

FLOWS IN POROUS MEDIA: VISUALIZATION BY
MAGNETIC RESONANCE IMAGING

by

Mark D. Shattuck

Department of Physics
Duke University

Date: _____

Approved:

Robert Behringer, Supervisor

Henry Greenside

G. Allan Johnson

Richard Walter

Dissertation submitted in partial fulfillment of the
requirements for the degree of Doctor of Philosophy
in the Department of Physics
in the Graduate School of
Duke University

1995

Copyright © 1995 by Mark D. Shattuck
All rights reserved

ABSTRACT

(Physics)

FLOWS IN POROUS MEDIA: VISUALIZATION BY
MAGNETIC RESONANCE IMAGING

by

Mark D. Shattuck

Department of Physics
Duke University

Date: _____

Approved:

Robert Behringer, Supervisor

Henry Greenside

G. Allan Johnson

Richard Walter

An abstract of a dissertation submitted in partial
fulfillment of the requirements for the degree
of Doctor of Philosophy in the Department of
Physics in the Graduate School of
Duke University

1995

Abstract

We have developed a Magnetic Resonance Imaging, MRI, technique which non-invasively measures local interstitial fluid velocity distributions in fully-saturated porous media. This was achieved by extending the standard three-dimensional MRI sequence to include local velocity and temperature information and adapted the technique to use the fast spin echo technique. We then applied this novel technique to two important problems. First, we studied pressure-driven flow through a fully-saturated, cylindrical packed bed. In this flow, we observed for the first time flow channeling inside a porous medium, as previously predicted. The MRI technique can also measure the local relative density. Which provides a non-invasive way of determining the spacial distribution of porosity in a porous medium. We used this information to verify previous findings concerning long-range spacial order and spacial oscillations in the porosity of packed beds of spheres. We found that the distribution of velocities in the flowing system is exponential. To our knowledge, this surprising fact has never before been documented. In the second application, we studied Porous Media Convection, PMC, from onset to eight times the critical Rayleigh number, Ra_c . We analyzed both ordered and disordered packings of mono-disperse spheres, in circular, rectangular, and hexagonal planforms. The disordered media was characterized by large ordered regions of close packing with grain boundaries and isolated defects. The defects created regions of larger

permeability, and thus spacial variations in the Rayleigh Number, Ra . We define the critical Ra , Ra_c , as Ra at the onset of convection in the ordered regions. We find that stable localized convective regions exist around grain-boundaries and defects at $Ra < Ra_c$ and remain as pinning sites for the convection patterns in the ordered regions as Ra is increased above Ra_c . In ordered media, defects only occurred within a thin region near the vertical walls. Stable localized convection began at $0.5Ra_c$ in the wall regions, and did not seem to affect the pattern in the interior regions. We observed roll-like structures that decayed rapidly to stable patterns between 1 and $5Ra_c$, which is consistent with theory. However, we found a wavenumber which is 0.7π compared to π derived from linear stability theory. We found an asymmetry between the size of up-flowing and down-flowing regions, with their ratio decreasing as Ra is increased, and a time-dependent state beginning at $6Ra_c$ and continuing through $8Ra_c$, the largest Ra that we studied. the slope of the Nusselt curve was determined to be 0.70 ± 0.05 which does not agree with the predicted value of 2.

To my wife, Dianna.

Acknowledgements

I sat down to make a list of all the people who have had significant influence on my progress towards my PhD. In a few minutes, I had over 25 people on that list. As I thought about the people on the list, it was clear that my success here has been a group effort.

I have had an opportunity that few students get to experience – the collaboration of three advisors. I have learned many things from each one, and my experience at Duke has been enhanced many more times than linear theory would predict. I gratefully thank Bob Behringer, Al Johnson, and John Georgiadis for the wisdom and knowledge that they have freely given to me. Bob has always been patient and supportive during the inevitable problems that arise in a large project like this, and excited and encouraging throughout the project. Al has provided many tools and resources which make this project a success. John's exuberance has kept this project exciting. We miss him at Duke.

I am grateful for the folks of the Center for In-vivo Microscopy, who have made the magnet room a productive and fun place. I would specifically like to thank Gary Cofer for keeping the magnets working and keeping me entertained; Sally Gewalt for the programs she has written and for many interesting discussions; Mark Martin for keeping the data flowing in spite of my complaining and for the fun we had scanning the Enterprise; Steve Suddarth for many en-

lightening conversations; Elaine Fitzsimons' helpful advice about manuscripts and abstracts; Bob Black for putting up with my heretical stance on famous people's equations; James MacFall for discussion on flow encoding; Janet MacFall for letting me get some magnet time;) and everyone else in the lunch crew; Hatty, Larry, Harrell.

I am also thankful for the LTB group members that have been here during my 7 year (and counting) stay: Karen Anderson who gave me a deep appreciation for the mysteries of science; Bill Baxter for being so excited about a sand box when I came to visit as a prospective student; Guy Metcalfe for many hours of conversation about science and life; Rick Leone for keeping me informed about the physics gossip; Jeff Olafsen for always being there for a good CB; Laurens Howle for the literature on porous media that he has pointed out; Brian Miller for many great discussions of religious issues; Orin Day for the weekly Monty Python readings; Eric Van Doorn for great conversations and for letting me make suggestions for his experiments. I have not had the opportunity to spend much time with the newest members of the group, Jason Fiering and Josh Fagans, but I have enjoyed beating both of them in ping-pong.

I would like to thank Henry Greenside for the semester projects which we worked on. The knowledge he imparted to me concerning Unix, stability analysis, and programming have been very valuable. Also, our discussions concerning this dissertation were quite useful.

I am very grateful to my parents, Sharon and David Shattuck, for always believing in me, and encouraging me to be myself. The value of good parents who love you is immeasurable. I would also like to thank my sisters, Elisabeth and Jennifer Shattuck for making our family a great place in which to grow

up.

I wish to acknowledge my wife, Dianna Shattuck. I *love* her with my whole being, and I thank her for putting up with me, especially during the preparation of this document. Without her encouragement and faith in me I am certain that this dissertation would not have been completed this semester.

This work is supported by the following grants:

DOE: DE-FG05-90-ER14141

NIH: 1P41 RR05959

NSF: CDR-8622201

Contents

Abstract	i
Dedication	iii
Acknowledgements	iv
List of Figures	x
List of Tables	xv
Introduction	2
I Magnetic Resonance Imaging	6
Introduction	7
1 Theory	8
1.1 Introduction	8
1.2 Nuclear Magnetic Resonance	9
1.2.1 Introduction	9
1.2.2 The Classical Nucleus	9
1.2.3 The Bloch Equations	12
1.2.4 Solutions to the Bloch Equations	16
1.2.5 Excitation	18
1.2.6 Free Induction Decay	23
1.2.7 Spin Echo	23
1.3 Magnetic Resonance Imaging	26
1.3.1 Introduction	26

1.3.2	Spacial Encoding	26
1.3.3	Sampling k-space	31
1.3.4	Selective Excitation	32
1.3.5	Pulse Sequence	37
	Introduction	37
	Gradient Recalled Echo	38
	Limited Flip Angle	44
	Echo Planer Imaging	44
	Spin Echo	47
	Fast Spin Echo	50
1.4	Velocity Measurement with MRI	55
1.4.1	Introduction	55
1.4.2	Flow in the Presence of a Linear Gradient	55
1.4.3	Time-of-Flight	58
1.4.4	Phase Contrast	59
1.4.5	Fourier Velocity Encoding	63
	Introduction	63
	Spin Echo Pulse Sequence	66
	Fast Spin Echo Pulse Sequence	70
2	Verification of Velocity Measurements with MRI	74
2.1	Introduction	74
2.2	Bulk Flow in a Pipe	75
2.3	Rotating Cylinder	82
2.4	Conclusions	86
II	Porous Media Flows	87
	Introduction	88
3	Pressure-Driven Flows	90
3.1	Introduction	90
3.2	Previous Experiments	92
3.3	Theory	94
	3.3.1 Introduction	94
	3.3.2 Representative Elementary Volume	94
	3.3.3 Conservation of Mass	95

3.3.4	Boundary Conditions	96
3.3.5	Darcy's Law	97
3.3.6	Flow Channelling	99
3.4	Experimental Setup	100
3.5	Results	103
3.5.1	Long Range Order	103
3.5.2	Spacial Averaging of Porosity	103
3.5.3	Flow Channeling	109
3.5.4	Velocity Distributions	113
3.6	Conclusions	113
3.7	Future Directions	114
4	Porous Media Convection	115
4.1	Introduction	115
4.2	Previous Experiments	116
4.3	Theory	117
4.3.1	Equations of motion	117
4.3.2	Additional terms	121
4.3.3	Amplitude equations	126
4.3.4	Symmetry	128
4.3.5	Comparison of PMC and RBC	129
4.3.6	Heat transport	131
4.3.7	Size of apparatus	132
4.4	Experimental Setup	133
4.4.1	The Convection Cell	133
4.4.2	Temperature Control	134
4.4.3	Planform and Packing	134
4.4.4	Heat Flux Measurement	137
4.5	Results	139
4.5.1	Disordered media	139
4.5.2	Ordered media	140
4.6	Conclusions	152
4.7	Future Directions	155
	Conclusion	157
	Bibliography	159

Biography

166

List of Figures

1.1	Pulse sequence for two-dimensional GRE.	39
1.2	K-space trajectory for two-dimensional GRE.	40
1.3	Pulse sequence for three-dimensional GRE.	42
1.4	K-space trajectory for three-dimensional GRE.	43
1.5	Pulse sequence for EPI.	45
1.6	K-space trajectory for EPI.	46
1.7	Pulse sequence for SE.	48
1.8	K-space trajectory for SE.	49
1.9	Pulse sequence for three-dimensional SE.	50
1.10	Pulse sequence for FSE.	51
1.11	K-space trajectory for FSE.	52
1.12	Pulse sequence for three-dimensional FSE.	54
1.13	Diagram showing the time-of-flight flow measurement technique. We excite spins in a thin slice, shown with stripes. They are allowed to flow to position shown with hash marks, where we measure their positions.	58
1.14	Typical gradient form used in phase sensitive velocity measure- ments. Each lobe is a half period sine function.	62
1.15	Velocity encoding SE pulse sequence.	67
1.16	Graph of the slice gradient and its zeroth and first moments. . .	68
1.17	Velocity encoding FSE pulse sequence.	71
2.1	Three-dimensional plot of the velocity along a 3.175 cm pipe. The velocity is averaged over a 2 mm thick slice. The in-plane resolution is 140 μm . The velocity resolution is 0.6 mm s^{-1} . . .	76

2.2	Two-dimensional graph of the azimuthally averaged velocity along a 3.175 cm pipe. The velocity is averaged over a 2 mm thick slice and over the azimuthal angle. The resolution is $140\ \mu\text{m}$. The velocity resolution is $0.6\ \text{mm s}^{-1}$. We show the theoretical velocity profile as a dotted line. The theoretical curve is based on the flow rate and the diameter of the tube. There are no fitted parameters.	77
2.3	Graph of the distribution of velocity as a function of velocity for parabolic flow along a 3.175 cm pipe. The velocity is averaged over the entire 2 mm thick slice, in all directions. The velocity resolution is $0.6\ \text{mm s}^{-1}$. We show the theoretical velocity distribution as a dotted line. The theoretical curve is based on the flow rate and the diameter of the tube. There are no fitted parameters.	78
2.4	Three-dimensional plot of the velocity along the twin 1.765 cm pipes. The velocity is averaged over a 1 mm thick slice. The in-plane resolution is $195\ \mu\text{m}$. The velocity resolution is $40\ \mu\text{m s}^{-1}$. This maximum velocity is $520\ \mu\text{m s}^{-1}$	79
2.5	Two-dimensional graph of a line going through the centers of both pipes. The velocity is averaged over a 1 mm thick slice. The spacial resolution is $195\ \mu\text{m}$. The velocity resolution is $40\ \mu\text{m s}^{-1}$. We show the theoretical velocity profile, with a maximum velocity of $520\ \mu\text{m s}^{-1}$, as a dotted line. The theoretical curve is based on the flow rate and the diameter of the tube. There are no fitted parameters.	80
2.6	Graph of the distribution of velocity as a function of velocity for parabolic flow through both pipes. The velocity is averaged over the entire 1 mm thick slice, in all directions. The velocity resolution is $40\ \mu\text{m s}^{-1}$. We show the theoretical velocity distribution as a dotted line. The theoretical curve is based on the flow rate and the diameters of the tubes. There are no fitted parameters.	81
2.7	Velocity bins for a rotating cylinder. The rotation rate is one revolution per second. The diameter of the cylinder is 3.175 cm. Each image show a different velocity bin. The ringing artifact is caused by improper k-space filtering. Images of spins in the rotating disk which have velocity a) $-8.8\ \text{cm s}^{-1}$, b) $0\ \text{cm s}^{-1}$, c) $8.8\ \text{cm s}^{-1}$, and d) $17.6\ \text{cm s}^{-1}$	83

2.8	Three-dimensional graph of the vertical, in-plane velocity in the rotating cylinder. The velocity is averaged over a 2 mm thick slice, and the velocity resolution is 2.94 cm s^{-1} . The rotation rate is one revolution per second, and the diameter of the cylinder is 3.175 cm.	84
2.9	Grayscale images of the vertical velocity in the rotating disk at rotation rate of a) $2\pi \text{ rad s}^{-1}$, b) $4\pi \text{ rad s}^{-1}$, and c) $8\pi \text{ rad s}^{-1}$. The intensity of grey is proportional to the velocity. As the rate increases, the images become somewhat distorted.	85
3.1	Schematic showing the test section used in the MRI pressure-driven flows experiments. The section consists of $3.204 \pm .029 \text{ mm}$ diameter mono-disperse spherical acrylic beads randomly packed in a 3.175 cm inner diameter tube. The beads are held in two perforated plugs.	100
3.2	Schematic showing constant pressure head system connected to the test section.	101
3.3	Volumetric rendering of the interstitial space (filled with water) in a packed bed using Magnetic Resonance Imaging. The section consists of $3.204 \pm .029 \text{ mm}$ diameter mono-disperse spherical acrylic beads randomly packed in a 3.175 cm inner diameter tube. The intensity of the grey scale corresponds to the density of water at that point. This is a small section from a $256 \times 256 \times 256$ isotropic array. The spacial resolution is 0.14 mm.	102
3.4	Image of porosity averaged over the \hat{z} axis, parallel to the tube. The image is averaged over 35 mm or 11 bead diameters from a $256 \times 256 \times 256$ isotropic array. The pixels are 0.14 mm across. The grey values are scaled to the maximum intensity pixel.	104
3.5	Plot of the azimuthally averaged porosity of a thin axial slice as a function of radius. A single slice, which is 0.14 mm thick was taken from a $256 \times 256 \times 256$ isotropic density acquisition of the test section in figure 3.1. This plot is the azimuthal average of that slice. The tube diameter is 3.175 mm.	105
3.6	Plot of the porosity averaged azimuthally and over the \hat{z} axis as a function of radius. A thick slice, which is 35 mm or 11 bead diameters thick was taken from a $256 \times 256 \times 256$ isotropic density acquisition of the test section in figure 3.1. The slice was averaged azimuthally and over \hat{z} . The tube diameter is 3.175 mm.	106

3.7	Plot of the porosity averaged over the \hat{x} and \hat{y} axes as a function of z from a $256 \times 256 \times 256$ isotropic density acquisition of the test section in figure 3.1. The tube diameter is 3.175 mm.	107
3.8	Graph of porosity as a function of averaging volume, V_{rev} , for 27 random starting positions within the central region.	108
3.9	Axial velocity contours in a cross-section of a packed bed during pressure driven flow. The velocity is averaged in the flow direction over a 2 mm slice. Each velocity contour represents 0.8 mm s^{-1}	110
3.10	Graph showing flow channelling in a 15.9 mm radius pipe packed with 3.2 mm beads. The azimuthally averaged, axial velocity profile in a 2 mm axial slice is shown with the solid line. The azimuthally averaged porosity is shown as a dashed line. The velocity is highest in the regions of largest porosity near the wall.	111
3.11	A graph showing the distribution of velocities integrated over a 2 mm slice perpendicular to the flow direction in a 3.175 mm pipe filled with 3.2 mm beads. For comparison the distribution of velocities for bulk pipe flow is shown in figure 2.3	112
4.1	Stability diagram determined by Strauss (1974). The hatched region is the conducting state. The stripped region is stable.	122
4.2	Schematic of convection cell. Hot water flows in from the bottom and cold flows in from the top. The outer circle represents the bore of the magnet, which is 15.24 cm.	135
4.3	(a) Density MRI of a 1 mm horizontal slice of the disordered media. The slice is taken at approximately mid-plane. (b) Density MRI of a 8 mm vertical slice of the disordered media.	136
4.4	Cross section of experimental cell, Delrin spacer, and Nu measurement sandwich. T_1 , T_2 , and T_3 are measured temperatures. k_D , k_s , and k_m are the conductivity of the Delrin spacer, the sandwich, and the medium, respectively.	138
4.5	Vertically averaged, vertical velocity for circular cell with disordered packing. a) $\Delta T = 0$. b) $\epsilon = -0.5$. c) $\epsilon = 1$. d) $\epsilon = 3$. e) $\epsilon = 5$. f) $\epsilon = 3$, but after dropping ΔT to 0.	141
4.6	Vertically averaged, vertical velocity for hexagonal cell with ordered packing. a) $\epsilon = -0.2$. b) $\epsilon = 1$. c) $\epsilon = 2$. d) $\epsilon = 3$	142
4.7	Vertically averaged, vertical velocity for hexagonal cell with ordered packing. a) $\epsilon = 4$. b) $\epsilon = 5$. c) $\epsilon = 6$. d) $\epsilon = 7$	143

4.8	Vertically averaged, vertical velocity for hexagonal cell with ordered packing at $\epsilon = 1$, but ΔT was dropped to 0 between each image.	144
4.9	Vertically averaged, vertical velocity for rectangular cell with ordered packing for various values of ϵ . a) $\epsilon=-0.5$ b) $\epsilon=0.2$ c) $\epsilon=0.4$	146
4.10	Vertically averaged, vertical velocity for hexagonal cell with ordered packing. All images, except for the last, are $2\tau_v$ apart. a) The time-dependent state before quenching ΔT . $\epsilon = 7$ b-e) Decay to steady state at $\epsilon = 2$. f) State $100\tau_v$ after quench.	148
4.11	Plot of the ratio of up-flowing roll width to down-flowing roll width versus ϵ for several runs.	149
4.12	Plot of ϵ versus reduced wavenumber, Q for several runs.	150
4.13	Vertically averaged, vertical velocity for hexagonal cell with ordered packing showing time-dependent behavior above 4ϵ . The images are separated by $2\tau_v$, and $\epsilon = 7$	151
4.14	Plot of Nu versus reduced Ra , ϵ , for two different runs.	153

List of Tables

4.1	Material parameters (Unless otherwise noted, medium properties are for the close-packed cell and are calculated based on an average of the separate properties weight by the porosity.)	133
4.2	Physical dimensions of various spacers.	136

Introduction

Porous media flows are ubiquitous in nature and in engineering. They are central to many environmental applications, chemical engineering processes, biological systems, and other industrial processes, such as oil and gas recovery, aquifers, filtration, catalytic beds, serum flow in living tissue, extraction of geothermal energy, and heat transport in insulation and packed beds (Combernous & Bories, 1975). Porous media can vary substantially, from a carbon filter, to sand on a beach, to capillary beds in living creatures. Most natural and technological porous media flows are very complicated. They may have multi-phase multi-component fluids, with moving and stationary matrices. In studying such complex systems, it is often very difficult to gain insight which can be carried from one problem to another. As a result, it is common to study simplified model systems with the hope that general principles will be uncovered which will apply to a large class of problems.

We have chosen Porous Media Convection, PMC, as the central experiment in this study. PMC is a model system for many of the applications listed above. It is also an example of a broad class of nonlinear pattern forming system that are characterized by the growth of a spacial or temporal pattern from a uniform state as a control parameter is changed. In PMC, the control parameter is the vertical temperature difference across a horizontal fluid saturated porous layer heated from below. When this difference is small, the fluid is at rest and the layer is in a motionless state with heat simply conducting through the media. But at a critical point, when the temperature difference is large enough, the fluid will begin to move. This motion is not random, however; it has a distinct pattern. In theory, the pattern is long straight rolls of a particular wavelength. Theoretical predictions like this one can apply to a broad class of pattern forming systems. This wide applicability to diverse systems is one reason why

studying nonlinear pattern forming systems is so exciting and fruitful. Insights gained from pattern formation in convective systems has applications to pattern formation on the wings of a butterfly, to patterns in sand at the beach, and to electrical patterns in hearts (Cross & Hohenberg, 1993).

One of the most thoroughly studied pattern forming systems is the bulk fluid analog to PMC, Rayleigh-Bénard convection, RBC. PMC offers some advantages over RBC in terms of their theoretical descriptions. Both systems have similar non-linear heat equations, but the momentum equation for PMC is a linear first-order partial differential equation, while the counterpart in RBC is non-linear second-order partial differential equation. This simplification has at least one important consequence, that the vertical vorticity in PMC decays to zero rapidly. It has been suggested that the vertical vorticity may play an important role in the complex dynamics observed for low to moderate Pr fluids in RBC (Siggia & Zippelius, 1981; Morris, Bodenschatz, Cannell & Ahlers, 1993).

Despite the technical importance of porous media and the theoretical advantages that it has over RBC, progress in understanding PMC and porous media flows in general have been hindered for some time by experimental difficulties (Torrance, Schoenhals, Tien & Viskanta, 1982; Georgiadis, 1991). For bulk fluids, many ingenious techniques have been developed to measure velocity and visualize flow in bulk fluids, for example, shadowgraph, laser Doppler velocimetry, interferometry, Schlieren or Topler techniques, particle streaks, dyes, smoke, and even fish scales. Common to these techniques is the need for optical transparency, which is difficult to achieve in porous media due to dispersion from the solid matrix. Transparency is even more difficult to attain if temperature gradients are present, as is the case in convective flows.

In such instances, index matching the fluid to the solid matrix is no longer possible. As a result, porous media flow visualization and velocity information have typically been either invasive (Bories & Thirriot, 1969; Prasad, Kulacki & Keyhani, 1985; Lister, 1990), based on theoretical correspondence to bulk flow (Elder, 1967), or based on inference from flow in adjacent bulk regions (Beckermann, Viskanta & Ramadhyani, 1988). Recently, however, some progress has been made in modifying some of these techniques for use in special geometries or conditions (Northrup, Kulp & Angel, 1991; Lein & Tankin, 1992; Howle, Behringer & Georgiadis, 1993). Even with these recent advances, quantitative velocity information and visualization had not been achieved in the general case.

In order to study porous systems, we have developed a general non-invasive technique which can measure fluid velocity in porous media. We have applied Magnetic Resonance Imaging, MRI, to this problem and produced the first non-invasive velocity profiles of convective flows in packed beds of beads. MRI provides non-invasive quantitative velocity, density, and temperature information in porous media saturated with water or any fluid that contains atoms with a nuclear magnetic moment. MRI is particularly suited for porous media studies since it is not sensitive to the solid matrix. The exception to this is a solid matrix that has high electrical conductivity or large magnetic susceptibility.

Although the MRI velocity distribution measurement technique that we use had been theoretically developed previously by Moran (1982) and verified experimentally by Redpath, Norris, Jones & Hutchison (1984), it had not been implemented at the Duke University Center for In-vivo Microscopy, where this research was conducted. A major part of this work was adapting and improving this method for use at our facility. We adapted this technique to measure

the small velocities encountered in convection experiments and increased the speed of acquisition by combining the velocity measurement technique with the fast spin echo technique. Consequently, this dissertation is broken into two parts. Part I is devoted entirely to MRI and part II contains the results of our experiment using MRI to measure flow in porous media. Both parts of this dissertation are, for the most part, self contained. Readers interested in only one part should feel free to skip the other part.

While the development in part I is not comprehensive, it goes beyond the essential information necessary to explain the technique used in this work. This approach was taken because the study of MRI represents a large portion of time and effort spent on this research and is a fascinating application of many aspects of basic physics. The information gathered here from multiple sources should also be useful to future students.

In part II, we apply the MRI technique to pressure driven flow through a pipe in chapter 3. Although, this is one of the simplest and most studied problems in porous media, with our new technique we were able to make a least one new discovery. We found that the distribution of velocities is exponential.

In chapter 4 we describe our PMC experiments. Because experimental velocity information is lacking, this allows the unique opportunity to provide the first experimental data to test the many theoretical ideas. Most of these ideas are based on a continuum approach that treats the porous medium as a homogeneous sample described by one or more parameters. We discuss some of these parameters, porosity, permeability, and coarseness, in detail, as well as the connection of porous media to continuum models. In some instances, our data confirms these theoretical ideas, but other results await explanation. In

these experiments, we provide detailed velocity information, never before available from porous media flows, which is useful for both theory and application.

Part I

Magnetic Resonance Imaging

Introduction

Chapter 1

Theory

1.1 Introduction

When a nucleus with a magnetic moment, or spin, is placed in a magnetic field, the magnetic moment precesses about the magnetic field direction with a frequency proportional to the field strength. If an oscillating magnetic field is also applied, there is a net absorption of energy from the oscillating field when its frequency is equal to the frequency of precession. NMR is the process of resonant absorption of energy by the nuclear spin and can be used to determine many details of atomic interactions and molecular structure.

NMR is also the basis of MRI. Because the nuclear magnetic moment precession frequency is proportional to the magnetic field strength, a field which varies linearly with position can be used to encode spacial information into the frequency of precession. The precession of nuclear magnetic moments will induce a time-varying signal in a loop of wire. The signal can be decomposed into frequency components, using a Fourier transform to give the spacial information contained in the frequencies. The use of linear field gradients to encode information is the basis of almost all NMR imaging schemes.

Velocity information can be encoded in a similar way using a bipolar gra-

dient, which consists of two gradient pulses of equal area, one of which has the gradient direction reversed. In this situation, a stationary spin precesses faster (slower) during the first pulse and slower (faster) during the second pulse. The net result is that all stationary spins have the same phase relation before and after the application of a bipolar gradient. Spins which move in the gradient direction between the application of the first and second pulses will not return to their initial phase. Under the approximation that the pulse width is very small, the phase change of a moving spin is proportional to the distance traveled in the direction of the field gradient and therefore proportional to the average velocity, if the time between pulses is fixed. With the use of phase sensitive detection, information about the velocity of the spin can be obtained from the phase of the precession while the position is determined using the frequency information.

1.2 Nuclear Magnetic Resonance

1.2.1 Introduction

While quantum mechanical ideas and constructs are required for a full understanding of NMR and MRI, most concepts can be understood from a classical viewpoint. The classical approach also provides physical intuition about many important concepts. In the following discussion we use the classical approach, whenever possible.

1.2.2 The Classical Nucleus

Classically, we imagine the nucleus as a spatially localized spinning charge and mass distribution, $\rho_e(\mathbf{r})$ and $\rho_m(\mathbf{r})$ respectively. Only nuclei with net spin can

be used in an NMR experiment. We calculate the torque, \mathbf{N} , on a spinning nucleus in an external magnetic field, $\mathbf{H}(\mathbf{r})$, from the current density, $\mathbf{J}(\mathbf{r})$, which is produced by the circulating charge distribution (Jackson, 1975);

$$\mathbf{N} = \int \mathbf{r} \times (\mathbf{J}(\mathbf{r}) \times \mathbf{H}(\mathbf{r})) dV, \quad (1.1)$$

where we have used MKS units. This result is derived from the elemental force law $d\mathbf{F} = d\mathbf{I} \times \mathbf{H}$. If we expand the field to lowest order about the center of the nucleus, integrate by parts, and assume that $\nabla \cdot \mathbf{J} = 0$, we obtain:

$$\mathbf{N} = \mathbf{m} \times \mathbf{H}(\mathbf{r}_0), \quad (1.2)$$

where \mathbf{r}_0 is the position of the nucleus, and \mathbf{m} is the magnetic moment, given by

$$\mathbf{m} = \frac{1}{2} \int \mathbf{r} \times \mathbf{J}(\mathbf{r}) dV. \quad (1.3)$$

Equation (1.2) is the familiar equation for the torque on a magnetic dipole. The integrand in (1.3) is the magnetic moment density, \mathbf{M} , or magnetization. Since the torque is given by

$$\mathbf{N} = \frac{d\mathbf{L}}{dt}, \quad (1.4)$$

where \mathbf{L} is the angular momentum, we seek a relation between \mathbf{L} and \mathbf{m} . From (1.3) the contribution to the magnetic moment from a small volume, dV , moving at velocity, \mathbf{v} , is

$$d\mathbf{m} = \frac{1}{2} \mathbf{r} \times (\rho_e(\mathbf{r})\mathbf{v}) dV, \quad (1.5)$$

where $\mathbf{J}(\mathbf{r})$ has been replaced by the density times the velocity of the small volume, $(\rho_e(\mathbf{r})\mathbf{v})$. The contribution to the angular momentum from a small

volume, dV , of mass, dm , moving at velocity, \mathbf{v} , is

$$d\mathbf{L} = \mathbf{r} \times dm\mathbf{v} = \mathbf{r} \times (\rho_e(\mathbf{r}) dV)\mathbf{v}. \quad (1.6)$$

Combining (1.5) and (1.6) and integrating we obtain a relation between \mathbf{m} and \mathbf{L} :

$$\mathbf{m} = \frac{1}{2} \int \frac{\rho_e(\mathbf{r})}{\rho_m(\mathbf{r})} d\mathbf{L}. \quad (1.7)$$

If we assume (Goldstein, 1980) that

$$\frac{\rho_e(\mathbf{r})}{\rho_m(\mathbf{r})}$$

is constant, then

$$\mathbf{m} = \frac{e}{2m_N} \mathbf{L} = \gamma \mathbf{L}, \quad (1.8)$$

where

$$e = \int \rho_e(\mathbf{r}) dV, \quad (1.9)$$

is the total charge of the nucleus and

$$m_N = \int \rho_m(\mathbf{r}) dV, \quad (1.10)$$

is the total mass of the nucleus. Equation (1.8) states that the magnetic moment and the angular momentum of the nucleus are parallel and that their magnitudes differ by

$$\gamma = \frac{e}{2m_n}, \quad (1.11)$$

which is called the gyromagnetic ratio. The fact that \mathbf{m} and \mathbf{L} are parallel is based on the assumption that the charge-to-mass ratio is uniform throughout the nucleus. While it is experimentally found that \mathbf{m} and \mathbf{L} are parallel, this

classical argument still breaks down with respect to the value of γ . The value of γ for the proton from (1.11) is $4.789 \times 10^7 \text{ Hz T}^{-1}$ and the experimental value is $4.258 \times 10^7 \text{ Hz T}^{-1}$. However, this discrepancy in γ can be rectified using relativistic quantum mechanics. Finally, by combining (1.8), (1.2), and (1.4), we obtain an evolution equation for the magnetic moment of a nucleus in an external magnetic field:

$$\frac{d\mathbf{m}}{dt} = \gamma \mathbf{m} \times \mathbf{H}. \quad (1.12)$$

Note that (1.12) is equally valid for the magnetization assuming as above that \mathbf{H} does not change over the size of the nucleus. In (1.12) we have derived the evolution of the nuclear magnetic moment of a single nucleus. For a collection of nuclei the total magnetic moment, \mathbf{m} , is the sum of the individual magnetic moments \mathbf{m}_i :

$$\mathbf{m} = \sum_{i=1}^N \mathbf{m}_i,$$

or in the limit of a large number of spins

$$\mathbf{m} = \int \mathbf{M} dV, \quad (1.13)$$

where \mathbf{M} is the magnetic moment per unit volume, or magnetization.

1.2.3 The Bloch Equations

Equation (1.12) is the starting point for the derivation of the phenomenological Bloch equations (Bloch, 1946). Bloch derived these equations from observation of one the first NMR experiments performed by Bloch, Hansen & Packard (1946) in the same year that a second group (Purcell, Torrey & Pound, 1946) independently discovered NMR.

The two groups had different approaches. Bloch et al. (1946) observed the resonance phenomenon by induction while Purcell et al. (1946) used absorption. The Bloch equations explain both of these techniques.

For diamagnetic materials, Bloch pointed out that two major effects have been neglected in (1.12), thermal noise and the fields produced by neighboring nuclei. Of these two contributions, only thermal noise can change the energy of the system. For a linear material,

$$\mathbf{B} = \mu \mathbf{H},$$

where μ is the magnetic permeability of the material, and \mathbf{B} is the magnetic induction. Combining this definition with

$$\mathbf{H} = \frac{1}{\mu_0} \mathbf{B} - \mathbf{M}$$

gives

$$\mathbf{M} = \chi_m \mathbf{H}, \tag{1.14}$$

where μ_0 is the permeability of free space, and

$$\chi_m = \frac{\mu}{\mu_0} - 1,$$

is the magnetic susceptibility. For such linear materials the total energy in a magnetic system is (Jackson, 1975)

$$U = \frac{1}{2} \int \mathbf{H} \cdot \mathbf{B} dV.$$

When an object of permeability μ is placed into a magnetic field in free space, \mathbf{H}_0 , with magnetic induction \mathbf{B}_0 then the change in energy is

$$\Delta U = \frac{1}{2} \int (\mathbf{B} \cdot \mathbf{H} - \mathbf{B}_0 \cdot \mathbf{H}_0) dV$$

$$= \frac{1}{2} \int [\mathbf{B} \cdot \mathbf{H}_0 - \mathbf{B}_0 \cdot \mathbf{H} + (\mathbf{B} + \mathbf{B}_0) \cdot (\mathbf{H} - \mathbf{H}_0)] dV. \quad (1.15)$$

Since $\nabla \cdot (\mathbf{B} + \mathbf{B}_0) = 0$, $(\mathbf{B} + \mathbf{B}_0)$ can be described by the curl of another vector, \mathbf{A} . Therefore,

$$(\mathbf{B} + \mathbf{B}_0) = \nabla \times \mathbf{A},$$

and the final term in the integrand of (1.15) may be written:

$$\frac{1}{2} \int (\nabla \times \mathbf{A}) \cdot (\mathbf{H} - \mathbf{H}_0) dV.$$

Integration by parts gives

$$-\frac{1}{2} \int \mathbf{A} \cdot \nabla \times (\mathbf{H} - \mathbf{H}_0) dV.$$

If we assume that the current density, \mathbf{J} , is fixed, then

$$\nabla \times (\mathbf{H} - \mathbf{H}_0) = 0,$$

and from (1.15)

$$\begin{aligned} \Delta U &= \frac{1}{2} \int (\mathbf{B} \cdot \mathbf{H}_0 - \mathbf{B}_0 \cdot \mathbf{H}) dV \\ &= \frac{1}{2} \int \left(\frac{\mu}{\mu_0} - 1 \right) \mathbf{H} \cdot \mathbf{B}_0 dV \\ &= \frac{1}{2} \int \mathbf{M} \cdot \mathbf{B}_0 dV. \end{aligned} \quad (1.16)$$

Therefore, changes in energy must be due to changes in the component of magnetization in the direction of the magnetic field. In thermal equilibrium, we expect that (1.14) will give the magnetization and that \mathbf{M} will point in the same direction as the applied field. When

$$\mathbf{M} \neq \chi_m \mathbf{H},$$

Bloch determined that \mathbf{M} relaxes to $\chi_m \mathbf{H}$ exponentially with a time constant T_1 . For $\mathbf{H} = H_0 \hat{z}$,

$$\frac{dM_z}{dt} = \frac{M_0 - M_z}{T_1}, \quad (1.17)$$

where $M_0 = \chi_m H_0$. Thermal noise contributes to changing all three components of \mathbf{M} . In equilibrium, the components transverse to the magnetic field, M_x and M_y , are zero. Bloch also determined that if the transverse components ever become non-zero then they will decay exponentially to zero. There are two effects which cause this decay. First, as with the longitudinal component, thermal noise causes decay. Second, interactions with internal fields created by other nuclei also cause decay. The internal interactions only affect the transverse components since they cannot change the total energy of the system. Thus, the decay time constant in this case is not T_1 , but is called T_2 and contains all factors which can cause irreversible transverse relaxation, including T_1 and interaction with other nuclei. Because of this definition, $T_1 \geq T_2$. Typically for solids $T_1 \gg T_2$ since the local magnetic field due to other nuclei is very strong. In liquids like water, T_1 and T_2 are of the same order. For a magnetic field in the \hat{z} direction,

$$\frac{dM_{x,y}}{dt} = \frac{-M_{x,y}}{T_2}. \quad (1.18)$$

Combining (1.12), (1.17), and (1.18) we obtain the phenomenological Bloch equation:

$$\frac{d\mathbf{M}}{dt} = \gamma \mathbf{M} \times \mathbf{H} + \frac{M_0 - M_z}{T_1} \hat{z} - \frac{M_x \hat{x} + M_y \hat{y}}{T_2}. \quad (1.19)$$

Equation (1.19) is only strictly true when $\mathbf{H} = H_0 \hat{z}$, but can be used as long as the \hat{z} component of \mathbf{H} is much larger than any other component.

1.2.4 Solutions to the Bloch Equations

We define a complex magnetization,

$$\mathbf{M} = (M, M_z), \quad (1.20)$$

where the transverse magnetization, M , is given by

$$M = \mathcal{M} \exp(i \Phi_M) = M_x + i M_y, \quad (1.21)$$

and $i = \sqrt{-1}$. We also define a complex angular frequency, $\boldsymbol{\omega}$, by combining γ and \mathbf{H} :

$$\boldsymbol{\omega} = 2\pi\gamma\mathbf{H} = (\Omega, \omega_z), \quad (1.22)$$

where

$$\Omega = \Omega \exp(i \Phi_\Omega) = \omega_x + i \omega_y. \quad (1.23)$$

With these definitions we transform (1.19) into:

$$\frac{dM}{dt} = -i (M\omega_z - M_z\Omega) - \frac{M}{T_2} \quad (1.24)$$

$$\begin{aligned} \frac{dM_z}{dt} &= \frac{1}{2i} (M^*\Omega - M\Omega^*) + \frac{M_0 - M_z}{T_1} \\ &= \text{Im}(M^*\Omega) + \frac{M_0 - M_z}{T_1}, \end{aligned} \quad (1.25)$$

where $*$ denotes a complex conjugate. Equations (1.24-1.25) are a set of three coupled first-order linear differential equations, as is Equation (1.19), and a general solution may be obtained through standard techniques. However, because \mathbf{H} for NMR and MRI is special, it is more informative to look at solutions to simplified versions of (1.24-1.25).

We first consider a constant magnetic field in the \hat{z} direction with no relaxation, that is, $T_1 = T_2 = \infty$. For this case we obtain from (1.22-1.23)

$$\Omega = 0, \quad (1.26)$$

$$\omega_z = 2\pi\gamma H_0 \equiv \omega_L, \quad (1.27)$$

where ω_L is called the Larmor frequency. For protons at 2 T,

$$\omega_L = 2\pi(85.5 \text{ MHz}) = 537 \times 10^6 \text{ rad s}^{-1}.$$

Substituting (1.26-1.27) into (1.24-1.25) gives:

$$\frac{d\mathbf{M}}{dt} = -i\omega_L \mathbf{M} \quad (1.28)$$

$$\frac{dM_z}{dt} = 0. \quad (1.29)$$

The solution to (1.28-1.29) for an arbitrary initial condition, $\mathbf{M}_0 = (M_0, M_{z0})$ is

$$\mathbf{M} = \mathbf{M}_0 \exp(-i\omega_L t) \quad (1.30)$$

$$M_z = M_{z0}. \quad (1.31)$$

This solution is a precession of \mathbf{M}_0 about \mathbf{H} at the Larmor frequency, ω_L . It is this precession which Bloch et al. measured using induction. If we include relaxation, then (1.28-1.29) become

$$\frac{d\mathbf{M}}{dt} = \left(-i\omega_L - \frac{1}{T_2}\right)\mathbf{M} \quad (1.32)$$

$$\frac{dM_z}{dt} = \frac{M_0 - M_z}{T_1}. \quad (1.33)$$

The solution to (1.32-1.33) for an arbitrary initial condition, as above, is

$$\mathbf{M} = M_0 \exp(-i\omega_L t) \exp\left(-\frac{t}{T_2}\right) \quad (1.34)$$

$$M_z = M_{z0} \exp\left(-\frac{t}{T_1}\right) + M_0 \left(1 - \exp\left(-\frac{t}{T_1}\right)\right). \quad (1.35)$$

In (1.34-1.35) the precession of \mathbf{M}_0 about \mathbf{H} at ω_L decays to the equilibrium value of $M_0 \hat{z}$. In subsequent sections we will look at other solutions to the Bloch equation that are important in NMR and MRI.

1.2.5 Excitation

Transverse magnetization, \mathbf{M} , can be easily measured by induction with a simple loop of wire used as a resonant antenna. However, as shown in (1.34-1.35), \mathbf{M} decays to zero with a time constant T_2 , which can be quite short for solids, in the range of a few milliseconds or less. This presents the problem of how to produce transverse magnetization from a system which is in equilibrium. This is accomplished with a resonant excitation pulse. As we will see from the Bloch equations, an oscillating magnetic field can change the direction of \mathbf{M} and produce transverse magnetization. The production of \mathbf{M} is often referred to as excitation. All NMR and MRI applications use these oscillating fields, which are often produced by the same resonant antenna used to measure the signal. The equation describing such a field is

$$\mathbf{H}_1 = H_1 [\cos(\omega_1 t) \hat{x} - \sin(\omega_1 t) \hat{y}]. \quad (1.36)$$

In complex notation from (1.22-1.23), the angular frequency associated with \mathbf{H}_1 , $\boldsymbol{\omega}_1$, becomes

$$\boldsymbol{\omega}_1 = 2\pi\gamma\mathbf{H}_1 = (\Omega_1 \exp(-i\omega_1 t), 0), \quad (1.37)$$

Including the static component $H_0\hat{z}$ of the magnetic field the total angular frequency associated with field is

$$\boldsymbol{\omega} = 2\pi\gamma(\mathbf{H}_0 + \mathbf{H}_1) = (\Omega_1 \exp(-i\omega_1 t), \omega_L). \quad (1.38)$$

With the approximation of no relaxation, substituting (1.38) into (1.24-1.25) gives:

$$\frac{d\mathbf{M}}{dt} = -i(\mathbf{M}\omega_L - M_z\Omega_1 \exp(-i\omega_1 t)) \quad (1.39)$$

$$\frac{dM_z}{dt} = \text{Im}(\mathbf{M}^*\Omega_1 \exp(-i\omega_1 t)) \quad (1.40)$$

We now make the transformation:

$$\mathbf{M} = \mathbf{M}' \exp(-i\omega_1 t). \quad (1.41)$$

This transformation is equivalent to moving into a coordinate frame which is rotating with the applied field, \mathbf{H}_1 . Making substitutions from (1.41) into (1.39-1.40) and eliminating the common term

$$\exp(-i\omega_1 t)$$

from both sides, we obtain

$$\frac{d\mathbf{M}'}{dt} = -i[\mathbf{M}'(\omega_L - \omega_1) - M'_z\Omega_1] \quad (1.42)$$

$$\frac{dM'_z}{dt} = \text{Im}(\mathbf{M}'^*)\Omega_1. \quad (1.43)$$

The solution to (1.42-1.43) for the equilibrium initial condition $\mathbf{M}'_0 = (0, M_0)$ is

$$\mathbf{M}' = iM_0 \frac{\Omega_1}{W} \sin(Wt) + 2M_0 \frac{\Omega_1 \Delta\omega_1}{W^2} \sin^2\left(\frac{Wt}{2}\right) \quad (1.44)$$

$$M'_z = \frac{M_0(\Delta\omega_1^2 + \Omega_1^2 \cos(\Omega_1 t))}{W^2}, \quad (1.45)$$

where $W = \sqrt{\Delta\omega_1^2 + \Omega_1^2}$ and $\Delta\omega_1 = \omega_L - \omega_1$. When the excitation pulse is not on resonance, $\omega_1 \neq \omega_L$, then $W > \Omega_1$. As W increases with respect to Ω_1 the solution tends toward the initial condition. In the limit, $\Delta\omega_1 \rightarrow \infty$, then

$$\mathbf{M}' = 0 \quad (1.46)$$

$$M_z = M_0, \quad (1.47)$$

and the pulse has no effect on the equilibrium magnetization. Under the resonance condition $\omega_1 = \omega_L$, the first term in (1.42) vanishes, and (1.42-1.43) can be reduced to the following second-order equation for M_z :

$$\frac{d^2 M_z}{dt^2} = -\Omega_1^2 M_z. \quad (1.48)$$

We determine the solution for the equilibrium initial condition $\mathbf{M}'_0 = (0, M_0)$ from (1.48) and (1.42-1.43) or by setting $\Delta\omega_1 = 0$ in (1.44-1.45):

$$\mathbf{M}' = i M_0 \sin(\Omega_1 t) \quad (1.49)$$

$$M_z = M_0 \cos(\Omega_1 t). \quad (1.50)$$

In cartesian coordinates, in a frame rotating at ω_L (1.49-1.50) becomes

$$M'_x = 0 \quad (1.51)$$

$$M'_y = M_0 \sin(\Omega_1 t) \quad (1.52)$$

$$M_z = M_0 \cos(\Omega_1 t). \quad (1.53)$$

Equations (1.51-1.53) describe the magnetization vector precessing about \hat{x} in the rotating frame. In the laboratory frame, (1.49-1.50) become

$$\mathbf{M} = i M_0 \sin(\Omega_1 t) \exp(-i \omega_L t) \quad (1.54)$$

$$M_z = M_0 \cos(\Omega_1 t), \quad (1.55)$$

and (1.51-1.53) become

$$M_x = M_0 \sin(\Omega_1 t) \sin(\omega_L t) \quad (1.56)$$

$$M_y = M_0 \sin(\Omega_1 t) \cos(\omega_L t) \quad (1.57)$$

$$M_z = M_0 \cos(\Omega_1 t). \quad (1.58)$$

In (1.36) we choose \mathbf{H}_1 with a phase such that at $t = 0$ it points along \hat{x} . If we include an arbitrary phase, Φ_0 , then

$$\begin{aligned} \boldsymbol{\omega}_1 = 2\pi\gamma\mathbf{H}_1 &= 2\pi\gamma H_1 [\cos(\omega_1 t + \Phi_0)\hat{x} - \sin(\omega_1 t + \Phi_0)\hat{y}] \\ &= (\Omega_1 \exp(i\Phi_0) \exp(-i\omega_1 t), 0), \end{aligned} \quad (1.59)$$

and the solution in the rotating frame, in complex notation is

$$\begin{aligned} \mathbf{M}' &= i \exp(i\Phi_0) M_0 \sin(\Omega_1 t) \\ &= \exp\left(i\left(\Phi_0 + \frac{\pi}{2}\right)\right) M_0 \sin(\Omega_1 t) \end{aligned} \quad (1.60)$$

$$M_z = M_0 \cos(\Omega_1 t). \quad (1.61)$$

This shows that the magnetization precesses about \mathbf{H}_1 regardless of the phase. Further, comparison of (1.24-1.25), neglecting relaxation, and (1.42-1.43) show that they have the same form with the following identifications:

$$\begin{aligned} \mathbf{M} &\leftrightarrow \mathbf{M}' \\ \Omega &\leftrightarrow \Omega_1 \\ \omega_z &\leftrightarrow (\omega_L - \omega_1) = \Delta\omega_1. \end{aligned}$$

Therefore in vector notation (1.42-1.43) become

$$\frac{d\mathbf{M}'}{dt} = \mathbf{M}' \times \boldsymbol{\omega}_{\text{eff}}, \quad (1.62)$$

where

$$\boldsymbol{\omega}_{\text{eff}} = \Delta\omega_1 \hat{z} + \Omega_1 \hat{x}.$$

Because we are in the rotating frame, Ω_1 is constant, as is $\boldsymbol{\omega}_{\text{eff}}$. We have already solved (1.62) with a constant \mathbf{H} or $\boldsymbol{\omega}$. The solution as given in (1.30-1.31) is that \mathbf{M}' precesses about the direction of $\boldsymbol{\omega}_{\text{eff}}$ at a rate equal to the magnitude of $\boldsymbol{\omega}_{\text{eff}}$. At resonance, $\omega_1 = \omega_L$, (1.51-1.53) are recovered since

$$\boldsymbol{\omega}_{\text{eff}} = \Omega_1 \hat{x}.$$

As the excitation pulse is moved off resonance $\boldsymbol{\omega}_{\text{eff}}$ turns toward the \hat{z} axis. The polar angle that $\boldsymbol{\omega}_{\text{eff}}$ makes with the \hat{z} axis,

$$\theta = \tan^{-1}\left(\frac{\Omega_1}{\Delta\omega_1}\right),$$

determines the maximum transverse magnetization that can be produced. If $\theta \geq \frac{\pi}{4}$, then at some point during the precession the maximum transverse magnetization of M_0 will be created. Therefore, transverse magnetization can only be created when the excitation pulse is near resonance. When the excitation pulse is exactly on resonance, \mathbf{M} is rotated from the equilibrium value of $M_0 \hat{z}$ about \hat{x} by an angle $\Omega_1 t$. If \mathbf{H}_1 with $\Phi_0 = 0$ is turned on for a short time,

$$\frac{\pi}{2\Omega_1},$$

then $M_0 \hat{z}$ will be rotated about \hat{x} by an angle $\frac{\pi}{2}$ until it is in the \hat{y} direction, and the maximum transverse magnetization will be created. A short pulse of oscillating magnetic field which rotates the magnetization by an angle $\frac{\pi}{2}$ is called a $\frac{\pi}{2}$ -pulse. In general, by varying the duration, t_w , or magnitude of the pulse, Ω_1 , \mathbf{M} can be rotated to any angle, $\alpha = \Omega_1 t_w$, by an α -pulse. The

α -pulse described by (1.59) can rotate $M_0\hat{z}$ about any direction in the \hat{x} - \hat{y} plane depending on the value of Φ_0 . If $\Phi_0 = 0$, then the α -pulse is in the \hat{x} direction; if $\Phi_0 = \pi/2$, then the α -pulse is in the \hat{y} direction. In general, if the phase is Φ_0 then the α -pulse is applied with a phase of Φ_0 radians. Relaxation is typically ignored in excitation pulses since $t_w < T_2 \leq T_1$. However, in solids it can be significant. In this work we deal only with fluids and relaxation can safely be ignored during the excitation.

1.2.6 Free Induction Decay

In the original experiment performed by Bloch et al. (1946), a $\frac{\pi}{2}$ -pulse was used to produce transverse magnetization. Then the system was allowed to evolve with the oscillating field off. During this time M_y was monitored by induction using a pickup coil. The signal observed was an exponentially decaying oscillation of the form

$$-M_0 \cos(\omega_L t) \exp\left(-\frac{t}{T_2}\right),$$

as predicted from the Bloch equations in (1.34) for an initial $\mathbf{M}_0 = M_0\hat{y}$. This type of signal is called a free induction decay or f.i.d., and will occur in the absence of oscillating fields whenever transverse magnetization is created.

1.2.7 Spin Echo

In 1950 Hahn discovered an interesting phenomenon. He found that if he applied a pair of $\frac{\pi}{2}$ -pulses separated by time, τ , that a signal or echo would appear at a time, 2τ . He named this phenomenon a spin echo (Hahn, 1950), and it is an important part of many NMR experiments, including imaging

experiments. This result is more easily understood by examining a system in which a $\frac{\pi}{2}$ -pulse in the \hat{x} direction is followed by a π -pulse in the \hat{y} direction a time, τ , later. In a perfectly homogeneous magnetic field the $\frac{\pi}{2}$ -pulse would produce a f.i.d. which would decay with a time constant T_2 according to (1.34). If Hahn had used such a field, the spin echo would not have been discovered. Fortunately, laboratory fields are inhomogeneous. An inhomogeneous field, $\mathbf{H}_i(\mathbf{r})$ can be broken into two parts:

$$\mathbf{H}_i(\mathbf{r}) = (H_0 + \Delta H(\mathbf{r}))\hat{z} \quad (1.63)$$

where H_0 is the ideal homogeneous part, and $\Delta H(\mathbf{r})$ is the difference between H_0 and $\mathbf{H}_i(\mathbf{r})$. $\mathbf{H}_i(\mathbf{r})$ includes all static inhomogeneities, including any static variation due to susceptibility of the sample. We ignore any time-dependent variations in this analysis. Since $\mathbf{H}_i(\mathbf{r})$ does not depend on time the solution in (1.34) gives the transverse magnetization, \mathbf{M} , for an arbitrary initial condition, if the following substitution is made:

$$\omega_L \rightarrow \omega_L + \Delta\omega(\mathbf{r}),$$

where

$$\Delta\omega(\mathbf{r}) = 2\pi\gamma\Delta H(\mathbf{r}).$$

Assuming that the $\frac{\pi}{2}$ -pulse is short compared to T_2 , so that relaxation can be ignored during the pulse, and that the pulse is applied along the \hat{x} direction, then after combining with the initial condition derived from (1.60),

$$\mathbf{M}(\mathbf{r}, t) = i M_0 \exp(-i(\omega_L + \Delta\omega(\mathbf{r}))t) \exp\left(-\frac{t}{T_2}\right) \quad (1.64)$$

during the interval between the two pulses. Equation (1.64) gives the magnetization at a point, \mathbf{r} . To get the total magnetization over the whole volume,

$\mathbf{M}(\mathbf{r}, t)$ must be integrated over the volume of the sample. After integrating,

$$\mathbf{M}(t)_T = i M_{T_0} \exp(-i \omega_L t) \exp\left(-\frac{t}{T_2}\right) \left\{ \frac{1}{V} \int \exp(-i \Delta\omega(\mathbf{r})t) dV \right\}, \quad (1.65)$$

where V is the volume of the sample and

$$M_{T_0} = V M_0.$$

The portion of (1.65) in braces represents the effect of the inhomogeneity of the field. This term causes a decay of the signal over time with a time constant which is of the order of

$$\frac{1}{\overline{\Delta\omega(\mathbf{r})}},$$

where

$$\overline{\Delta\omega(\mathbf{r})} = \frac{1}{V} \int \Delta\omega(\mathbf{r}) dV.$$

For typical magnetic fields produced in the laboratory, the field inhomogeneities are one part per million. For protons at 2 T, this corresponds to $\overline{\Delta\omega(\mathbf{r})} \sim 537 \text{ rad s}^{-1} = 85.5 \text{ Hz}$ which is a much shorter decay than the T_2 decay of water. Inhomogeneity due to susceptibility depends on the sample and is often the largest contribution to $\overline{\Delta\omega(\mathbf{r})}$. Due to these inhomogeneities, the signal from the $\frac{\pi}{2}$ -pulse will typically decay much more quickly than expected by considering T_2 alone. However, it turns out that the decay due to static field variations is reversible by the application of a π -pulse. The total decay constant including T_2 and the reversible decay effects is often called T_2^* . If we again assume that the duration of the pulse is short compared to the relaxation parameters, then a π -pulse in the \hat{y} direction will rotate $\mathbf{M}(t)_T$ by π radians about the \hat{y} axis. This rotation is equivalent to reversing the sign of the \hat{x} component of $\mathbf{M}(t)_T$, or in complex notation by replacing $\mathbf{M}(t)_T$ by the negative

of its complex conjugate. Therefore the transverse magnetization just after the application of the π -pulse at time, τ is

$$\mathbf{M}(\tau)_T = i M_{T0} \exp(i \omega_L \tau) \exp\left(-\frac{\tau}{T_2}\right) \left\{ \frac{1}{V} \int \exp(i \Delta\omega(\mathbf{r})\tau) dV \right\}. \quad (1.66)$$

Equation (1.66) can now be used as a new initial condition for (1.34) to give

$$\begin{aligned} \mathbf{M}(\tau + t)_T = & i M_{T0} \exp(i \omega_L(\tau - t)) \exp\left(-\frac{\tau + t}{T_2}\right) \times \\ & \left\{ \frac{1}{V} \int \exp(i \Delta\omega(\mathbf{r})(\tau - t)) dV \right\}, \end{aligned} \quad (1.67)$$

where t now measures time from the π -pulse. At $t = \tau$ (1.67) reduces to

$$\mathbf{M}(2\tau)_T = i M_{T0} \exp\left(-\frac{2\tau}{T_2}\right). \quad (1.68)$$

The signal is back to what it would have been if $\Delta\omega(\mathbf{r}) = 0$. The signal loss from the inhomogeneities has been reversed and a spin echo is formed.

1.3 Magnetic Resonance Imaging

1.3.1 Introduction

MRI is a non-invasive technique based on NMR, which measures spacial distributions of relaxation-weighted spin density. In 1973, 27 years after the discovery of NMR, Lauterbur and Mansfield & Grannell independently realized that linear field gradients could encode spacial information into an NMR signal. This technique is described in the following sections.

1.3.2 Spacial Encoding

To understand spacial encoding we look at the effect of a linear field gradient on the magnetization, \mathbf{M} , through the Bloch equations. The magnetic field is

given by

$$\mathbf{H} = (H_0 + \mathbf{G}(t) \cdot \mathbf{r})\hat{z}, \quad (1.69)$$

where \mathbf{G} gives the strength of the gradient in each direction of the \hat{z} component of the field. We assume that the gradient is small, that is, $G_z z \ll H_0$ for any z of interest. This field, however, is not experimentally realizable since

$$\nabla \cdot \mathbf{H} = G_z \neq 0.$$

A magnetic field with gradients in a particular direction cannot point in that direction throughout space. A field which is close to (1.69) that can be achieved is

$$\mathbf{H} = (H_0 + \mathbf{G}(t) \cdot \mathbf{r})\hat{z} + G_z(t)(\beta x\hat{x} - (1 + \beta)y\hat{y}), \quad (1.70)$$

where β is an arbitrary constant. Ideally, $-1 \leq \beta \leq 0$, so that (1.70) is as close to (1.69) as possible. In determining the importance of the perturbation introduced by (1.70) first, we note that the \hat{x} and \hat{y} components of \mathbf{G} do not contribute to the discrepancy between (1.69) and (1.70) and can be ignored. Second, it is the magnitude of \mathbf{H} which determines the frequency of precession, so we compare the change in magnitude of \mathbf{H} due to G_z in (1.69) and (1.70). The change in magnitude in (1.69) due to G_z is

$$|\mathbf{H}| - H_0 = G_z z. \quad (1.71)$$

The change due to the corrected field is

$$\begin{aligned} |\mathbf{H}| - H_0 &= \sqrt{(H_0 + G_z z)^2 + G_z^2(\beta^2 x^2 - (1 + \beta)^2 y^2)} - H_0 \\ &= H_0 \left[\sqrt{1 + \frac{2G_z z}{H_0} + \frac{G_z^2(z^2 + \beta^2 x^2 - (1 + \beta)^2 y^2)}{H_0^2}} - 1 \right]. \end{aligned} \quad (1.72)$$

Since $G_z z \ll H_0$, and x , y , and z are all of the same order we use the approximation

$$\sqrt{1+x} \simeq 1 + \frac{x}{2}$$

and obtain

$$|\mathbf{H}| - H_0 = G_z z \left[1 + \frac{G_z z}{2H_0} \left(1 + \frac{\beta^2 x^2 - (1+\beta)^2 y^2}{z^2} \right) \right]. \quad (1.73)$$

Comparing (1.71) and (1.73), the error created in neglecting the \hat{x} and \hat{y} components of (1.70) is

$$G_z z \frac{G_z z}{2H_0} \left(1 + \frac{\beta^2 x^2 - (1+\beta)^2 y^2}{z^2} \right),$$

which is small compared to $G_z z$ as long as $G_z z \ll H_0$ and x , y , and z are near the origin. Therefore in what follows we will neglect the \hat{x} and \hat{y} components of the field and use (1.69) to describe \mathbf{H} .

In complex notation defined in (1.22-1.23) the angular frequency associated with the field becomes

$$\boldsymbol{\omega} = 2\pi\gamma\mathbf{H} = (0, \omega_L + \boldsymbol{\Gamma}(t) \cdot \mathbf{r}), \quad (1.74)$$

where

$$\boldsymbol{\Gamma}(t) = 2\pi\gamma\mathbf{G}(t),$$

and on substitution into (1.24-1.25) give

$$\frac{d\mathbf{M}}{dt} = \left(-i\omega_L - i\boldsymbol{\Gamma}(t) \cdot \mathbf{r} - \frac{1}{T_2} \right) \mathbf{M} \quad (1.75)$$

$$\frac{dM_z}{dt} = \frac{M_0 - M_z}{T_1}. \quad (1.76)$$

The solution to (1.75-1.76) for an arbitrary initial condition, $\mathbf{M}_0 = (M_0, M_{z0})$ is

$$\mathbf{M} = M_0 \exp(-i\omega_L t) \exp\left(-\frac{t}{T_2}\right) \exp(-i\mathbf{k} \cdot \mathbf{r}) \quad (1.77)$$

$$M_z = M_{z0} \exp\left(-\frac{t}{T_1}\right) + M_0 \left(1 - \exp\left(-\frac{t}{T_1}\right)\right), \quad (1.78)$$

where

$$\mathbf{k}(t) = \int_0^t \boldsymbol{\Gamma}(s) ds. \quad (1.79)$$

If the spins are prepared with an excitation $\frac{\pi}{2}$ -pulse then the initial condition is $(M_0, 0)$ and the solution becomes

$$\mathbf{M} = M_0 \exp(-i\omega_L t) \exp\left(-\frac{t}{T_2}\right) \exp(-i\mathbf{k}(t) \cdot \mathbf{r}) \quad (1.80)$$

$$M_z = M_0 \left(1 - \exp\left(-\frac{t}{T_1}\right)\right). \quad (1.81)$$

This gives the magnetization at position \mathbf{r} . The total magnetization is

$$\mathbf{M}_T = \int \mathbf{M}(\mathbf{r}) dV. \quad (1.82)$$

The initial condition, M_0 , introduced above is a function of space. The magnitude is a function of space because of density changes in space. The phase is also a function of space, because of static and r.f. field inhomogeneities. We therefore represent the initial condition as a complex number, M_0 , whose magnitude is M_0 . As in NMR the total transverse magnetization is measured with a resonant antenna. This is equivalent to measuring M_T . Using heterodyne phase sensitive detection both components of \mathbf{M} are measured in the rotating frame. Therefore M_T in the rotating frame from (1.80) and (1.82) is

$$\mathbf{M}_T(t) = \int M_0(\mathbf{r}) \exp\left(-\frac{t}{T_2(\mathbf{r})}\right) \exp(-i\mathbf{k}(t) \cdot \mathbf{r}) dV. \quad (1.83)$$

If we ignore relaxation, then (1.83) becomes

$$\mathbf{M}_T(t) = \mathbf{M}_T(\mathbf{k}(t)) = \int \mathbf{M}_0(\mathbf{r}) \exp(-i \mathbf{k}(t) \cdot \mathbf{r}) dV. \quad (1.84)$$

Equation (1.84) shows that $\mathbf{M}_T(\mathbf{k}(t))$ is the fourier transform of $\mathbf{M}_0(\mathbf{r})$. Since \mathbf{k} is experimentally controlled through the gradients according to (1.79), the fourier transform of $\mathbf{M}_0(\mathbf{r})$ can be measured for all \mathbf{k} . Then,

$$\mathbf{M}_0(\mathbf{r}_0) = \frac{1}{(2\pi)^3} \int \mathbf{M}_T(\mathbf{k}) \exp(i \mathbf{k} \cdot \mathbf{r}_0) d^3\mathbf{k}, \quad (1.85)$$

can be determined.

In practice, $\mathbf{M}_T(\mathbf{k})$ is measured for many \mathbf{k}_i on a grid, and $\mathbf{M}_0(\mathbf{r}_0)$ is calculated using a discrete fast fourier transform, DFFT. Since

$$|\mathbf{M}_0(\mathbf{r}_0)| = M_0(\mathbf{r}_0) \propto \rho(\mathbf{r}_0), \quad (1.86)$$

where ρ is the density of spins, the spacial distribution of spins is determined on a grid. Because the signal, which is proportional to the fourier transform of $\rho(\mathbf{r}_0)$, is measured on a grid of \mathbf{k}_i , it is often referred to as k-space. Much of the art and many of the new advances in MRI come from new ways of sampling $\mathbf{M}_T(\mathbf{k})$. We discuss several of the common techniques for sampling k-space in (§ 1.3.5) and (§ 1.3.3).

If we include relaxation from (1.83) we no longer have the fourier transform of the magnetization. Instead we have

$$\mathbf{M}_T(t) = \int \mathbf{f}(\mathbf{r}, \mathbf{k}) \mathbf{M}_0(\mathbf{r}) \exp(-i \mathbf{r} \cdot \mathbf{k}(t)) dV, \quad (1.87)$$

where

$$\mathbf{f}(\mathbf{r}, \mathbf{k}) = \exp\left(-\frac{t(\mathbf{k})}{T_2(\mathbf{r})}\right),$$

and $t(k)$ is the inverse of (1.79). If we assume that the acquisition time is small compared to T_2 then we can expand $t(\mathbf{k})$ about the center of the acquisition window, t_a and get

$$t(\mathbf{k}) = t_a + \dots$$

Upon substitution in (1.87), we obtain

$$\mathbf{M}_T(\mathbf{k}) = \int \mathbf{M}_0(\mathbf{r}) \exp\left(-\frac{t_a}{T_2(\mathbf{r})}\right) \exp(-i \mathbf{r} \cdot \mathbf{k}(t)) dV, \quad (1.88)$$

and we again have a fourier relation between the signal, $\mathbf{M}_T(\mathbf{k})$, and $\mathbf{M}_0(\mathbf{r})$.

From (1.88) we have

$$\rho(\mathbf{r}) \exp\left(-\frac{t_a}{T_2(\mathbf{r})}\right) \propto M_0(\mathbf{r}_0) = |\mathbf{M}_0(\mathbf{r}_0)|,$$

where $\mathbf{M}_0(\mathbf{r}_0)$ is determined from (1.85). Therefore, we measure the spacial distribution of the density of spins weighted by the loss of signal due to T_2 relaxation after t_a seconds.

1.3.3 Sampling k-space

Determining the way that $\mathbf{M}_T(\mathbf{k})$ will be sampled is an important part of MRI. Since $\mathbf{k}(t)$ is a function of time through (1.79), an analogy to a trajectory through k-space is often made. After an excitation pulse as described above, \mathbf{k} is at the origin of k-space. The gradients control the velocity of motion through k-space. Sampling of $\mathbf{M}_T(\mathbf{k})$ typically occurs at a constant rate with the gradients on during the acquisition, so that many points in k-space can be sampled. While the fastest imaging techniques attempt to sample all of k-space in a single acquisition, most often, only a portion of k-space is sampled after

an excitation. After waiting for a time, T_r , called the repetition time, some of the spins will have relaxed back to equilibrium, a new excitation pulse can be applied, and another section of k-space sampled.

1.3.4 Selective Excitation

Often it is useful to be able to apply a spacially selective excitation pulse. The most common use of these pulses is to reduce acquisition time by limiting the sample to a thin slice, thus eliminating one dimension of k-space which must be acquired. There is a large time savings since only two-dimensions of k-space must be collected. The simplest way to eliminate a dimension is to ignore it. If we ignore the \hat{z} direction, then the signal acquired will be,

$$\mathbf{M}_T(\mathbf{k}) = \int_{-\frac{\Delta z}{2}}^{\frac{\Delta z}{2}} \iint M_0(\mathbf{r}) \exp(-i \mathbf{k} \cdot \mathbf{r}) dx dy dz, \quad (1.89)$$

where Δz is the thickness of the sample in the \hat{z} direction. If k_z is set to zero, by setting the \hat{z} gradient to zero, then

$$\mathbf{M}_T(k_x, k_y) = \iint \overline{M_0(x, y)} \exp(i(k_x x + k_y y)) dx dy, \quad (1.90)$$

where

$$\overline{M_0(x, y)} = \int_{-\frac{\Delta z}{2}}^{\frac{\Delta z}{2}} M_0(\mathbf{r}) dz.$$

Equation (1.90) shows that $\mathbf{M}_T(k_x, k_y)$ is the two-dimensional fourier transform of $\overline{M_0(x, y)}$, and

$$\overline{M_0(x_0, y_0)} = \frac{1}{(2\pi)^2} \iint \mathbf{M}_T(k_x, k_y) \exp(i(k_x x_0 + k_y y_0)) dk_x dk_y. \quad (1.91)$$

By simply ignoring one dimension, we are able to measure the projection or average over that dimension as a function of the remaining dimensions. By limiting the sample to a thin slice in the \hat{z} direction, either by physical sectioning or by selective production of transverse magnetization,

$$\overline{M_0(x, y)} \simeq M_0(x, y),$$

and a good approximation to a two-dimensional slice is obtained.

As mentioned above, one way to achieve slice selection is physical sectioning, but one of the powers of MRI is the ability to perform this sectioning with the sample intact and often alive. A spacially selective r.f. pulse is produced by applying an excitation pulse in the presence of a linear magnetic field gradient. For a gradient along the \hat{z} axis, the angular frequency associated with the field, in complex notation defined in (1.22-1.23) is

$$\boldsymbol{\omega} = 2\pi\gamma\mathbf{H} = (\Omega_1(t)\exp(-i\omega_1 t), \omega_L + \Gamma_z(t)z). \quad (1.92)$$

The consequences of this field can be qualitatively understood in the following way. Excitation by a $\frac{\pi}{2}$ -pulse is a resonance phenomenon. As described in (§1.2.5) the resonance condition $\omega_1 = \omega_L$ must be met in order to rotate \mathbf{M} into the transverse plane. By applying a gradient during the application of this pulse, we only rotate spins with

$$\omega_L + \Gamma_z(t)z = \omega_L,$$

and we only excite spins with $z = 0$. Clearly the slice will have a width, since any pulse of finite width will contain a range of frequencies, which can be determined by fourier analysis. The width of the frequency range and the strength of the gradient will determine the thickness of the slice. If the pulse

has a width $\Delta\omega_1$ then a slice of transverse magnetization with thickness

$$\Delta z = \frac{\Delta\omega_1}{\Gamma_z(t)} \quad (1.93)$$

occurs. While this analysis is qualitatively correct, we can obtain a quantitative understanding by looking at solutions of the Bloch equations for fields defined by (1.92).

The Bloch equations defined by (1.92), in the rotating frame, with $\omega_1 = \omega_L$, and ignoring relaxation are

$$\frac{d\mathbf{M}'}{dt} = -i [\mathbf{M}'\Gamma_z(t)z - M_z\Omega_1(t)] \quad (1.94)$$

$$\frac{dM_z}{dt} = \text{Im}(\mathbf{M}'^*\Omega_1(t)), \quad (1.95)$$

where \mathbf{M}' is the transverse magnetization in the rotating frame. Comparison with (1.24-1.25) shows that these represent the most general Bloch equations. Like most sets of coupled first-order linear differential equations the general solution cannot be expressed in simple functions, but must be given in terms of infinite series. While infinite series are perfectly good solutions, very little insight can be gained from them. As a result (1.94-1.95) are often analyzed using a small flip angle approximation (Hoult, 1979; Hinshaw & Lent, 1983; Bailes & Bryant, 1984). Under this approximation we use the fact that,

$$\frac{d|\mathbf{M}'|^2}{dt} = \frac{d}{dt}(M'M'^* + M_z^2) = \frac{dM'}{dt}M'^* + M'\frac{dM'^*}{dt} + 2\frac{dM_z}{dt}M_z = 0 \quad (1.96)$$

which can be derived from (1.94-1.95). Equation (1.96) shows that $|\mathbf{M}'|$ is constant and therefore equal to the initial value, M_0 . Solving for M_z :

$$M_z = M_0 \sqrt{1 - \frac{M'M'^*}{M_0^2}}. \quad (1.97)$$

In the small angle approximation, we assume that $M' \ll M_0$ and

$$M_z \simeq M_0 \left(1 - \frac{M'M'^*}{2M_0^2} + \dots \right). \quad (1.98)$$

Only the leading term of (1.98) is retained which leaves the approximation

$$M_z \simeq M_0.$$

In this approximation, the solution to (1.94-1.95), for an initial condition $(0, M_0)$, is

$$M'(t) = i M_0 \exp(-i k_z(t)z) \int_0^t \Omega_1(s) \exp(i k(s)z) ds, \quad (1.99)$$

where

$$k_z(t) = \int_0^t \Gamma_z(s) ds.$$

If $\Gamma_z(t) = \Gamma_0$ and the duration of the pulse is τ then (1.99) becomes

$$M'(z) = i M_0 \exp(-i \tau \Gamma_0 z) \int_0^\tau \Omega_1(s) \exp(i \Gamma_0 z s) ds, \quad (1.100)$$

at $t = \tau$. Equation (1.100) shows that the spacial distribution of the excitation along the \hat{z} direction is the inverse fourier transform of the r.f. waveform in time scaled by Γ_0 and modulated by a spacial phase factor:

$$\exp(-i \tau \Gamma_0 z).$$

Therefore, for small angle rotations, the r.f. waveform should be the fourier transform of the desired slice profile.

The phase factor presents a problem since the signal is summed over all space. This phase factor would cause the cancellation of some signal by other

signal in the slice at a different phase. As a result the slice must be re-phased. First, we notice that the fourier transform in (1.100) is not centered about zero, and thus adds to the phase factor. If we make a change of integration variable so that the integral is centered about zero we obtain:

$$\mathbf{M}'(z) = i M_0 \exp\left(-\frac{i \tau \Gamma_0 z}{2}\right) \int_{-\frac{\tau}{2}}^{\frac{\tau}{2}} \Omega_1\left(s + \frac{\tau}{2}\right) \exp(i \Gamma_0 z s) ds, \quad (1.101)$$

and the new phase factor is

$$\exp\left(-\frac{i \tau \Gamma_0 z}{2}\right).$$

We can remove this factor by the application of a gradient along the same axis but with opposite sign. From (1.77) we find that the application of a constant gradient of amplitude $-\Gamma_0$ and duration $\frac{\tau}{2}$ in the rotating frame, ignoring relaxation, and for an arbitrary initial condition $(\mathbf{M}_0, 0)$, gives

$$\mathbf{M}'(z) = M_0 \exp\left(\frac{i \tau \Gamma_0 z}{2}\right).$$

Evaluating with initial value, \mathbf{M}_0 , from (1.101),

$$\mathbf{M}'(z) = i M_0 \int_{-\frac{\tau}{2}}^{\frac{\tau}{2}} \Omega_1\left(s + \frac{\tau}{2}\right) \exp(i \Gamma_0 z s) ds, \quad (1.102)$$

and the phase factor is eliminated. By taking the fourier transform of both sides of (1.102) and solving for the r.f. waveform amplitude we obtain,

$$\Omega_1\left(t + \frac{\tau}{2}\right) = \begin{cases} -\frac{i \Gamma_0}{2\pi M_0} \int \mathbf{M}'(z) \exp(-i \Gamma_0 z t) dz & |t| \leq \frac{\tau}{2} \\ \text{undetermined} & |t| > \frac{\tau}{2} \end{cases}. \quad (1.103)$$

For selection of a thin slice, the slice profile should be

$$\mathbf{M}'(z) = \begin{cases} M_0 & |z| \leq \frac{\Delta z}{2} \\ 0 & |z| > \frac{\Delta z}{2} \end{cases}. \quad (1.104)$$

Evaluating (1.103) with (1.104) we obtain,

$$\Omega_1(t) = -\frac{i \sin\left(\frac{\Gamma_0 \Delta z t}{2}\right)}{\pi t}. \quad (1.105)$$

Since (1.105) is of infinite duration in practice it must be truncated. This truncation causes the slice profile to be slightly different. By using a similar procedure, many different spacially selective pulses can be derived (Pauly, Nishimura & Macovski, 1989). For many spacially selective excitations the small angle approximation works remarkably well, even up to angles of $\pi/2$. It should also be noted that this technique can be used to move the center of the excitation region by changing the base frequency, ω_1 , of the r.f. excitation. In this case, spins at

$$z = \frac{\omega_1 - \omega_L}{\Gamma_0}$$

will be excited.

1.3.5 Pulse Sequence

Introduction

Pulse sequence design is an important part of MRI. A pulse sequence is a timing diagram for the gradients, r.f. pulses, and data acquisition. In a standard system, there are three gradient channels, one for each direction; there are two r.f. channels, either one for real and one for imaginary, or one for magnitude and one for phase; and finally, there are two data acquisition channels, one for storing each component of \mathbf{M}_T . If a channel is missing from a diagram, it is assumed zero. Also, the two acquisition channels are usually displayed on a single line. Shaded areas on the same line are of equal area. Since most

sequences consist of many acquisitions, only one period of repetition time, T_r , is shown. Any subsequent changes are displayed as dotted lines. The gradient lines are not labeled by x , y , and z , as this may change from one scan to another. Instead they are usually labeled by slice, phase, and frequency. The slice direction is the direction of the spatially selective excitation, if there is any. The frequency direction refers to the gradient direction which is on during the acquisition. Since \mathbf{k} is moving through k-space in that direction, the frequency spectrum of the acquisition gives spatial information about that direction. The phase direction refers to the prescription of the displacement or phase in k-space at the start of acquisition. The magnitude of the phase gradient is typically changed after each acquisition, so that a different part of k-space may be sampled. In the following sections we describe several standard pulse sequences and their k-space trajectories.

Gradient Recalled Echo

A two-dimensional Gradient Recalled Echo, GRE, pulse sequence is shown in figure 1.1. During the first time interval labeled *sinct*, we apply a slice selective excitation $\frac{\pi}{2}$ -pulse. This produces M_T in a region with a user-definable thickness and position as described in (§ 1.3.4). During the second time period labeled *pet*, for phase encoding time, there are gradients on all three channels. The gradient on the slice channel re-phases the spins from the phase induced by the slice selective pulse (see § 1.3.4). The gradients on the phase channel and frequency channels define a path in k-space from the initial position at the center to the beginning of the next line of k-space to be acquired. This trajectory is shown in figure 1.2 as a dotted line. Next, during the time interval labeled *aqc*, data is acquired while the gradient in the frequency direction is

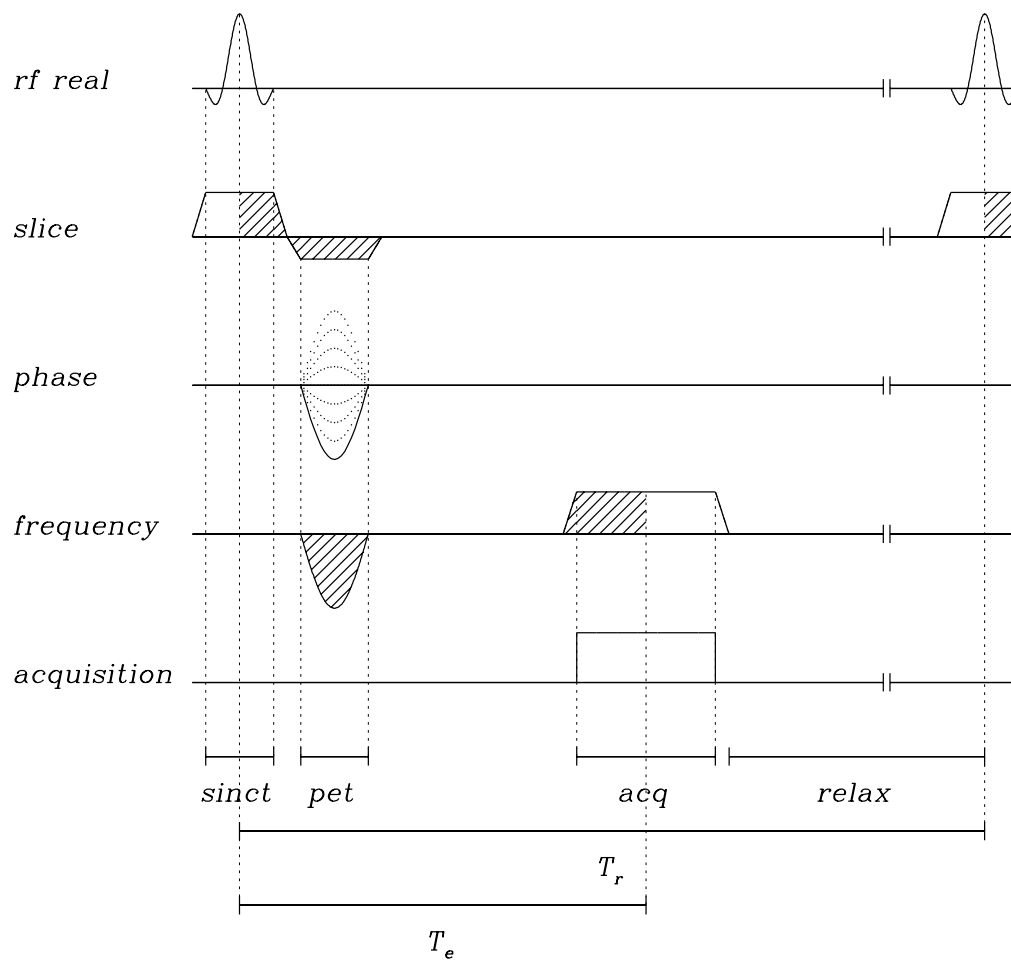


Figure 1.1: Pulse sequence for two-dimensional GRE.

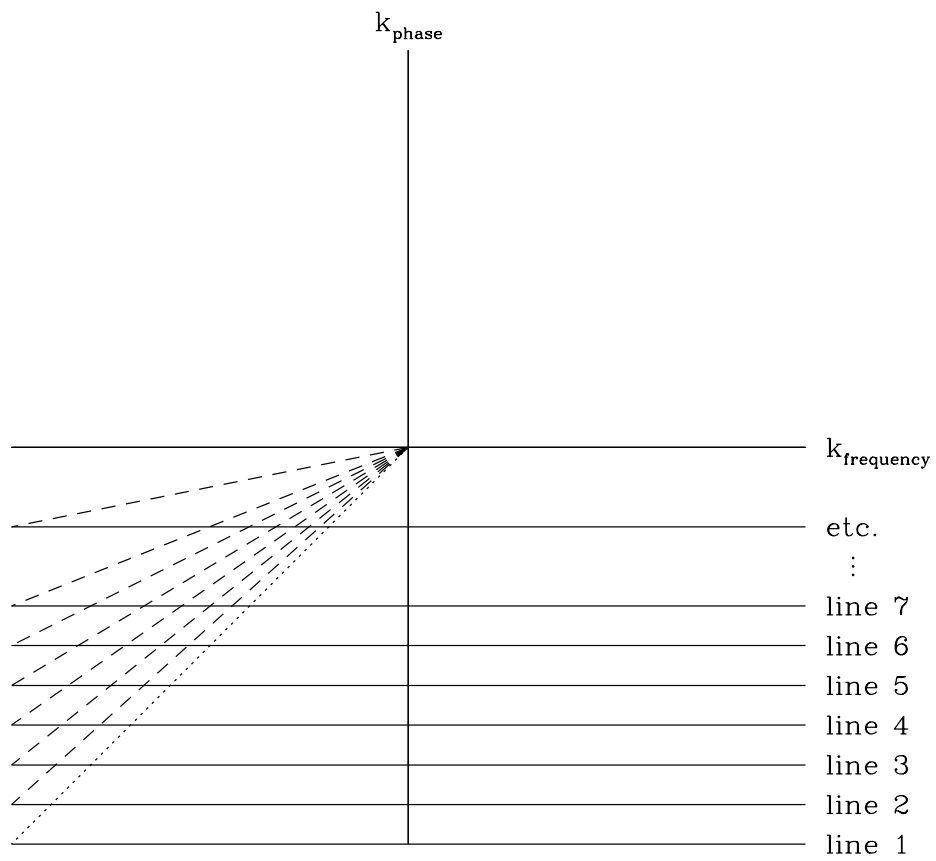


Figure 1.2: K-space trajectory for two-dimensional GRE.

on. The trajectory through k-space during the acquisition is shown as a solid line in figure 1.2. The shaded area in the first pulse on the acquisition line is equal to the shaded area on the second pulse. Through (1.79), this implies that the center of k-space is collected at the center of the acquisition. Finally, during the period labeled *relax* the spins are allowed to relax until the sequence is repeated a time, T_r , after the start of the sequence. During the time, *pet*, on subsequent repetitions, the phase gradient is changed, so that a different line in k-space is acquired. This is shown in figure 1.1 and figure 1.2 by the dashed lines. The frequency gradient remains the same for each acquisition. In this way, the acquisition always begins at the same value of $k_{\text{frequency}}$ but the value of k_{phase} is incremented.

For a three-dimensional acquisition, only a small addition is needed to the pulse sequence. Such a sequence is shown in figure 1.3. The addition is an incrementing gradient added to the slice re-phasing gradient. We acquire a three-dimensional volume of k-space as depicted in figure 1.4 by incrementing this gradient in a nested loop with the phase gradient. This increases the number of acquisitions needed to collect this data by a factor of the number of planes of k-space data to be collected.

The time required to collect the data, assuming that \hat{z} is the slice direction, \hat{y} is the phase direction, and \hat{x} is the frequency direction, is given by

$$\text{Total Acquisition Time} = N_a N_y N_z T_r, \quad (1.106)$$

where N_a is the number of times each line in k-space is collected and averaged, and N_y and N_z are the number of points to be determined along the \hat{y} and \hat{z} directions.

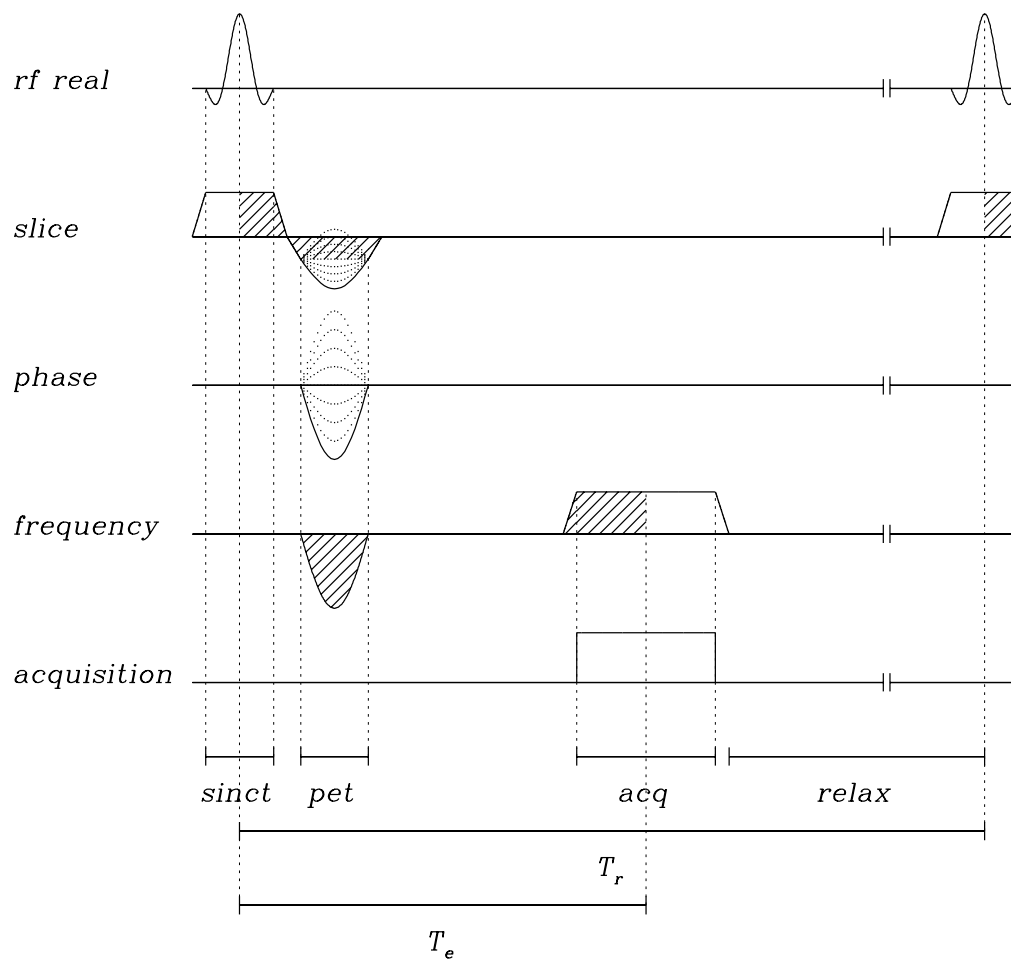


Figure 1.3: Pulse sequence for three-dimensional GRE.

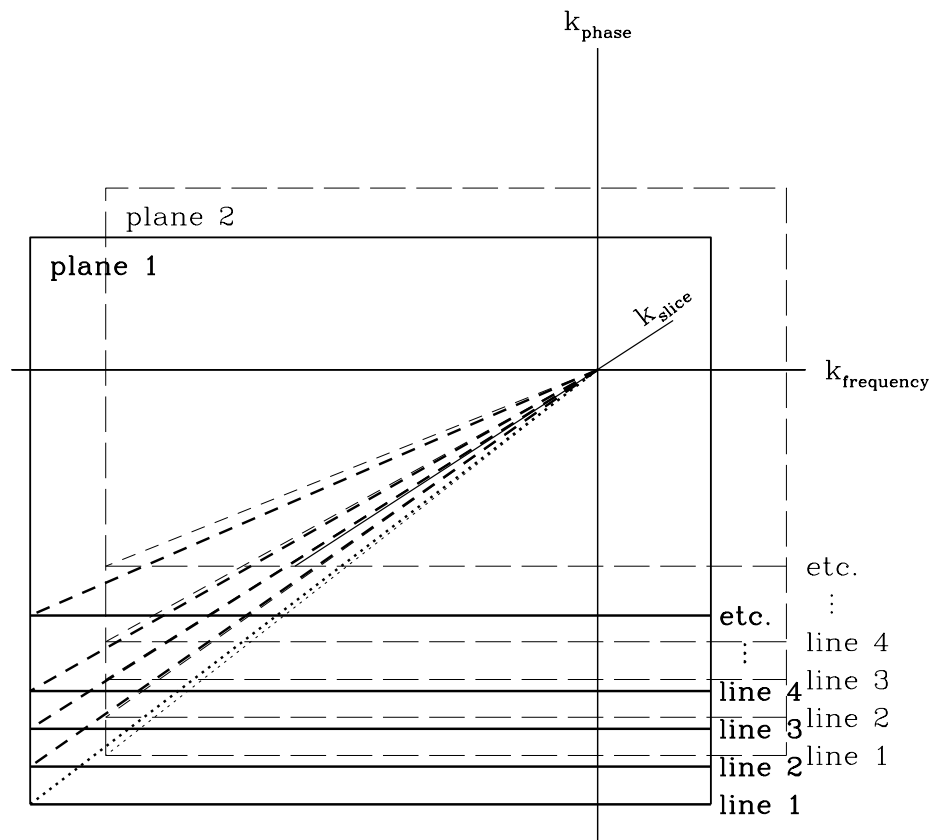


Figure 1.4: K-space trajectory for three-dimensional GRE.

Limited Flip Angle

From (1.106), one obvious way to reduce the time of the acquisition is to reduce T_r . Unfortunately, the amount of signal depends on the length of T_r . According to (1.35), M_z recovers with a time constant T_1 . The magnitude of M_T which is created in an excitation pulse is proportional to the magnitude of M_z at the time of the pulse. As we make T_r shorter, there is less time for the spins to relax and M_z is smaller at the time of the next excitation pulse. This makes M_T smaller, and hence, diminishes the signal. One solution to this problem is to use an α -pulse instead of a $\frac{\pi}{2}$ -pulse for excitation. An α -pulse produces $M_{z0} \sin(\alpha)$ transverse magnetization and leaves $M_{z0} \cos(\alpha)$ longitudinal magnetization. After multiple applications of the α -pulse a steady-state is reached. It turns out that for a given T_r there is an optimal angle,

$$\alpha_E = \cos^{-1}\left[\exp\left(\frac{-T_r}{T_1}\right)\right],$$

called the Ernst angle which produces maximal steady state signal (Ernst, Bodenhausen & Wokaun, 1987). By choosing this angle the T_r may be shortened without losing as much signal as would have been lost if a $\frac{\pi}{2}$ -pulse was used. This technique may be used to shorten the acquisition time in many pulse sequences.

Echo Planer Imaging

In Echo Planer Imaging, EPI, all of k-space is measured at one time. EPI begins just like GRE. Phase and frequency gradients move to point A in figure 1.6 and then the first line of k-space is acquired from point A to point B. Then instead of waiting, a small gradient on the phase channel increments the position in

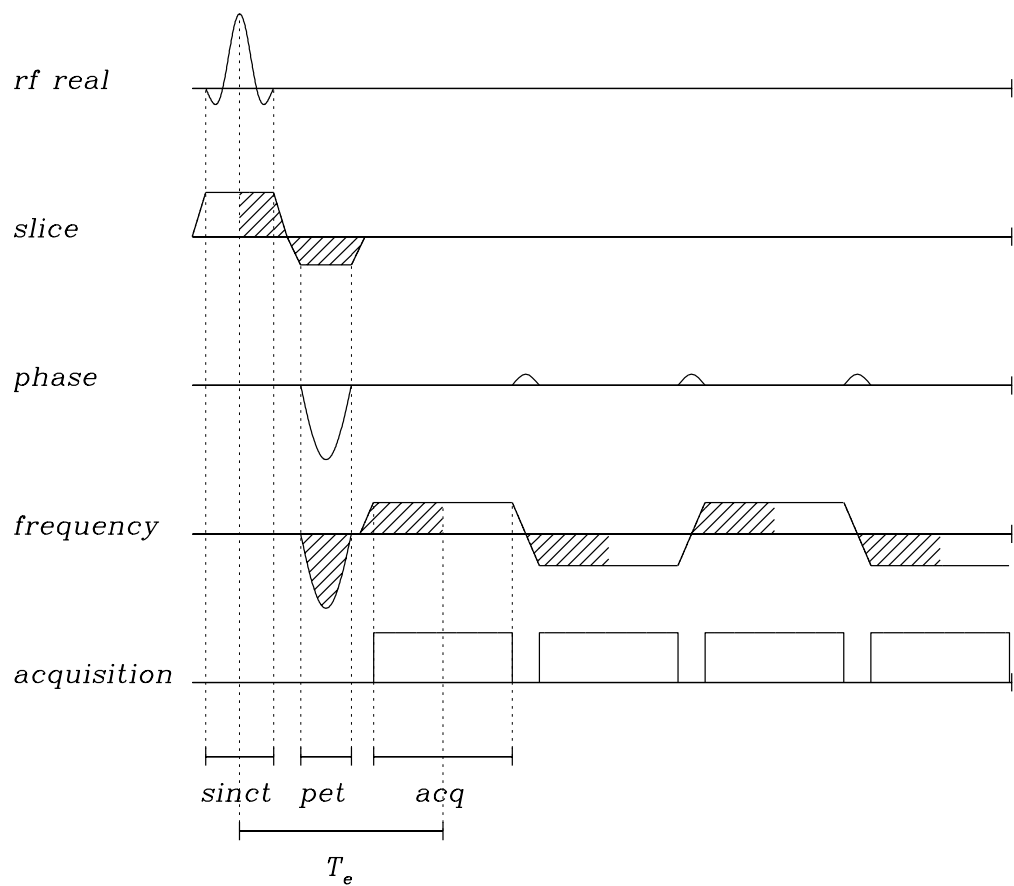


Figure 1.5: Pulse sequence for EPI.

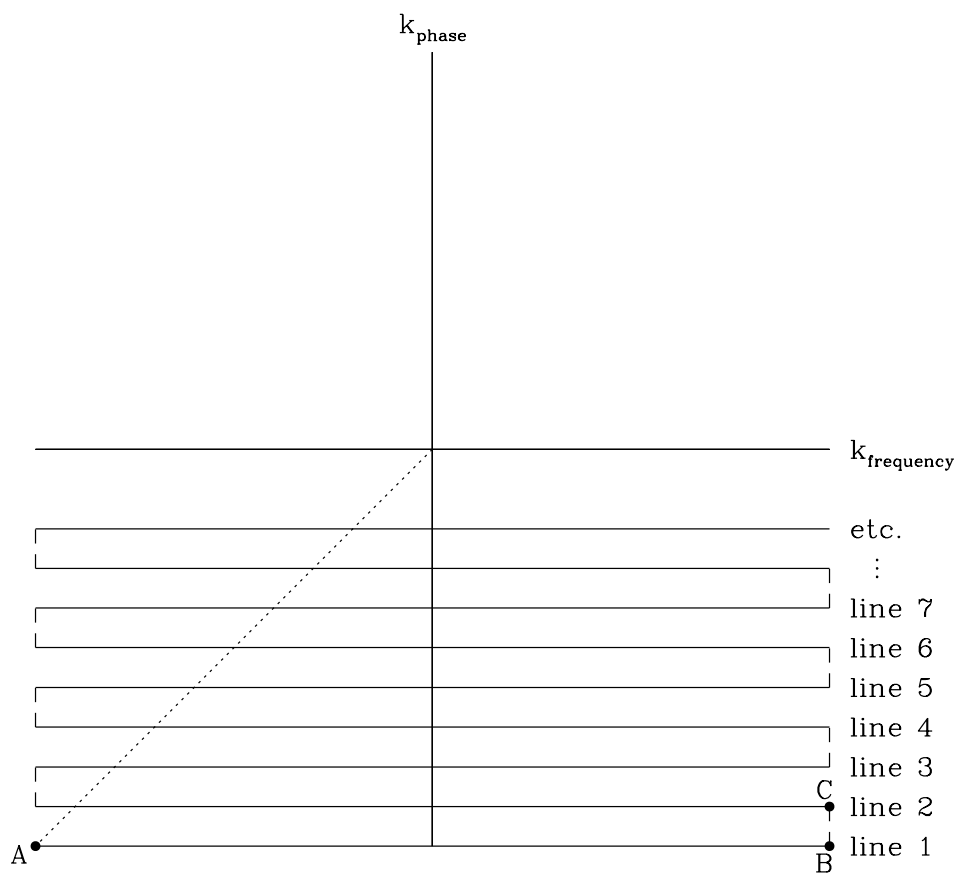


Figure 1.6: K-space trajectory for EPI.

k-space to point C where a second line is acquired traversing k-space in the opposite direction. We repeat the process back and forth across k-space until we collect all k-space points. Variants of this sequence include sampling sub-domains of k-space in this manner, then waiting for relaxation and repeating the process on another sub-domain until all of k-space is sampled. This is one of the fastest sampling techniques known. Another related technique is called spiral sampling. In this technique, gradients produce a spiral trajectory through k-space collecting data during the whole trajectory.

Spin Echo

In the previous pulse sequences, the signal is sampled from the f.i.d. following the excitation pulse. This signal decays with a decay constant T_2^* , as defined in (§ 1.2.7), which is often much shorter than T_2 . For this reason many pulse sequences use a π -pulse to produce a spin echo to increase the signal. As in the sequence shown in figure 1.7, we make the spin echo position coincident with the sampling of the center of k-space. This sequence uses the same trajectory as in figure 1.2, except that the application of the π -pulse reflects the position about the origin. This is shown in figure 1.8 by the dotted lines. Because of this reflection, the sign of the frequency channel gradients are the same on both sides of the π -pulse. Without the intervening π -pulse the gradient, which is on during the acquisition, would continue to move \mathbf{k} further away from the origin than the position at the end of the first pulse. With the π -pulse this gradient moves \mathbf{k} in the same direction as the first pulse but the starting point has been reflected to the other side of the origin. With this sequence the signal is weighted by relaxation due to T_2 , not T_2^* . In many situation the difference between these two relaxation times can be more than an order of magnitude.

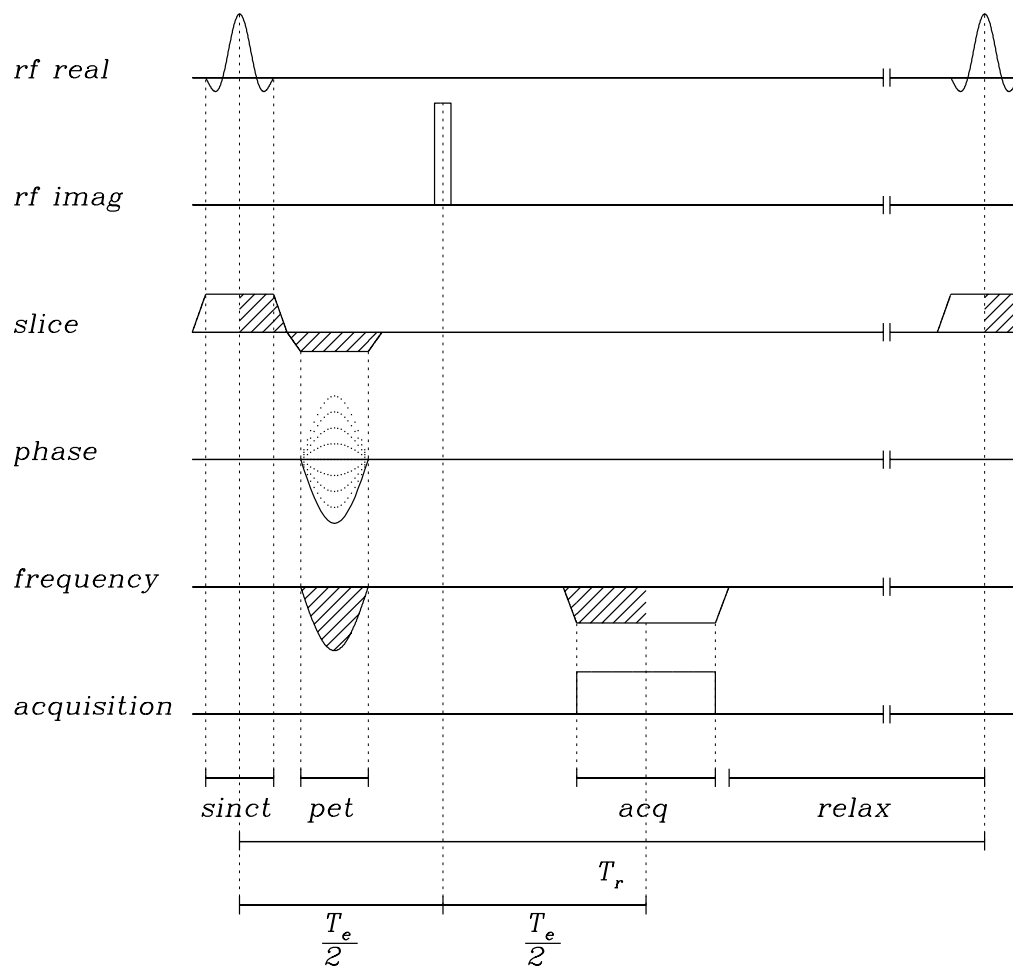


Figure 1.7: Pulse sequence for SE.

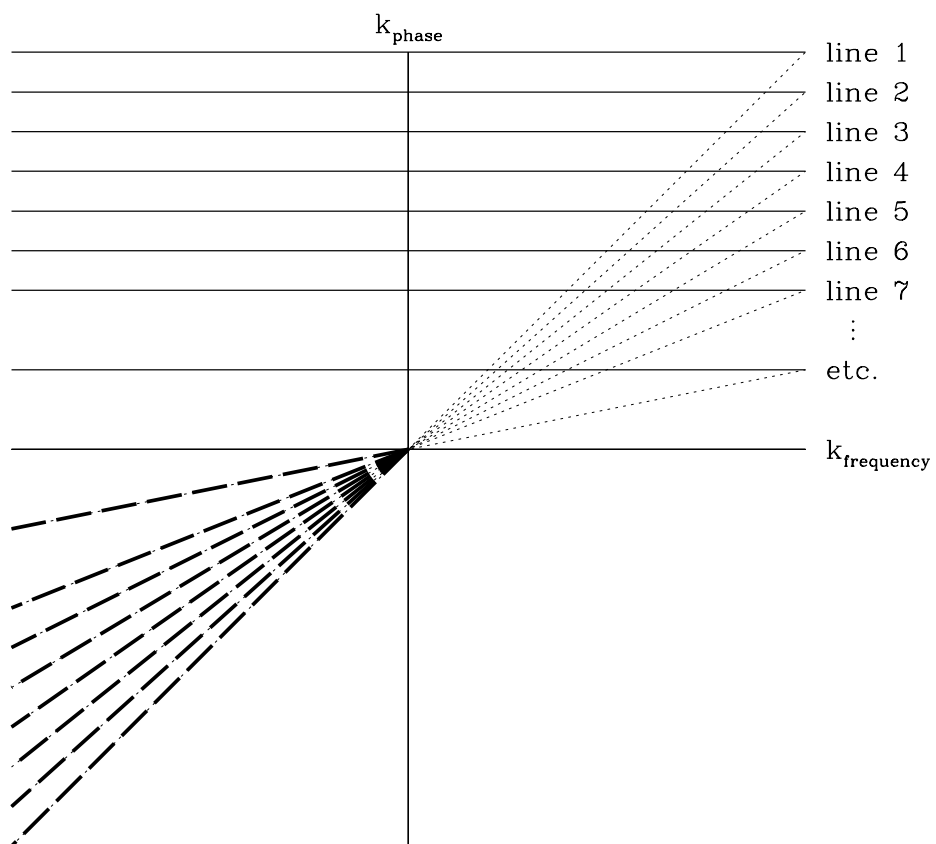


Figure 1.8: K-space trajectory for SE.

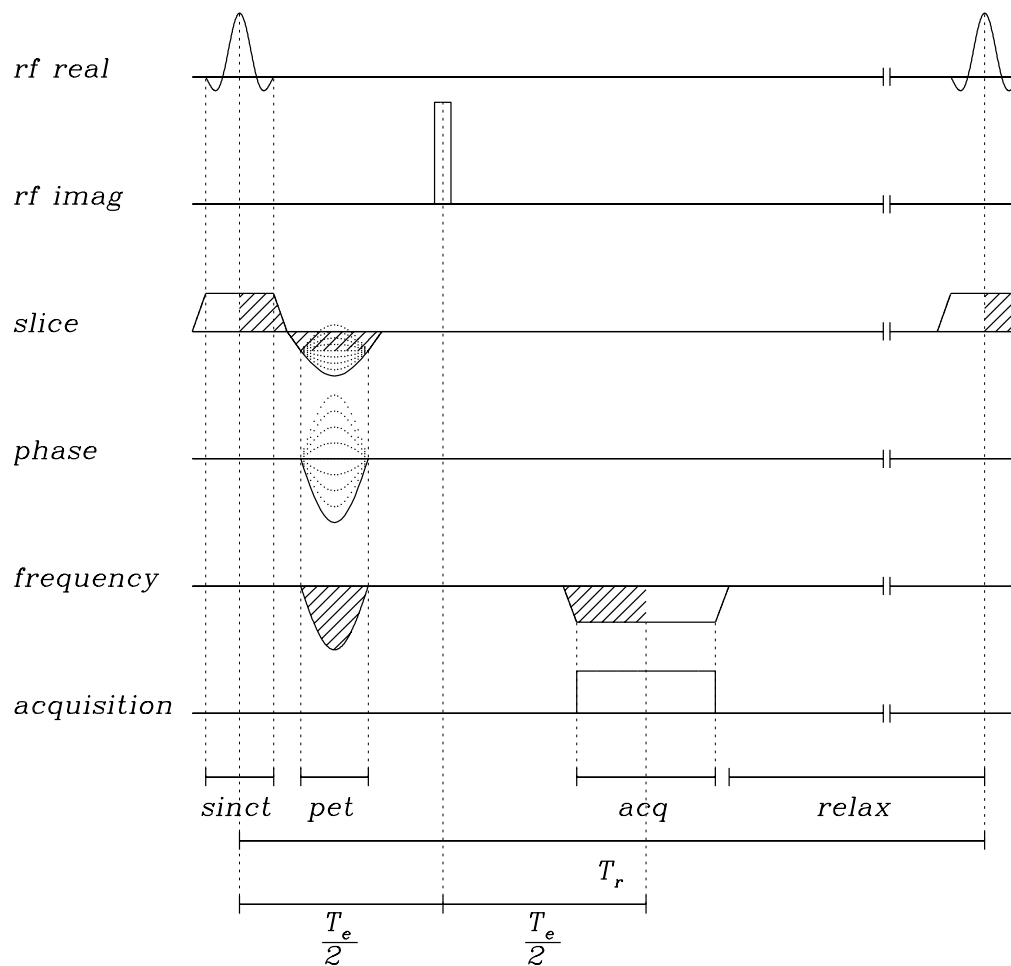


Figure 1.9: Pulse sequence for three-dimensional SE.

Like the GRE sequence SE is extended to three-dimensions easily by the addition of an incrementing gradient added to the slice re-phasing gradient. As in the three-dimensional GRE sequence this gradient is incremented in a nested loop with the phase gradient. Such a sequence is shown in figure 1.9

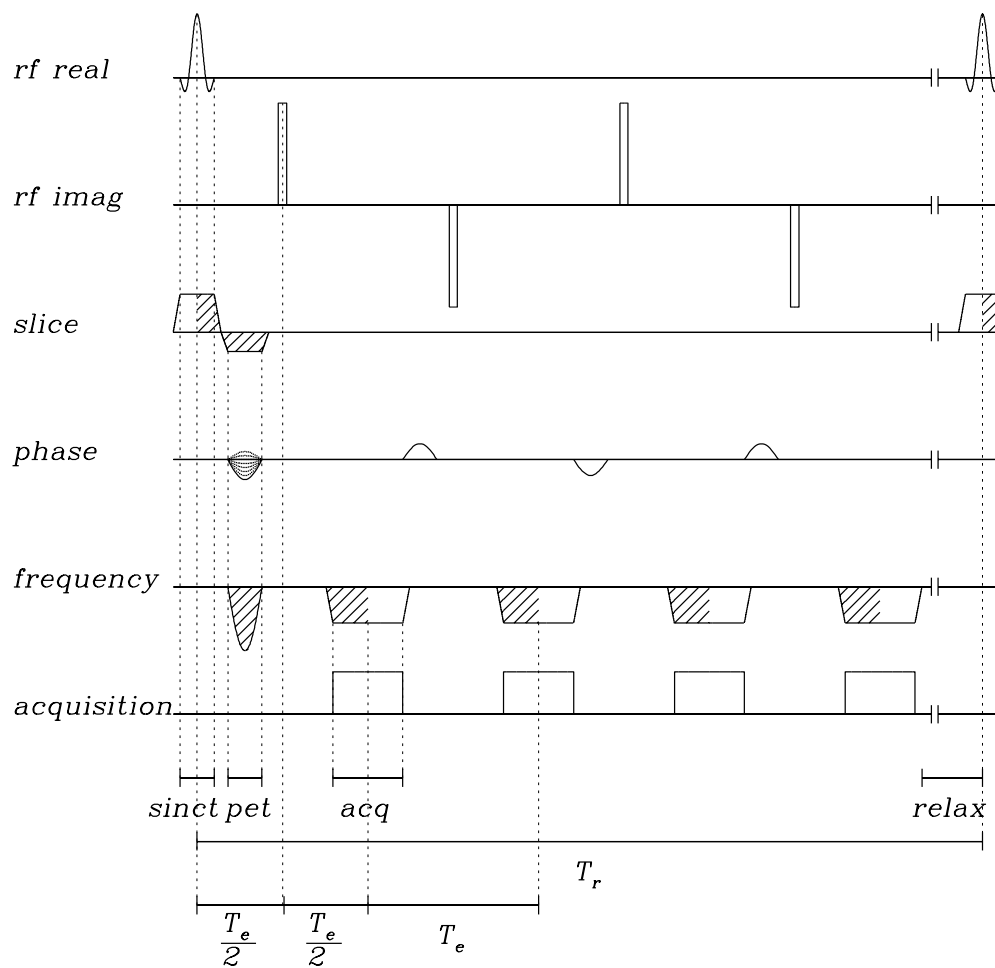


Figure 1.10: Pulse sequence for FSE.

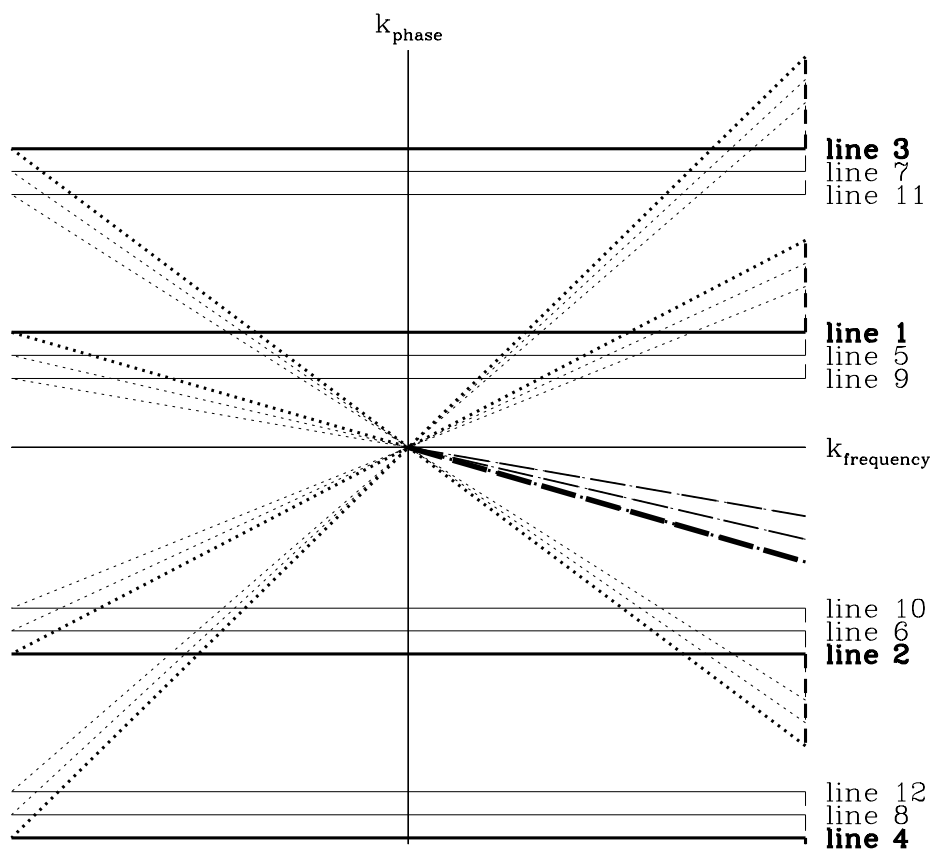


Figure 1.11: K-space trajectory for FSE.

Fast Spin Echo

Fast Spin Echo, FSE, uses multiple π -pulses to produce multiple spin echoes from the same excitation pulse. As shown in figure 1.10, this sequence begins just like a SE sequence with the application of a π -pulse a time, $T_e/2$, after the $\frac{\pi}{2}$ -pulse, and acquisition of the spin echo formed at time, T_e . Then a second π -pulse is applied a time, $3T_e/2$, after the excitation pulse, which causes a second echo to be formed at a time, $2T_e$. This can be understood by noting that the signal at the first echo is the same as that just after the initial excitation, except decreased by the factor,

$$\exp\left(-\frac{T_e}{T_2}\right).$$

The signal evolves in the same way during the second period of duration, T_e , and at time $2T_e$ an echo forms with its intensity decreased by the factor,

$$\exp\left(-\frac{2T_e}{T_2}\right).$$

In general, after n echoes, the signal will be decreased by

$$\exp\left(-\frac{nT_e}{T_2}\right).$$

In FSE data is acquired during each echo. Then the system is allowed to relax, and we repeat the process. The k-space trajectory during a four echo sequence or echo train is depicted in figure 1.11. It is complicated because of the multiple reflection about the origin caused by the π -pulses. Between each echo, \mathbf{k} moves further out in k-space. After the four echoes, we allow the system to relax, and then we acquire four more echoes. During each echo train, we acquire four different lines of k-space. These are often interleaved, as shown in figure 1.11.

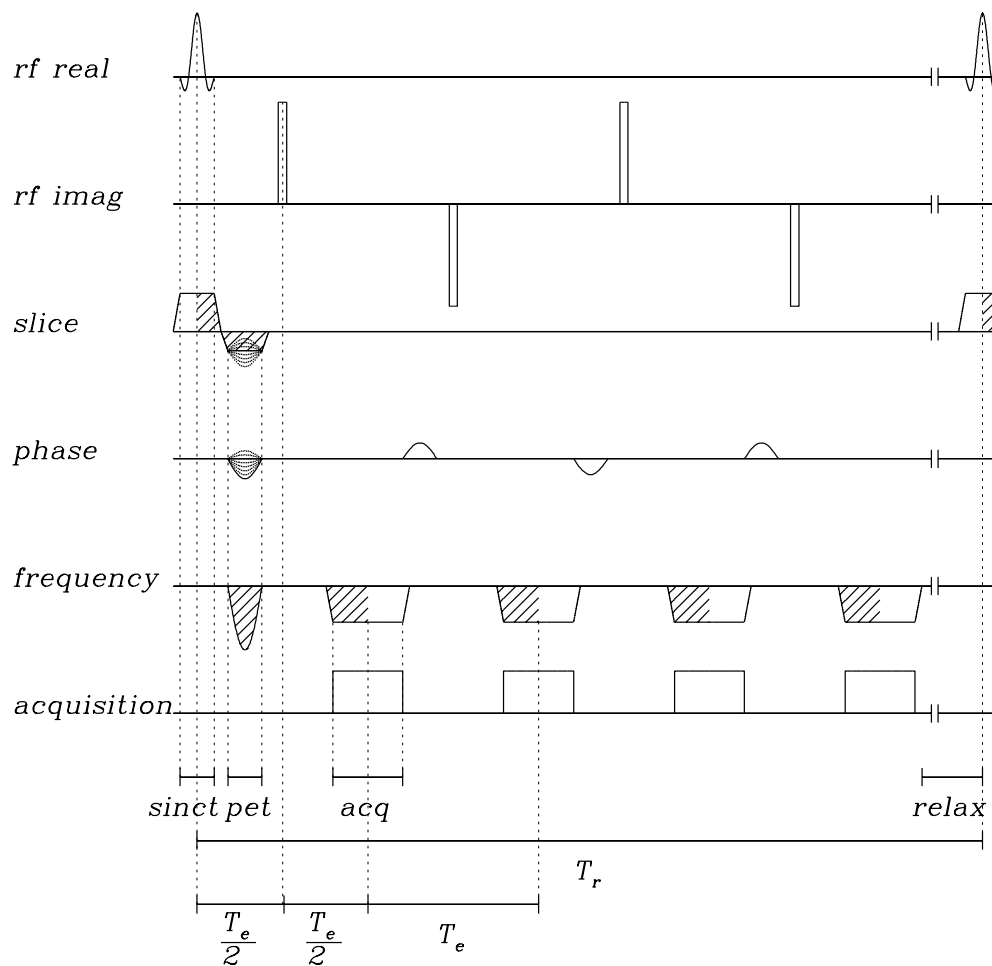


Figure 1.12: Pulse sequence for three-dimensional FSE.

This puts echoes from the same position in the train together and cuts down on artifacts produced because of the differential weighting of different lines of k-space.

We make the three-dimensional version of this sequence in the same way as in the SE and GRE pulse sequences. We show the additions in figure 1.12.

1.4 Velocity Measurement with MRI

1.4.1 Introduction

In the previous sections, we have ignored all effects due to motion of the sample. In fact, motion of the sample or within the sample can rarely be ignored. Indeed, MRI and NMR are extremely sensitive to motion. This sensitivity is responsible for severe artifacts in clinical imaging due to blood flow, breathing, bowel motion, eye movement, etc. However, this sensitivity can be turned to an advantage in the measurement of flow, as will be explained in the following sections.

1.4.2 Flow in the Presence of a Linear Gradient

In developing the response of a sample to linear field gradients in (§ 1.3.2), the position of the spin, \mathbf{r} , was considered time independent. However, in a flowing system, \mathbf{r} is a function of time. Thus, a spin with Lagrangian coordinate trajectory, $\mathbf{r}(t)$, experiences the field,

$$\mathbf{H} = (H_0 + \mathbf{G}(t) \cdot \mathbf{r}(t))\hat{z}, \quad (1.107)$$

in the presence of a gradient $\mathbf{G}(t)$. This equation is the generalization of (1.69). The complex angular frequency associated with (1.107) is

$$\boldsymbol{\omega} = 2\pi\gamma\mathbf{H} = (0, \omega_L + \boldsymbol{\Gamma}(t) \cdot \mathbf{r}(t)), \quad (1.108)$$

where as before

$$\boldsymbol{\Gamma}(t) = 2\pi\gamma\mathbf{G}(t).$$

This leads to Bloch equations:

$$\frac{d\mathbf{M}}{dt} = \left(-i\omega_L - i\boldsymbol{\Gamma}(t) \cdot \mathbf{r}(t) - \frac{1}{T_2}\right)\mathbf{M} \quad (1.109)$$

$$\frac{dM_z}{dt} = \frac{M_0 - M_z}{T_1}. \quad (1.110)$$

The solution to (1.109-1.110) for an arbitrary initial condition, $\mathbf{M}_0 = (M_0, M_{z0})$ in the rotating frame is

$$\mathbf{M} = M_0 \exp\left(-\frac{t}{T_2}\right) \exp(-i Q(t)) \quad (1.111)$$

$$M_z = M_{z0} \exp\left(-\frac{t}{T_1}\right) + M_0 \left(1 - \exp\left(-\frac{t}{T_1}\right)\right), \quad (1.112)$$

where

$$Q(t) = \int_0^t \boldsymbol{\Gamma}(s) \cdot \mathbf{r}(s) ds. \quad (1.113)$$

Note that, $\mathbf{r}(t)$ is a function of time and cannot be pulled out of the integral in (1.113). If we expand $\mathbf{r}(t)$ in a Taylor series, then

$$Q(t) = \sum_{n=0}^{\infty} \mathbf{K}_n(t) \cdot \mathbf{R}_n, \quad (1.114)$$

where

$$\mathbf{K}_n(t) \equiv \frac{1}{n!} \int_0^t \boldsymbol{\Gamma}(s) s^n ds, \quad (1.115)$$

and

$$\mathbf{R}_n = \left. \frac{d^n \mathbf{r}(t)}{dt^n} \right|_{t=0}. \quad (1.116)$$

$\mathbf{K}_n(t)$ is the n-th moment of the gradient, and \mathbf{R}_n is the n-th derivative of the spin's motion. Specifically, \mathbf{R}_0 is the position at time zero, \mathbf{r}_0 , \mathbf{R}_1 is the velocity at time zero, \mathbf{v}_0 , and \mathbf{R}_2 is the acceleration at time zero, \mathbf{a}_0 . From (1.79), we find

$$\mathbf{k}(t) = \mathbf{K}_0(t).$$

If we truncate the expansion at $\mathcal{O}(t^2)$, ignoring the acceleration and higher derivatives, then the solution to (1.109-1.110) becomes

$$\mathbf{M} = M_0 \exp\left(-\frac{t}{T_2}\right) \exp(-i \mathbf{k} \cdot \mathbf{r}_0) \exp(-i \mathbf{K}_1 \cdot \mathbf{v}_0) \quad (1.117)$$

$$M_z = M_{z0} \exp\left(-\frac{t}{T_1}\right) + M_0 \left(1 - \exp\left(-\frac{t}{T_1}\right)\right). \quad (1.118)$$

If the spins are prepared with an excitation $\frac{\pi}{2}$ -pulse then the initial condition is $(M_0, 0)$ and the solution becomes

$$\mathbf{M} = M_0 \exp\left(-\frac{t}{T_2}\right) \exp(-i \mathbf{k} \cdot \mathbf{r}_0) \exp(-i \mathbf{K}_1 \cdot \mathbf{v}_0) \quad (1.119)$$

$$M_z = M_0 \left(1 - \exp\left(-\frac{t}{T_1}\right)\right). \quad (1.120)$$

This gives the magnetization at position \mathbf{r}_0 with velocity \mathbf{v}_0 . The total transverse magnetization is

$$\mathbf{M}_T = \iint \mathbf{M}(\mathbf{r}_0, \mathbf{v}_0) d^3 \mathbf{r}_0 d^3 \mathbf{v}_0. \quad (1.121)$$

Ignoring relaxation

$$M_T(\mathbf{k}, \mathbf{K}_1) = \iint M_0(\mathbf{r}_0, \mathbf{v}_0) \exp(-i \mathbf{k} \cdot \mathbf{r}_0) \exp(-i \mathbf{K}_1 \cdot \mathbf{v}_0) d^3 \mathbf{r}_0 d^3 \mathbf{v}_0. \quad (1.122)$$

Equation (1.122) shows that $M_T(\mathbf{k}, \mathbf{K}_1)$ is the fourier transform of $M_0(\mathbf{r}_0, \mathbf{v}_0)$. This fourier relation is the basis for fourier velocity encoding techniques, which we discuss in (§ 1.4.5). This relation, along with an assumption about $M_0(\mathbf{r}_0, \mathbf{v}_0)$, is also the basis of phase encoding methods, which we discuss in (§ 1.4.4). Flow measurement methods based on (1.122) are known as phase sensitive methods, since the velocity enters as a phase.

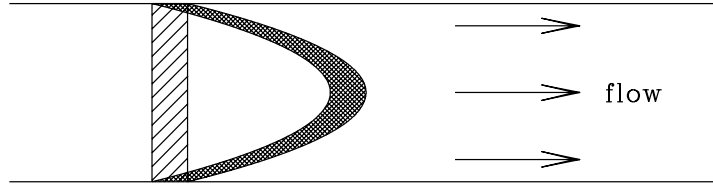


Figure 1.13: Diagram showing the time-of-flight flow measurement technique. We excite spins in a thin slice, shown with stripes. They are allowed to flow to position shown with hash marks, where we measure their positions.

In order to use (1.122) to measure velocity the experimenter must be able to control \mathbf{k} and \mathbf{K}_1 independently through (1.115). In order to show this, it is sufficient to show that there exists a gradient form for which $\mathbf{k} = 0$ and $\mathbf{K}_1 = c$, and one for which $\mathbf{k} = d$ and $\mathbf{K}_1 = 0$, where c and d are non-zero. A bipolar gradient satisfies the former. A bipolar gradient contains a positive lobe and a negative lobe of equal area. An example is a sine wave from 0 to 2π . The latter is satisfied by a velocity compensated gradient. An example of this class of gradient waveforms is given by

$$\Gamma(t) = \begin{cases} -\Gamma_0 & 0 < t \leq \tau \\ 2\Gamma_0 & \tau < t \leq 2\tau \\ -\Gamma_0 & 2\tau < t \leq 3\tau \\ 0 & \text{otherwise} \end{cases} .$$

1.4.3 Time-of-Flight

Time-of-flight (Singer, 1980) covers several flow measurement methods which are not based on (1.122). Instead, all of these methods are based on measuring the position of spins which were excited in one place but have moved with the flow to a new location. Consider a straight pipe with water flowing through it, as depicted in figure 1.13. If the excitation process is fast compared to

the flow, then the spins in a thin slice may be excited using a slice selective excitation. Then, after waiting a time, τ , the spins position is measured using any of the techniques described above, for example SE. The measurement of the position of the spins after time, τ , using SE is accomplished through multiple measurement of single lines in k-space. As a result, the flow must be stationary over the time required to complete the measurement, or the flow must be time-periodic. If the flow is periodic, then it can be sampled at the same phase during each period or sampled at twice the frequency. In the latter case, the flow can be time resolved within the period. The spins must also not move too far during the acquisition of a single line of data. For an acquisition time, at , and a desired spacial resolution, Δx , the velocity should satisfy

$$v \ll \frac{\Delta x}{at}.$$

Other variants of this technique include selectively exciting a pattern in the fluid, such as a grid, and then deducing the motion from the deformation of the pattern (Axel & Dougherty, 1989).

This method can be coupled with a fast imaging technique like EPI or spiral to produce two-dimensional images at several frames per second. The weakness of this method is twofold. First, flow velocities must be large to be resolved. In general, it is difficult to determine the distance traveled if it is less than the spacial resolution of the image. Second, this method does not utilize the inherent sensitivity that NMR has to flow through (1.122).

1.4.4 Phase Contrast

Phase contrast methods were developed by O'Donnell (1985) and Dumoulin (1986). These methods use the fact that the phase of the fourier transform of

the signal in (1.122) is dependent on the velocity of the spins. If we fourier transform (1.122) with respect to \mathbf{k} we obtain

$$M_T(\mathbf{r}_0, \mathbf{K}_1) = \int M_0(\mathbf{r}_0, \mathbf{v}_0) \exp(-i \mathbf{K}_1 \cdot \mathbf{v}_0) d^3 \mathbf{v}_0. \quad (1.123)$$

If we assume that

$$M_0(\mathbf{r}_0, \mathbf{v}_0) \simeq M_0(\mathbf{r}_0) \delta(\mathbf{v}_0 - \mathbf{v}(\mathbf{r}_0)), \quad (1.124)$$

where $\delta(\mathbf{v}_0 - \mathbf{v}(\mathbf{r}_0))$ is the Dirac delta function, then (1.123) becomes

$$M_T(\mathbf{r}_0, \mathbf{K}_1) = M_0(\mathbf{r}_0) \exp(-i \mathbf{K}_1 \cdot \mathbf{v}(\mathbf{r}_0)). \quad (1.125)$$

This equation shows that under the assumption (1.124) that the velocity does not vary significantly over a voxel, then the phase image of the fourier transform of the signal given in (1.122) is

$$-i \mathbf{K}_1 \cdot \mathbf{v}(\mathbf{r}_0), \quad (1.126)$$

and $\mathbf{v}(\mathbf{r}_0)$ can be determined from it. Equation (1.125) is the basis of all phase contrast methods. Care must be taken in choosing \mathbf{K}_1 . If it is too large, then the phase will wrap around for larger velocities. To avoid this, $i \mathbf{K}_1 \cdot \mathbf{v}(\mathbf{r}_0)$ must be less than or equal to π . From this we can also derive the gradient strength needed, in a typical situation, to measure a flow with maximum velocity, \mathbf{v}_{\max} . To do this we must assume a certain gradient form. The form used is shown in figure 1.14. This function is given by

$$\mathbf{\Gamma}(t) = \begin{cases} -2\pi\gamma\mathbf{G} \sin(\frac{\pi t}{\tau}) & 0 < t \leq \tau \\ 2\pi\gamma\mathbf{G} \sin(\frac{\pi t}{\tau}) & T < t \leq T + \tau \\ 0 & \text{otherwise} \end{cases} . \quad (1.127)$$

At $t = T + \tau$, from (1.79) $\mathbf{k} = 0$, and from (1.115)

$$\mathbf{K}_1 = 4\gamma\mathbf{G}T\tau. \quad (1.128)$$

Combining the phase wrap limit on (1.126) and (1.128), and solving for $|\mathbf{G}|$ we obtain

$$|\mathbf{G}| = \frac{\pi}{4\gamma T\tau} \frac{1}{|\mathbf{v}_{\max}| \cos \theta}, \quad (1.129)$$

where θ is the angle between the gradient and the flow direction. For typical values of $\tau = 5$ ms, $T = 25$ ms, and γ for protons at 2 T

$$|\mathbf{G}| = \frac{1.47 \text{ G s}^{-1}}{|\mathbf{v}_{\max}| \cos \theta}. \quad (1.130)$$

To determine the velocity resolution of this technique we must include the signal to noise ratio, SNR, in the calculation. The SNR determines the number of values of the phase that can be distinguished. This number is approximately equal to the SNR. For $\text{SNR} = 10$ a gradient of 14.7 G cm^{-1} would be needed to achieve a resolution of $100 \mu\text{m s}^{-1}$, which is easily attained at our facility. However, this is still well beyond what the average MRI facility can achieve, with gradients typically around 1 G cm^{-1} .

While this technique is good at measuring slow and fast flows, the dynamic range is limited by the SNR. It is also able to measure velocity in all three directions. As with time of flight techniques, the flow field must be either stationary or periodic. In practice, phase images are very sensitive to inhomogeneities in the static field, the gradients, and the rf field. As a result, the background phase must be removed before this technique can be used successfully. The major drawback to this technique with respect to its application in porous media is the assumption made in (1.124). As the pore scale gets smaller the distribution of velocities get wider over a constant sized voxel. In the next section we will discuss a technique which will overcome this problem by actually measuring this distribution on a voxel by voxel basis. It also makes

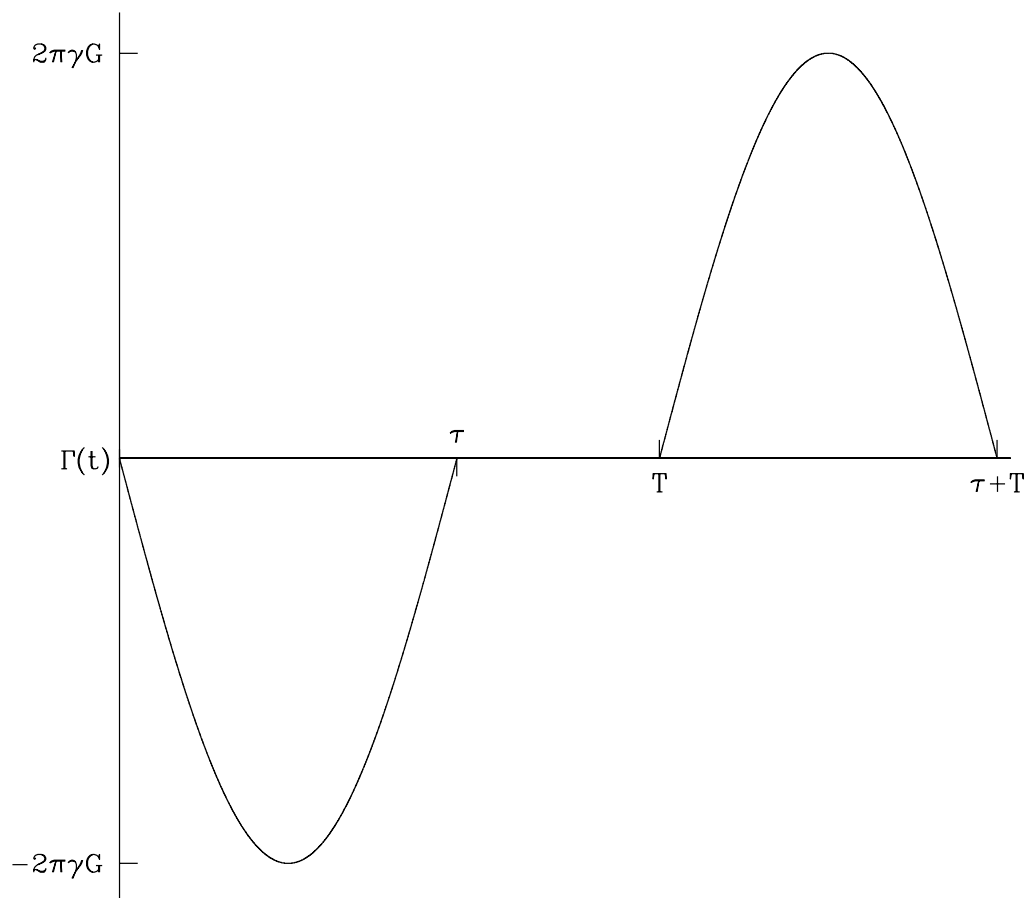


Figure 1.14: Typical gradient form used in phase sensitive velocity measurements. Each lobe is a half period sine function.

the resolution nearly independent of the SNR.

1.4.5 Fourier Velocity Encoding

Introduction

Fourier velocity encoding was developed theoretically by Moran (1982), and verified experimentally by Redpath, Norris, Jones & Hutchison (1984). This method is based on (1.122), which shows that $M_T(\mathbf{k}, \mathbf{K}_1)$ is the fourier transform of $M_0(\mathbf{r}_0, \mathbf{v}_0)$. This fourier relation between \mathbf{K}_1 and \mathbf{v}_0 is the same as the relation between \mathbf{k} and \mathbf{r} used to measure spacial distribution as described in (§1.3.2). Thus, everything described earlier may be applied to the measurement of velocity. K-space is now six-dimensional and can be measured in the same way that the original three-dimension k-space is measured. This method can also be extended to measure higher derivatives of the motion. Equation (1.114) was truncated arbitrarily a $\mathcal{O}(t^2)$. If terms up to the N -th derivative are included the total transverse magnetization becomes

$$M_T(\mathbf{K}_0, \mathbf{K}_1, \dots, \mathbf{K}_N) = \int \dots \int M_0(\mathbf{R}_0, \mathbf{R}_1, \dots, \mathbf{R}_N) \prod_{n=0}^N \exp(-i \mathbf{K}_n \cdot \mathbf{R}_n) d^3 \mathbf{R}_n. \quad (1.131)$$

Equation (1.131) shows that in principle the distribution of N derivatives of the motion could be measured on an $3N$ -dimensional grid. The obvious problem is time. We calculate the time required to sample an N -dimensional k-space with the number of points, N_i , for the i^{th} dimension. We assume that only one dimension is acquired during each repetition period, T_r . Of course, in reality

more than one dimension can be sampled using EPI, spiral, or FSE.

$$\text{Total Acquisition Time} = T_r N_a \prod_{i=2}^N N_i, \quad (1.132)$$

where N_a is the number of averages per line acquired. For $T_r = 125$ ms, $N = 6$, $N_i = 32$, and $N_a = 2$, then the acquisition time is 97 days. So, although it is theoretically possible to get six-dimensional information, with current equipment $N = 4$ is probably the limit for high resolution experiments. However, $N = 6$ can be considered where lower resolution is acceptable.

In order to maintain high spacial and velocity resolution several of the six-dimensions must be eliminated. First, one spacial dimension can be eliminated by selective excitation. With a slice selective excitation of thickness, Δz in the \hat{z} direction (1.122) becomes

$$\begin{aligned} M_T(k_x, k_y, \mathbf{K}_1) = \\ \int \iint \overline{M_0(x, y, \mathbf{v})} \exp(-i(k_x x + k_y y)) \exp(-i \mathbf{K}_1 \cdot \mathbf{v}) dx dy d^3 \mathbf{v}, \end{aligned} \quad (1.133)$$

where

$$\overline{M_0(x, y, \mathbf{v})} = \int_{-\frac{\Delta z}{2}}^{\frac{\Delta z}{2}} M_0(\mathbf{r}, \mathbf{v}) dz. \quad (1.134)$$

Second, only one velocity direction is measured at a time. For concreteness we choose the \hat{z} direction and therefore $\mathbf{K}_1 = K_{1z} \widehat{K}_{1z}$. This results in

$$\begin{aligned} M_T(k_x, k_y, K_{1z}) = \\ \iiint \overline{M_0(x, y, v_z)} \exp(-i(k_x x + k_y y + K_{1z} v_z)) dx dy dv_z, \end{aligned} \quad (1.135)$$

where

$$\overline{M_0(x, y, v_z)} = \iint \int_{-\frac{\Delta z}{2}}^{\frac{\Delta z}{2}} M_0(\mathbf{r}, \mathbf{v}) dz dv_x dv_y, \quad (1.136)$$

$\overline{M_0(x, y, v_z)}$ is calculated from the fourier transform of the signal (1.135) using the following formula:

$$\overline{M_0(x_0, y_0, v_{z0})} = \frac{1}{(2\pi)^3} \iiint \mathbf{M}_T(\mathbf{k}_x, \mathbf{k}_y, K_{1z}) \times \exp(-i(\mathbf{k}_x x_0 + \mathbf{k}_y y_0 + K_{1z} v_{z0})) d\mathbf{k}_x d\mathbf{k}_y, dK_{1z}. \quad (1.137)$$

$\overline{M_0(x_0, y_0, v_{z0})}$ is proportional to the average density of spins with position (x_0, y_0) and velocity v_{z0} , where average is defined by (1.136). Measurement of this function gives the distribution of velocities at each point in a thin slice.

We derive several important quantities from (1.136). First, the average value of the velocity at each point,

$$v_z(x, y) = \frac{\int \overline{M_0(x, y, v_z)} v_z dv_z}{\int \overline{M_0(x, y, v_z)} dv_z}. \quad (1.138)$$

Second, the relative density of spins at each point,

$$\rho_{\text{rel}}(x, y) = \frac{\int \overline{M_0(x, y, v_z)} dv_z}{\max \left\{ \int \overline{M_0(x, y, v_z)} dv_z \right\}}. \quad (1.139)$$

Third, the width of the distribution at each point can be related to the diffusion coefficient. For a pulse sequence similar to the SE sequence that we describe in (§ 1.4.5), Callaghan (1991) calculates that the diffusion constant,

$$D = \frac{(\pi N_{V_z} W_{\text{FWHM}})^2}{4 \log(2) [\gamma \tau G_{\text{max}} N]^2 T},$$

where N_{V_z} is the number of velocity encoding steps, W_{FWHM} is the full-width-half-maximum of the velocity distribution peak measured in pixels, N is the

number of spacial encoding bins and τ , T and G_{\max} are defined from figure 1.14. Finally, we can determine the temperature field from $\overline{M_0(x, y, v_z)}$, under certain conditions. T_1 for water is a function of temperature. For the temperature range 0–40 °C at 1.4 T the dependence is (Hindman, Svirnickas & Wood, 1971)

$$T_1 = 6531 \exp\left(\frac{-2243.24}{T}\right) \text{ s}, \quad (1.140)$$

where the temperature, T is measured in K. The initial magnetization is a function of T_1 through (1.34) and given by

$$M_0 = i M_0 \left(1 - \exp\left(\frac{-T_r}{T_1(x, y)}\right)\right). \quad (1.141)$$

If $T_r \gg T_1$, then (1.139) measures the density, since

$$\exp\left(\frac{-T_r}{T_1(x, y)}\right) \simeq 0.$$

If $T_r \leq T_1$, then (1.139) measures the density weighted by

$$\left(1 - \exp\left(\frac{-T_r}{T_1(x, y)}\right)\right).$$

The temperature field is determined from the density, the T_1 weighted density, and (1.140). We have not implemented this procedure to obtain actual quantitative temperature maps, but the T_1 weighted density images provide some temperature information.

We discuss the specific pulse sequences which we use to measure $\overline{M_0(x, y, v_z)}$ in the following sections.

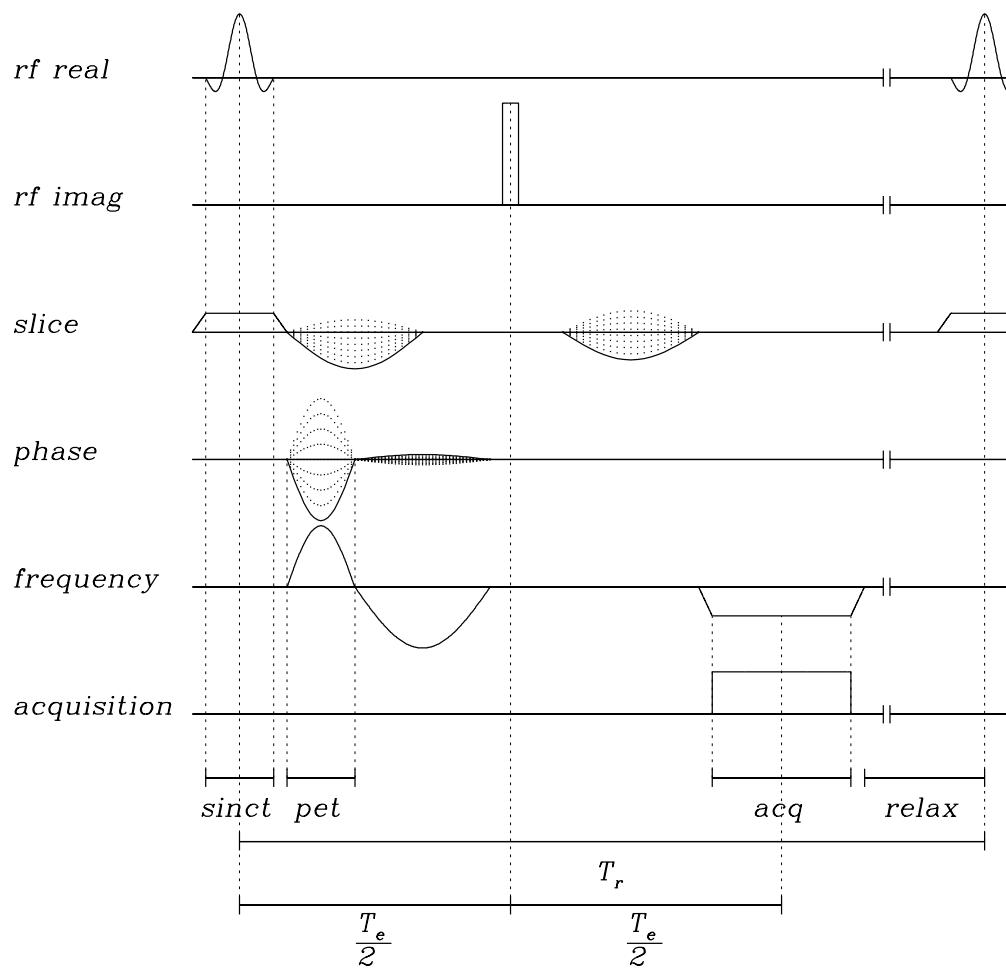


Figure 1.15: Velocity encoding SE pulse sequence.

Spin Echo Pulse Sequence

Measuring $\overline{M_0(x, y, v_z)}$ is similar to measuring $M_0(\mathbf{r})$. Compare the pulse sequence shown in figure 1.15 to figure 1.9. The first difference is the addition of a second synchronous incrementing gradient on the slice line. We chose the magnitude of the incrementing gradients such that by the beginning of the acquisition $k_{\text{slice}} = 0$ and

$$K_{1\text{slice}} = \frac{n\pi}{2\max\{|v_{\text{slice}}|\}},$$

where n is incremented from $-\frac{1}{2}(N_{V_{\text{slice}}} - 1)$ to $\frac{1}{2}(N_{V_{\text{slice}}} - 1)$ and $\max\{|v_{\text{slice}}|\}$ is the absolute value of the maximum velocity in the slice direction. The slice gradient, $k_{\text{slice}}(t)$, and $K_{1\text{slice}}(t)$ are shown in figure 1.16. The vertical dashed line indicates the position of the π -pulse, which inverts the sign of both $k_{\text{slice}}(t)$ and $K_{1\text{slice}}(t)$. In accordance with (1.101) only half of the slice selection gradient contributes to $k_{\text{slice}}(t)$ and $K_{1\text{slice}}(t)$.

We determine the gradient magnitudes shown in figure 1.16 as follows. G_s is determined by the thickness of the slice through (1.105). G_1 and G_2 are determined by the requirements above on k_{slice} and $K_{1\text{slice}}$ as follows:

$$G_1 = \frac{12K_{1\text{slice}} - \pi\gamma G_s [\tau_r(6T + 3\tau + 4\tau_r) + 3\tau_s(4T + 2\tau + 4\tau_r + \tau_s)]}{48\gamma T\tau};$$

$$G_2 = \frac{12K_{1\text{slice}} - \pi\gamma G_s [\tau_r(3\tau + 4\tau_r) + 3\tau_s(2\tau + 4\tau_r + \tau_s)]}{48\gamma T\tau}.$$

Note that we recover the relation in (1.128), if $G_s = 0$. The durations of the various parts of the slice pulse are arbitrary. They are usually chosen so that they are as small as possible given the constraint imposed by the maximum value of the gradient strength. This slice gradient is incremented as the outer part of a nested loop with the phase gradient.

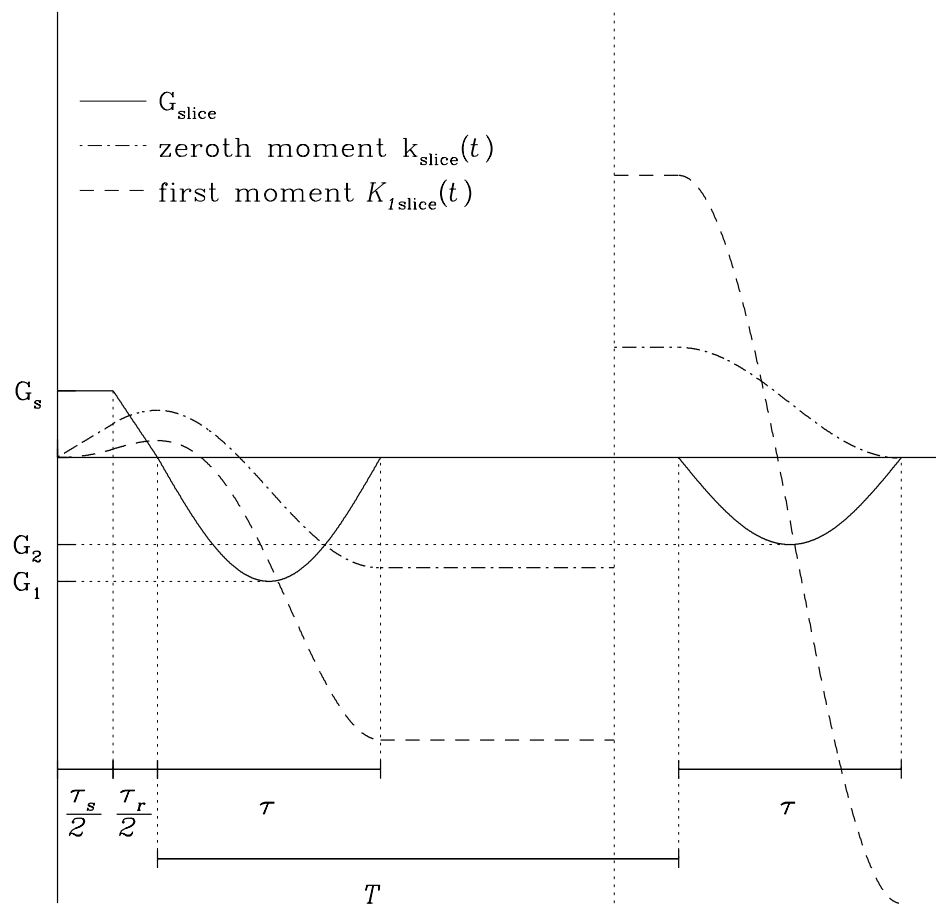


Figure 1.16: Graph of the slice gradient and its zeroth and first moments.

The second difference between figure 1.15 and figure 1.9 is the addition of a gradient lobe on the frequency line. This gradient is included so that $K_{1\text{frequency}} = 0$ at the center of the acquisition and k-space. It is not possible to produce a gradient which has $K_{1\text{frequency}} = 0$ throughout k-space, as is strictly required by the derivation in the previous section. By making $K_{1\text{frequency}} = 0$ at the center of k-space we come as close as possible to the ideal. An extra gradient is not really needed in the phase direction since $K_{1\text{phase}}$ is already zero when $k_{\text{phase}} = 0$, however, we have included one to make $K_{1\text{phase}} = 0$ throughout k-space.

The total time to measure $\overline{M_0(x, y, v_z)}$ using this sequence is:

$$\text{Total Acquisition Time} = N_a N_y N_{v_z} T_r. \quad (1.142)$$

For a typical scan with resolution $(256 \times 256 \times 16)$, $T_r = .5$ s, and two averages, the total scan time is 68 min. We have used two techniques to shorten this time. If the fluid is doped with copper sulfate or manganese chloride the relaxation times will be shortened. If T_1 is shorter then a shorter T_r can be used with no loss of signal. A copper sulfate concentration of 1×10^{-3} M gives a $T_1 = 100$ ms. Using this concentration a T_r of 100 ms gives a good signal and shortens the total acquisition time by a factor of 5 or allows the acquisition of a $(256 \times 256 \times 64)$ matrix in approximately the same time. This method is appropriate for simple flow experiments, for which a pure fluid is not needed. However, for convective experiments the system is changed significantly by the presence of temperature-induced concentration gradients. We give the second method that we use to shorten the acquisition time in the next section.

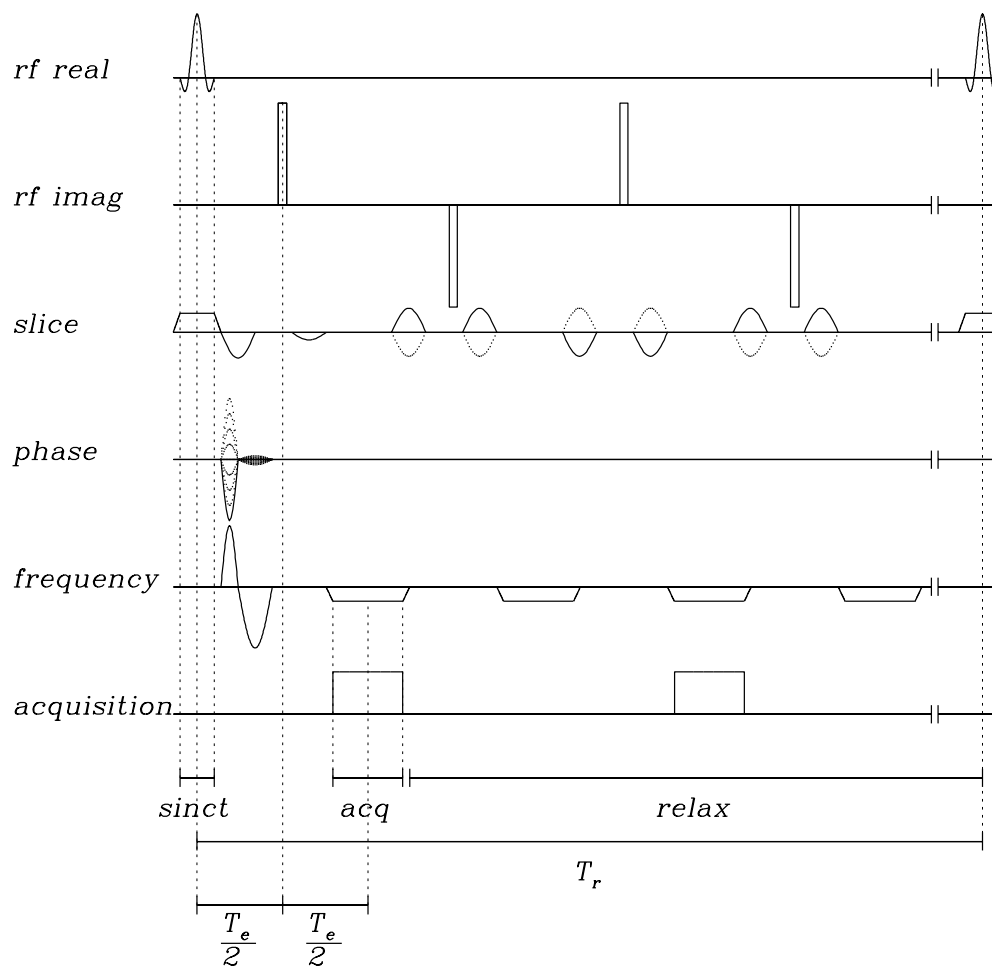


Figure 1.17: Velocity encoding FSE pulse sequence.

Fast Spin Echo Pulse Sequence

We explained the general three-dimensional FSE technique in (§ 1.3.5). The application of FSE to fourier velocity encoding is very similar to the general technique. We show the pulse sequence that we use in figure 1.17. After a slice selective excitation, the gradients on the phase and frequency lines move \mathbf{k} to the edge of k-space in both remaining spacial dimensions. The gradients on the slice line produce a slice selective excitation and move $K_{1\text{slice}}$ to zero. Thus, during the first echo we acquire one line of k-space with $K_{1\text{slice}} = 0$ and

$$k_{\text{phase}} = \frac{N_{\text{phase}}\pi}{\text{fovpe}},$$

where fovpe is the field of view in the phase direction and N_{phase} is the number of points to be determined in the phase direction. With the application of the second π -pulse the position of \mathbf{k} and $K_{1\text{slice}}$ reflects about the origin. However, $K_{1\text{slice}}$ is unchanged, since it is initially zero. Then, before the second echo, $K_{1\text{slice}}$ is changed such that

$$K_{1\text{slice}} = \frac{1}{2} \frac{\pi}{\text{fov v}},$$

where fovv is the total range of velocities. In our implementation, we ignore this echo and all even echoes. The application of a third π -pulse reflects the position of \mathbf{k} and $K_{1\text{slice}}$ about the origin. At this point,

$$K_{1\text{slice}} = -\frac{1}{2} \frac{\pi}{\text{fov v}},$$

and we increment $K_{1\text{slice}}$ again by the same amount but in the opposite direction. Now,

$$K_{1\text{slice}} = -\frac{\pi}{\text{fov v}},$$

and we acquire the second line of k-space from the third echo. Proceeding in the same way we acquire a new line of k-space during each echo. In one echo train we acquire one half of one of the $k_{\text{frequency}} - K_{1\text{slice}}$ plane. During the next echo train we acquire the second half using gradients of opposite sign. With this scheme we acquire the $K_{1\text{slice}} = 0$ line during both acquisitions and average them. Finally, we change the phase gradient, and we acquire another $k_{\text{frequency}} - K_{1\text{slice}}$ plane.

In the previous discussion, the timing of the motion in the $k_{\text{frequency}} - K_{1\text{slice}}$ plane is imprecise. Actually, we break the gradients, which change $K_{1\text{slice}}$, into two parts across the π -pulse instead of applying them in sequence, as implied above. Therefore, the simple motion described above between each echo is not correct, but the final result at the time of the echo is correct.

The total time to measure $\overline{M_0(x, y, v_z)}$ using this sequence is:

$$\text{Total Acquisition Time} = 2N_a N_{\text{phase}} T_r. \quad (1.143)$$

For our typical scan using this sequence with resolution $(256 \times 256 \times 16)$, $T_r = 2$ s, and two averages, the total scan time is 34 min. However, comparison of (1.143) and (1.142) shows we can achieve much shorter acquisitions using the FSE sequence compared to the SE sequence. In general, this FSE sequence is $N_{\text{velocity}}/2$ time faster than the SE sequence.

In theory, it is possible to speed up acquisition by another factor of two, by using both the odd and even echoes. In a SE sequence, the phase variations are functions of the real-space variables only. Because of this, they are thrown away, since we retain only the magnitude (1.86). The problem with FSE is that the phase of the odd and even echoes is not the same in practice. This leads to phase variations which are functions of both the k-space variables and

real-space variables. Such phase variations cannot be corrected for in general. We could also retain both odd and even echoes from the sequence above. This would give a full reconstruction from each set, which could be averaged to increase the SNR. We choose not to do this, since it requires twice the storage space, more than twice the processing time, and we already have adequate SNR.

The FSE technique has two advantages over the SE technique. First, it is much faster. Second, the multiple π -pulses limit the effects of diffusion.

Chapter 2

Verification of Velocity Measurements with MRI

2.1 Introduction

In order to test the velocity encoding MRI techniques discussed in (§ 1.4.5), we examined two systems for which the flow pattern is known by theory and experiment. The first is pressure driven flow in a long straight pipe, whose flow field is known to be parabolic (Landau & Lifshitz, 1987). For a cylindrical pipe with flow in the \hat{z} direction the flow field is

$$\mathbf{v}_{\text{pipe}}(\mathbf{r}) = \left[v_{\text{max}} \left(1 - \frac{\mathbf{r} \cdot \mathbf{r} - (\mathbf{r} \cdot \hat{z})^2}{R_0^2} \right) \right] \hat{z},$$

where R_0 is the radius of the pipe and v_{max} is the maximum velocity at the center of the tube. The second system is an axially rotating cylinder of fluid. After a short transient, the fluid moves in solid body rotation, for which the velocity field is given by,

$$\mathbf{v}_{\text{cyl}}(\mathbf{r}) = \boldsymbol{\Omega}_0 \times \mathbf{r},$$

where $\boldsymbol{\Omega}_0$ is the angular velocity.

In the first case the acceleration, which is the substantive derivative of the

velocity, is zero, that is,

$$\left(\frac{\partial}{\partial t} + \mathbf{v} \cdot \nabla\right) \mathbf{v}_{\text{pipe}}(\mathbf{r}) = 0.$$

In this case, the truncation made in the derivation of (1.122) is exact. For the rotating cylinder the acceleration is

$$\left(\frac{\partial}{\partial t} + \mathbf{v} \cdot \nabla\right) \mathbf{v}_{\text{cyl}}(\mathbf{r}) = \boldsymbol{\Omega}_0 \times (\boldsymbol{\Omega}_0 \times \mathbf{r}).$$

In this case the acceleration increases linearly along the radius, and we test the effect of acceleration on the measurement process.

2.2 Bulk Flow in a Pipe

We examine two pipe flow systems. In the first case we use the SE velocity encoding scheme, discussed in (§ 1.4.5), to measure the velocity in a 3.175 cm pipe. The flow is maintained by a constant pressure source that is described in (§ 3.4). We measured the average flow rate using a graduated cylinder and a stop watch. Combining the flow rate with the diameter of the tube we determine the theoretical velocity profile. A plot of the flow profile is shown in figure 2.1. To check the curve against theory we plot the velocity as a function of radius, in figure 2.2. We average the data over the azimuthal angle. In this figure, we measure every parameter; there are no fitted constants. The data shows excellent agreement with the theory.

One of the strengths of the velocity encoding technique is the ability to determine the velocity distribution. In figure 2.3 we show the measured and the theoretical distributions. The agreement is very good.

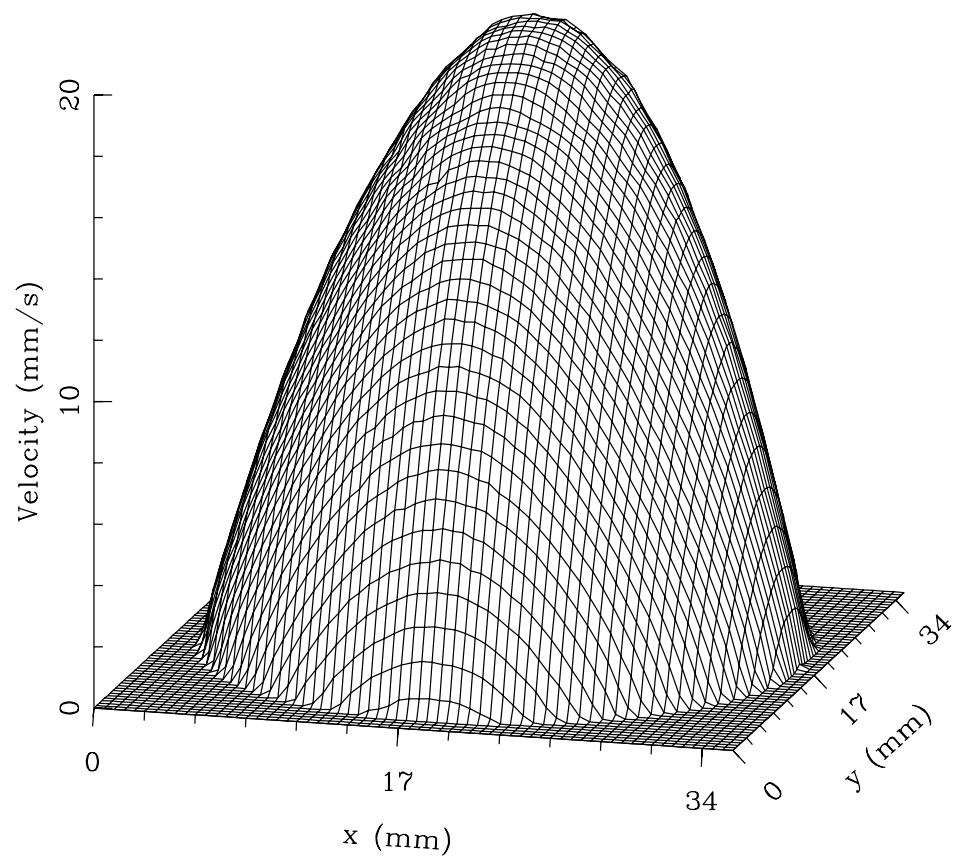


Figure 2.1: Three-dimensional plot of the velocity along a 3.175 cm pipe. The velocity is averaged over a 2 mm thick slice. The in-plane resolution is $140 \mu\text{m}$. The velocity resolution is 0.6 mm s^{-1} .

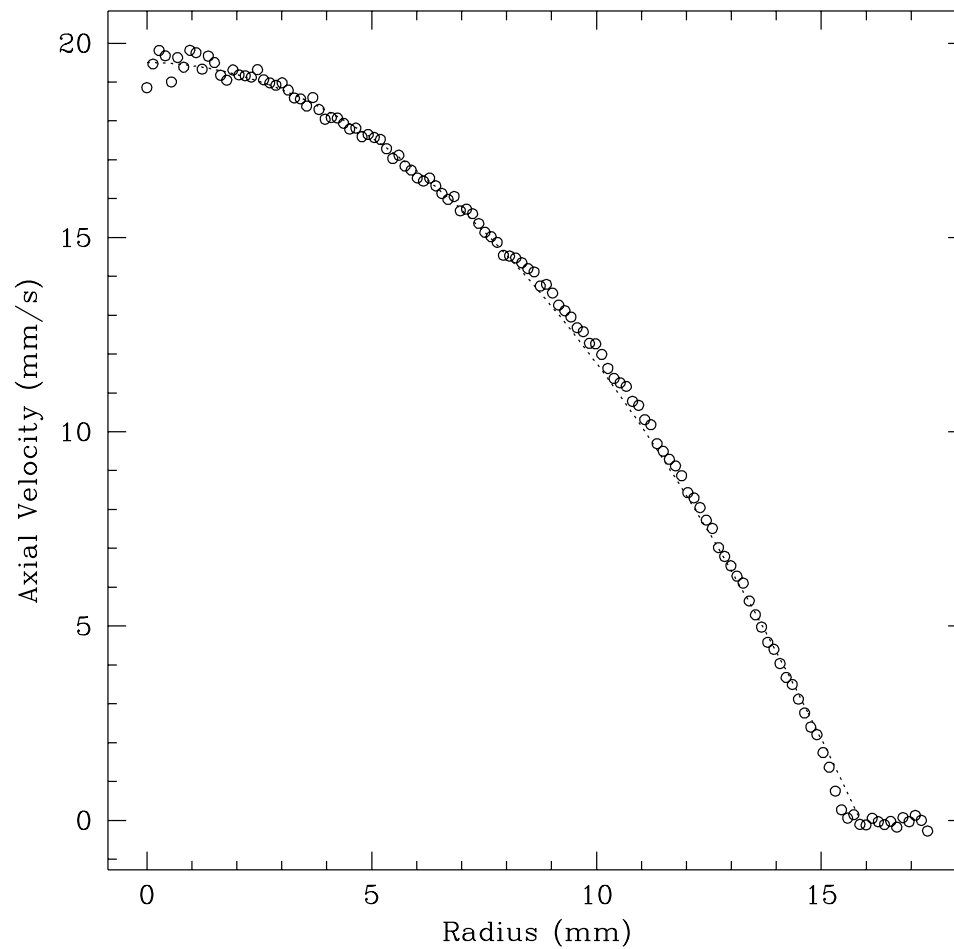


Figure 2.2: Two-dimensional graph of the azimuthally averaged velocity along a 3.175 cm pipe. The velocity is averaged over a 2 mm thick slice and over the azimuthal angle. The resolution is $140 \mu\text{m}$. The velocity resolution is 0.6 mm s^{-1} . We show the theoretical velocity profile as a dotted line. The theoretical curve is based on the flow rate and the diameter of the tube. There are no fitted parameters.

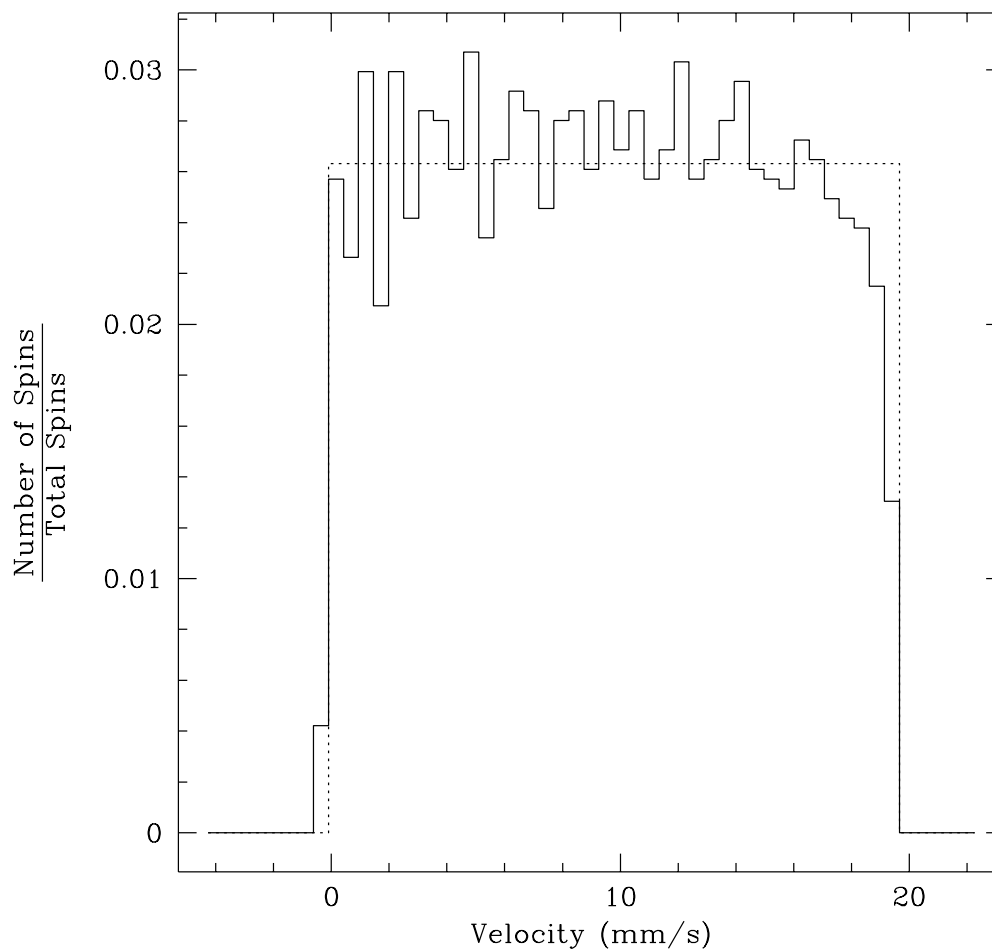


Figure 2.3: Graph of the distribution of velocity as a function of velocity for parabolic flow along a 3.175 cm pipe. The velocity is averaged over the entire 2 mm thick slice, in all directions. The velocity resolution is 0.6 mm s^{-1} . We show the theoretical velocity distribution as a dotted line. The theoretical curve is based on the flow rate and the diameter of the tube. There are no fitted parameters.

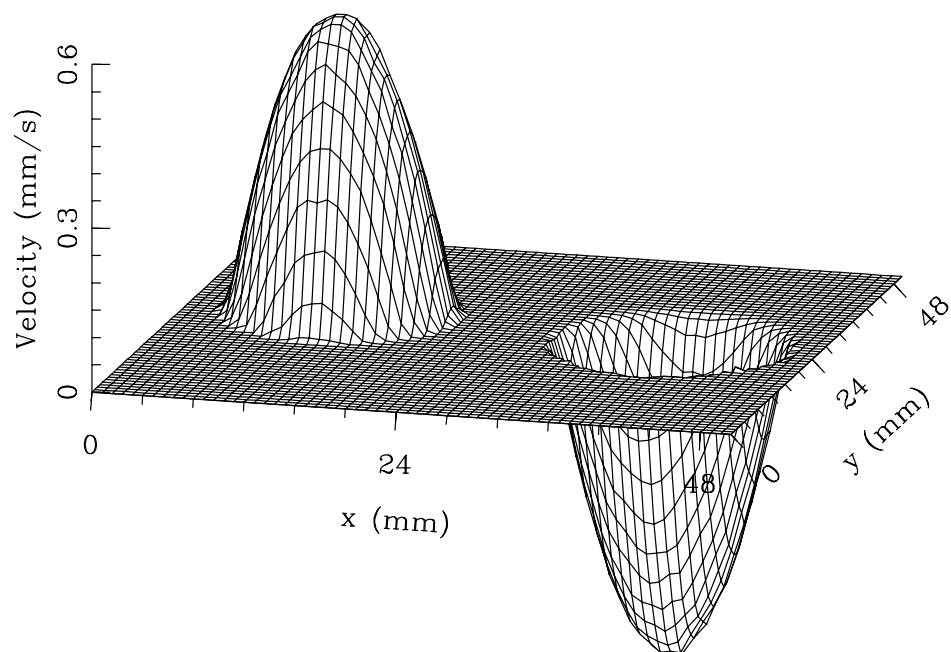


Figure 2.4: Three-dimensional plot of the velocity along the twin 1.765 cm pipes. The velocity is averaged over a 1 mm thick slice. The in-plane resolution is $195 \mu\text{m}$. The velocity resolution is $40 \mu\text{m s}^{-1}$. This maximum velocity is $520 \mu\text{m s}^{-1}$

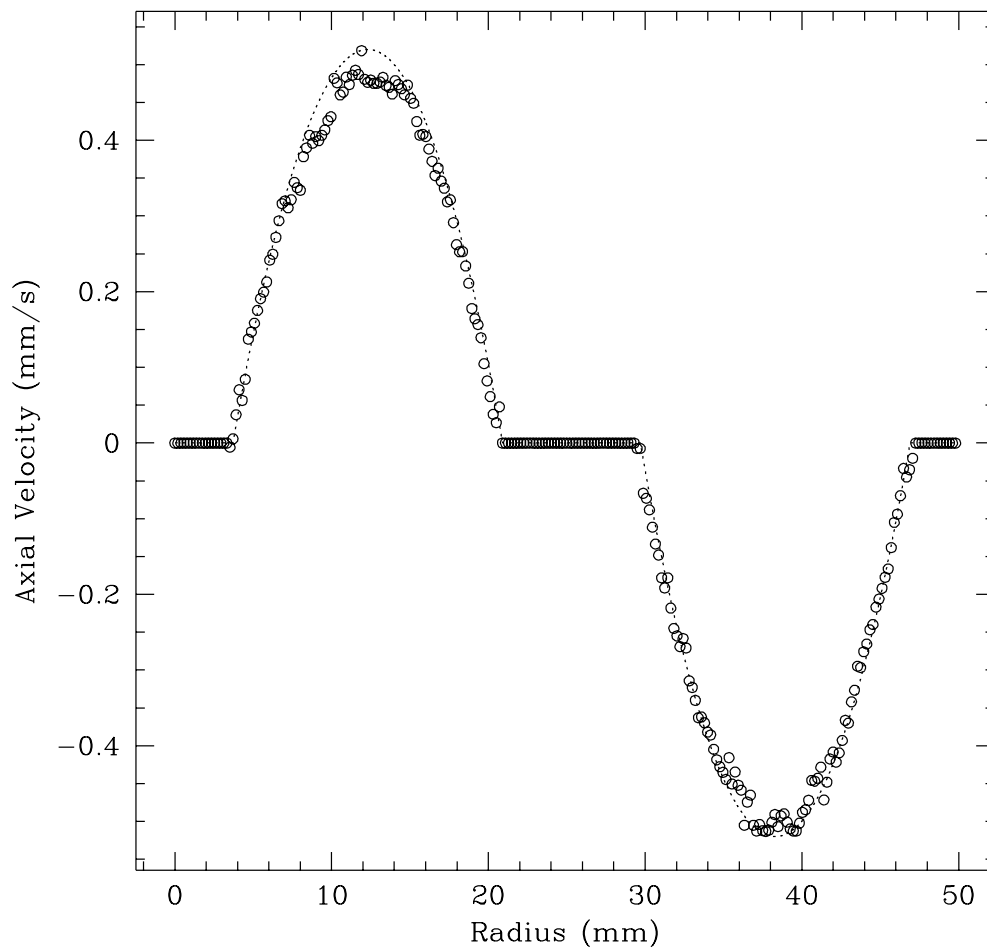


Figure 2.5: Two-dimensional graph of a line going through the centers of both pipes. The velocity is averaged over a 1 mm thick slice. The spatial resolution is $195 \mu\text{m}$. The velocity resolution is $40 \mu\text{m s}^{-1}$. We show the theoretical velocity profile, with a maximum velocity of $520 \mu\text{m s}^{-1}$, as a dotted line. The theoretical curve is based on the flow rate and the diameter of the tube. There are no fitted parameters.

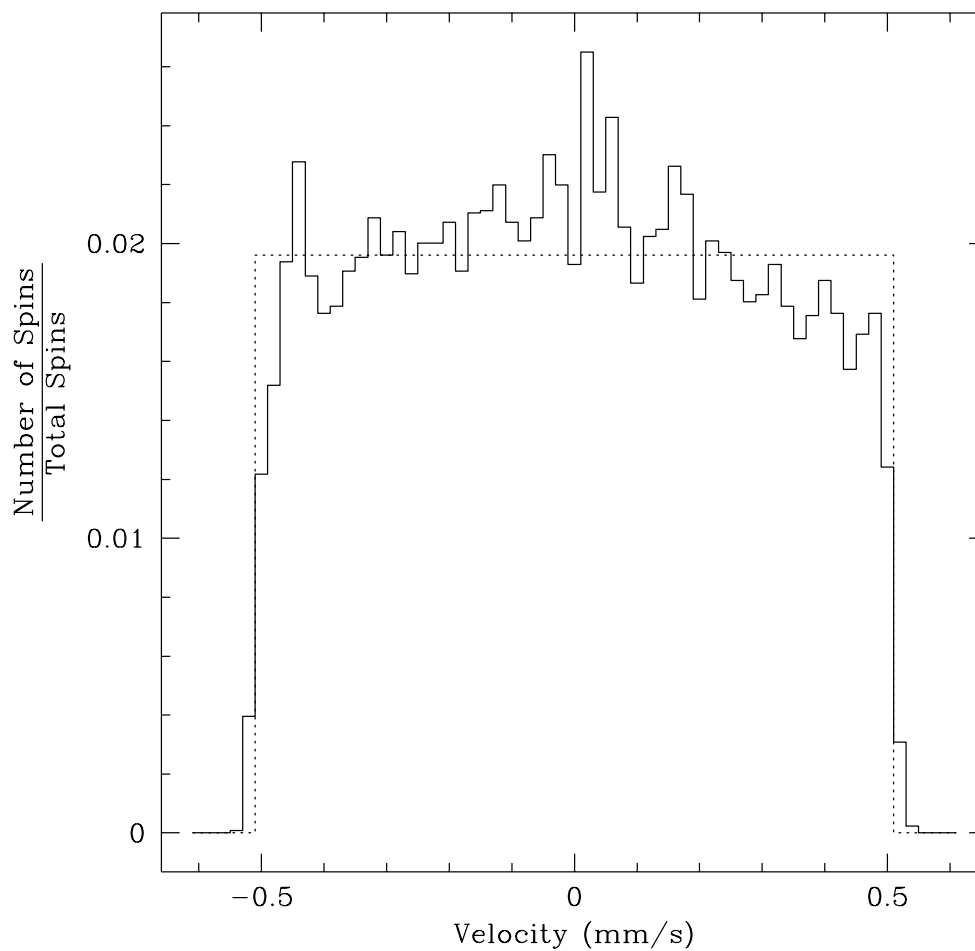


Figure 2.6: Graph of the distribution of velocity as a function of velocity for parabolic flow through both pipes. The velocity is averaged over the entire 1 mm thick slice, in all directions. The velocity resolution is $40 \mu\text{m s}^{-1}$. We show the theoretical velocity distribution as a dotted line. The theoretical curve is based on the flow rate and the diameters of the tubes. There are no fitted parameters.

We have also examined another pipe flow system using the FSE velocity encoding scheme discussed in (§1.4.5). In this case, we place two long pipes with inner diameters of 1.765 cm side by side. At one end they are connected together, and at the other end we use one as the inlet and one as the outlet. This allows us to monitor and correct for another variable: the net flow rate. Since we are imaging both the inflow and the outflow, the net flow rate must be zero. Without any adjustments the net flow rate is $3.2 \times 10^{-3} \text{ cm}^3 \text{ s}^{-1}$ which is 2.7% of the flow rate through one of the pipes. In this case no correction is needed. We show the flow profile in figure 2.4, and the velocity along a line through the center of both pipes in figure 2.5. In figure 2.6 we show the distribution of velocities in both pipes. As above, there are no fitted parameters in either of these figures.

2.3 Rotating Cylinder

We examined an axially rotating cylinder using the SE velocity encoding sequence developed in (§1.4.5). We use a programmable stepper motor to turn a long rod connected to the cylinder. In this experiment, we demonstrate that we can measure in-plane velocities as well as the velocity perpendicular to the slice.

In figure 2.7 we display an image of the spins in four different velocity bins. The ringing artifact is a result of improper filtering in k-space. In these images, we measure the velocity in the vertical direction. All of the fluid with the same value of vertical velocity is in a vertical line. For example, all of the fluid that is not moving in the upward direction lies on a vertical line in the center of the cylinder. This is the correct result from the velocity field

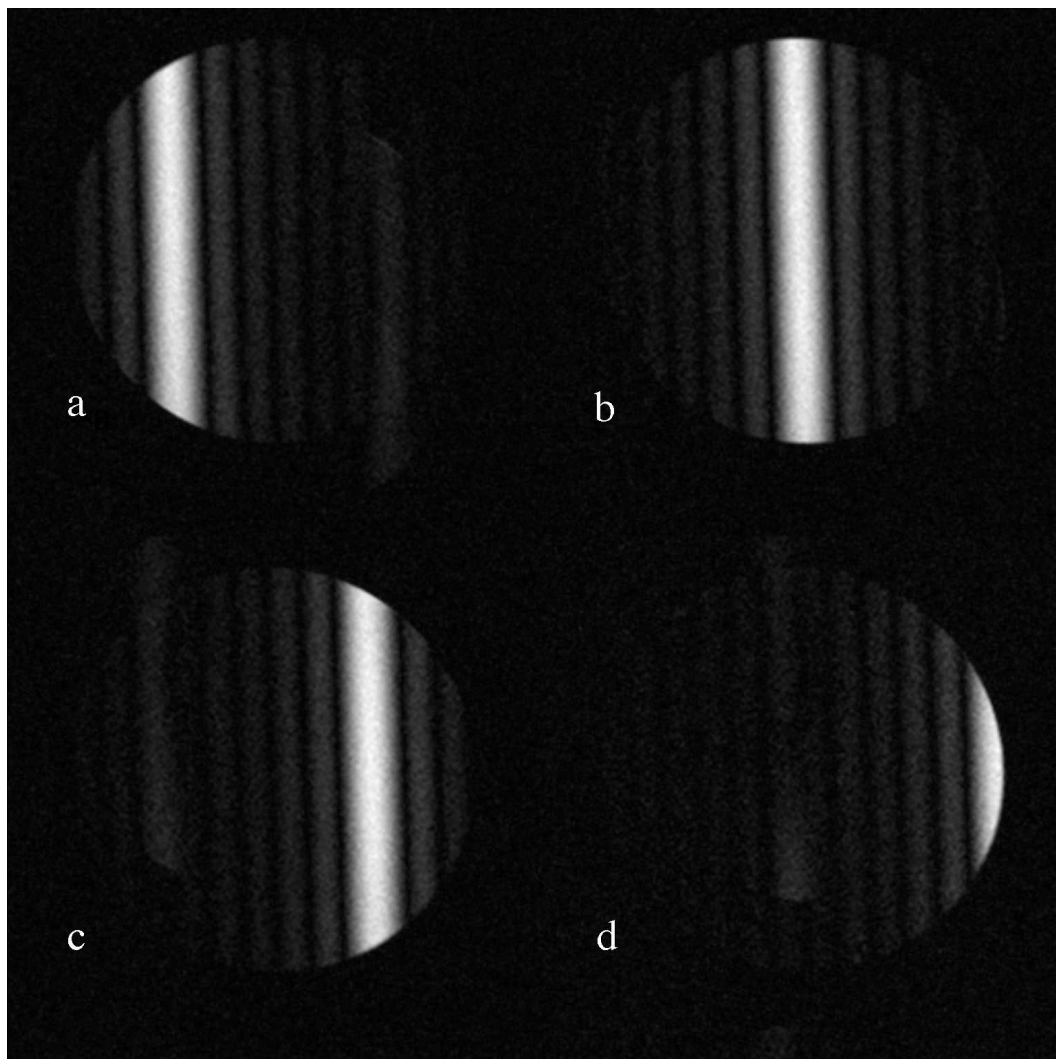


Figure 2.7: Velocity bins for a rotating cylinder. The rotation rate is one revolution per second. The diameter of the cylinder is 3.175 cm. Each image shows a different velocity bin. The ringing artifact is caused by improper k-space filtering. Images of spins in the rotating disk which have velocity a) -8.8 cm s^{-1} , b) 0 cm s^{-1} , c) 8.8 cm s^{-1} , and d) 17.6 cm s^{-1}

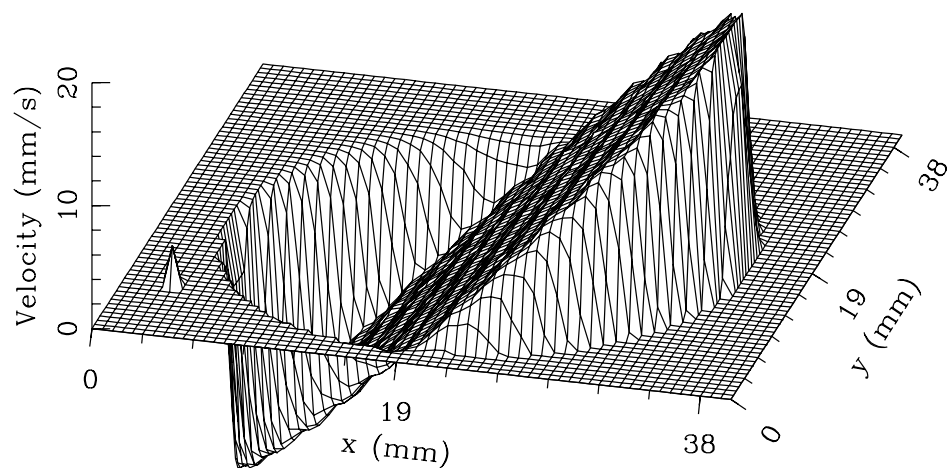


Figure 2.8: Three-dimensional graph of the vertical, in-plane velocity in the rotating cylinder. The velocity is averaged over a 2 mm thick slice, and the velocity resolution is 2.94 cm s^{-1} . The rotation rate is one revolution per second, and the diameter of the cylinder is 3.175 cm.

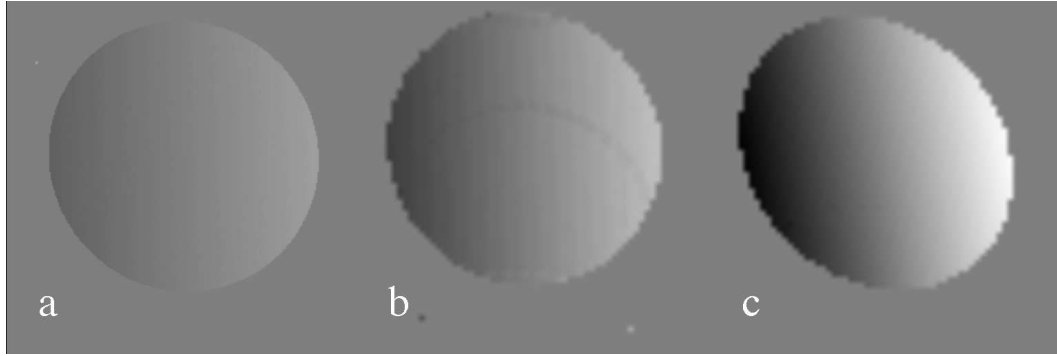


Figure 2.9: Grayscale images of the vertical velocity in the rotating disk at rotation rate of a) $2\pi \text{ rad s}^{-1}$, b) $4\pi \text{ rad s}^{-1}$, and c) $8\pi \text{ rad s}^{-1}$. The intensity of grey is proportional to the velocity. As the rate increases, the images become somewhat distorted.

above. In figure 2.8 we show a three-dimensional plot of the average velocity field. As the rotation rate is increased the image begins to distort. Figure 2.9 shows grayscale images of the vertical velocity in the cylinder at three rotations rates: $2\pi \text{ rad s}^{-1}$, $4\pi \text{ rad s}^{-1}$, and $8\pi \text{ rad s}^{-1}$. At the lowest rotation rate the velocity at the edge of the 3.175 cm tube is 19.9 cm s^{-1} , and the acceleration is 125 cm s^{-2} . This is much larger than the accelerations that we expect to find in the porous media convection, and it is equal our largest flow rates in the pipe flow experiment. To get an order of magnitude estimate, we calculate the acceleration of a fluid particle moving around the surface of a δ diameter bead at velocity, v . The acceleration is

$$a = \frac{2v^2}{\delta} = \frac{2\nu^2}{c_F^2 K \delta} Re^2 = 22 \text{ cm s}^{-2} Re^2,$$

where we have used the definition of the Reynolds' number from (§ 4.3.2), and the values of various parameters from table 4.1. Here, ν is the kinematic viscosity, c_F is a constant equal to approximately 0.55, K is the permeability of the medium, and Re is the Reynolds' number, which is a non-dimensional measure of the velocity. In the pipe flow experiments we have looked at flows

with $Re \simeq 1$. In the convection experiments $Re \leq 0.12$. We measure the percent difference between the major and minor axis from figure 2.9 and find that the magnitude of the distortion for $2\pi \text{ rad s}^{-1}$ is 1.5%, for $4\pi \text{ rad s}^{-1}$ is 10%, and for $8\pi \text{ rad s}^{-1}$ is 31%. For many experiments, this distortion is probably acceptable. Further, in theory it could be corrected by using gradient pulses which have the coefficient of the acceleration term in (1.114) set to zero.

2.4 Conclusions

From the previous sections we see that MRI is an excellent tool for measuring flow non-invasively. The technique is quantitative, and gives good accuracy without any adjustable parameters. Both the SE and FSE technique show good agreement with the test flows. The FSE technique allows measurement of very slow flows. In this section, we achieve a resolution of $40 \mu\text{m s}^{-1}$. In the convection experiments, we typically achieve $20 \mu\text{m s}^{-1}$. There can be spacial distortion associated with the presence of acceleration. This is a problem when the acceleration is of the same order as

$$\frac{2\nu^2}{c_F^2 K \delta} Re^2.$$

Part II

Porous Media Flows

Introduction

Porous media flows are a part of many problems of significant technical importance, including ground water filtration, oil and gas recovery, extraction of geothermal energy, heat transport in insulation and packed beds, as well as many other industrial processes (Combernous & Bories, 1975). These applications are often complicated by multi-phase, multi-component fluids and intricate geometries. The study of simpler related systems or model systems often aids in the understanding of such complicated systems.

We consider here two important model systems. In chapter 3 we describe pressure-driven flow through a packed bed of beads. In this experiment a constant pressure head forces pure water through a porous medium of mono-disperse plastic beads. We chose this system as a first test of our new MRI technique since it is one of the simplest experiments in porous media flows. Although extensively studied, very little was known about the flow field inside the media because of the lack of visualization techniques. We are able to compare our results with other measurements taken just outside of a porous medium, and with theory which predicts flow channelling near the walls. We also use MRI to look at the porosity of our sample.

In chapter 4 we discuss buoyancy-driven convection in a packed bed of beads. In this experiment a thin horizontal layer of beads with isothermal boundaries on top and bottom and fully saturated with pure water is heated

from below. This is the principal experiment of this work. It is both technically relevant and amenable to theoretical description. It is also interesting as a nonlinear pattern forming system. Previous experiments in this area are typically invasive and therefore difficult to connect with theory. As a result a large body of theory exists for which there is very little experimental confirmation or contradiction (Torrance et al., 1982; Georgiadis, 1991). With this work and future work using this technique we begin to correct this deficiency.

Chapter 3

Pressure-Driven Flows

3.1 Introduction

Single-phase pressure-driven flow in fully-saturated porous media is of considerable importance to a variety of environmental applications, chemical engineering processes, and biological systems; for example, oil and gas recovery, aquifers, filtration, catalytic beds, and serum flow in living tissue. The idealized system consists of a uniform porous media fully-saturated with a single phase pure fluid which moves under the influence of an external pressure gradient. Such a system is characterized entirely by a small number of parameters. In addition to fluid parameters such as the viscosity, the flow may depend on the void fraction, or porosity, the permeability, the pore volume to pore surface ratio, and many other properties defined over the years. Ideally, these properties could be determined for certain classes of porous media once, and then applied to many situations. Unfortunately, these properties can differ even among various realizations of the same system. For example, the porosity of a packed bed of spheres can vary from 0.48, for cubic packing, to .26, for close packing. Haughey & Beveridge (1953) compiled a list of observed porosities for randomly packed mono-disperse spheres. They determined four categories:

gently settled, loose random, poured random, and close random, which had porosities that varied from 0.36 – 0.44. Clearly this variations affects other properties, such as the permeability, which depend on the third power of the porosity in (3.9) and (3.10). These variations can also occur within the media. At the boundaries of packing of spheres, for example, the porosity must increase to one since the spheres can only touch at a point. Added to the problem that the major parameters must be determined on a case by case basis, is the experimental problem that it is very difficult to measure the velocity inside a porous medium. Because of these difficulties, there is not a clear consensus on the equations of motion or the dependence of various parameters on each other. There are at least two equations, (3.9) and (3.11), for this system which correlate well with existing data (Nield & Bejan, 1992). Both equations have the same dependence on velocity, namely a linear term and a quadratic term, but no consistent definition of the coefficient dependence on the material parameters will reduce them to the same equation.

In this work, we measure the interstitial velocity distributions in a packed bed of mono-disperse spheres. This is one of first non-invasive quantitative velocity measurements in this system. The experiments of Northrup, Kulp & Angel (1991), who also measured the velocity in this system using particle tracking, will be discuss in cd(§3.2). The MRI technique also gives the local porosity. The spacial resolution of the velocity and porosity measurements is 40 – 140 μm , and the velocity resolution is 0.3% of the maximum velocity. The technique yields not only the average velocity but also the distribution of velocities at each point in a plane on a 256×256 grid. The thickness of the plane can be varied from 0.5 mm to 2 mm. We have used this method to verify for the first time flow channelling inside a porous medium, which had been

theoretically predicted but only measured near the outlet of a porous media, or with such low resolution that it was inconclusive. We also verify the average radial porosity which has been previously measured (Benenati & Brosilow, 1962; Cheng, Chowdhury & Hsu, 1991), and report the average porosity along the flow direction. In fact, with our three-dimensional density data we can determine the porosity distribution along any direction averaged over an arbitrary volume. We also investigate the assumptions of the continuum equations used to describe porous media flow by looking at the porosity as a function of the size of the averaging volume.

3.2 Previous Experiments

The modern study of flows in porous media began with Henri Darcy (Darcy, 1856). His study of pressure-driven flow through a porous media uncovered an empirical relation between pressure and flow rate that provides the basis for the equations of motion in porous media used today. There have been many studies of pressure drop as a function of flow rate. In a review by Macdonald, El-Sayed, Mow & Dullien (1979) eight different data sets (Fancher & Lewis, 1933; Doering, 1955; Matthies, 1955; Dudgeon, 1966; Kyan, Wasan & Kintner, 1970; Luther, Abel, Rittner, Giesler & Schultz, 1971; Rumpf & Gupte, 1971; Pahl, 1975) were tested against the Ergun equation (Ergun, 1952) and what is referred to as the Ahmed-Sunada equation (Ahmed & Sunada, 1969). Both equations fit the data well and will be discussed in detail in (§ 3.3). Several researchers have used hot wire anemometry (Morales, Spinn & Smith, 1951; Schwartz & Smith, 1953; Szekely & Poveromo, 1975) and laser anemometry (Volkov, Reznikov, Khalilov, Zel'vensky & Sakodynsky, 1986) to study the

flow profiles at the outlet of the porous medium. These experiments showed a radial velocity profile with a maximum near the wall, a phenomenon called flow channelling. Volkov et al. also includes velocity distributions for several sphere diameters. They indicate that the longitudinal velocity is asymmetric and has long tails. From their graphs it appears that they do not have enough data to determine the functional dependence of the histograms. Chu & Ng (1989) have also investigated flow channelling as it affects the measurement of permeability. They find that for system-to-particle diameter ratios below 10 the permeability is overestimated as compared to the bulk. When the ratio is decreased to 2.5 the permeability will be overestimated by a factor of 2.5. They also use a computer simulation to determine the distribution of pore velocities. Stephenson & Stewart (1986) measured the interstitial velocity in a quartz tube filled with quartz cylinders. They used a fluid which has the same index of refraction as quartz, and placed the entire apparatus in a box filled with the fluid to avoid the refraction due to the cylindrical surface of the tube. They determined the velocity field in a plane parallel to the flow direction using small air bubbles. They recorded the flow on tape and then transferred it to film. They projected each frame onto a sheet of paper, on which they recorded the bubble position manually. From the positions they determined the velocity. While their data showed radial flow rate enhancement near the walls, the actual velocity decreased. They also show velocity distributions which are somewhat different than the ones we show in figure 3.11. One is much more symmetric, and the other is bimodal. Northrup et al. (1991) have also used particle tracking in index-matched fluid to obtain the velocity field in a system of 3 mm spheres in a 5.2 cm tube. Their work was concurrent with our study, and they obtained substantially similar results. However, even

with automated data, taking their measurements lack sufficient numbers to determine the velocity distribution with great accuracy. For comparison, the maximum number of points in their velocity bins is 50. In figure 3.11 each of the 64 bins include 65536 individual measurements.

3.3 Theory

3.3.1 Introduction

A porous medium consists of a solid matrix with holes or pores. For fluid flow only the subset of interconnected pores are relevant. If a pore is not connected to the outside of the matrix then it does not affect isothermal flow in any way. However, such pores can affect heat transport which in turn can affect the flow. In this section we concentrate on a simple system in which the only dynamic variables are the velocity and pressure. The temperature is assumed isothermal in all space. We also assume that a pure single-phase fluid fully saturates the solid matrix. For bulk fluids the velocity and pressure are related by the Navier-Stokes equations. These equations also apply in the case of porous media, but due to the complicated boundary conditions are extremely difficult to solve. The same situation exists for bulk fluid flows when the individual molecule's motion is considered. In that case the equation of motion is Newton's equation.

3.3.2 Representative Elementary Volume

Both of these problems are solved in the same way. In bulk fluids, we do not attempt to determine the trajectory of each molecule. Instead we consider a volume of fluid which is large compared to the molecular mean free path and

small compared to the system. The equations which govern the flow of this fluid volume are much simpler. The determination of the macroscopic equations from the microscopic ones is an averaging process. This averaging can be either spacial or statistical. In the case of spacial averaging the fluid volume, over which the averaging takes place, is called a representative elementary volume, or r.e.v. For porous media we must find an r.e.v., V_{rev} , which is large compared to the pore size, δ , and small compared to the system, L , that is, $\delta \ll V_{\text{rev}} \ll L$. We then define all macroscopic or continuum properties in terms of averages of microscopic properties over the r.e.v. Two different types of volumes can be defined (Nield & Bejan, 1992). One is based on an r.e.v., V_m , which contains the medium as a whole, both fluid and solid. The other is based on an r.e.v., V_f , which contains only fluid. Variables can be averaged over either one depending on the situation. In general, unless otherwise noted, variables based on V_f are subscripted with an f and variables based on V_m are subscripted with an m .

3.3.3 Conservation of Mass

The seepage velocity, \mathbf{v} , is based on averages over V_m , while the intrinsic velocity \mathbf{V} is based on averages over V_f . The relation between them is

$$\mathbf{v} = \frac{V_f}{V_m} \mathbf{V} = \phi \mathbf{V},$$

where the void fraction, ϕ , is called the porosity. The mass conservation law is derived by equating the time rate of change of an arbitrary volume to the flux of fluid into a volume. This gives,

$$\frac{d}{dt} \int \rho_m dV = - \int \rho_f \mathbf{v} \cdot d\mathbf{S}, \quad (3.1)$$

where ρ_f is the density of the fluid and $\rho_m = \phi\rho_f + (1-\phi)\rho_s$ is the density of the medium, and ρ_s is the density of the solid. Using Gauss's law and exchanging the order of differentiation and integration on the left hand side of (3.1) we obtain

$$\int (\phi \frac{\partial \rho_f}{\partial t} + \nabla \cdot (\rho_f \mathbf{v})) dV = 0, \quad (3.2)$$

where we have used the fact that $\frac{\partial \phi}{\partial t} = 0$ and $\frac{\partial \rho_s}{\partial t} = 0$. In order for this integral to be zero for all t the integrand must be zero. Thus,

$$\phi \frac{\partial \rho_f}{\partial t} + \nabla \cdot (\rho_f \mathbf{v}) = 0. \quad (3.3)$$

3.3.4 Boundary Conditions

One consequence of the averaging process is seen in the boundary conditions appropriate for the continuum equations in porous media. In bulk fluids, the correct boundary condition is called no slip, and is given by,

$$\mathbf{v}(\mathbf{r})|_{\mathbf{r}=\boldsymbol{\sigma}} = 0,$$

where $\boldsymbol{\sigma}$ is an impenetrable stationary surface. Since each r.e.v., even those adjacent to an impenetrable surface, contains many pores, the velocity need not go to zero. The correct condition on the velocity is obtained from (3.3). If we assume that the fluid is incompressible then (3.3) becomes,

$$\nabla \cdot \mathbf{v} = 0.$$

For simplicity, we assume that the surface is at $x = 0$ and pointing in the \hat{x} direction toward the outside of the medium. Since the pore size must be small

in order for the continuum approach to be valid we use it as a differential.

Then,

$$\frac{v_x(x + \delta, y, z) - v_x(x, y, z)}{\delta} = -\left(\frac{\partial v_y(x, y, z)}{\partial y} + \frac{\partial v_z(x, y, z)}{\partial z}\right).$$

Outside the boundary the velocity is zero, and we obtain

$$v_x(0, y, z) = \delta\left(\frac{\partial v_y(x, y, z)}{\partial y} + \frac{\partial v_z(x, y, z)}{\partial z}\right).$$

Since by definition δ is small, the condition becomes

$$\hat{n} \cdot \mathbf{v}(\mathbf{r})|_{\mathbf{r}=\boldsymbol{\sigma}} = 0,$$

where \hat{n} is normal to $\boldsymbol{\sigma}$.

3.3.5 Darcy's Law

Henri Darcy, in his study of fountains in Dijon, uncovered an empirical relation between the pressure applied across a uniform porous media and the bulk flow rate through it (Darcy, 1856). This relation can be expressed by Darcy's law,

$$v_z = -\frac{K}{\eta} \frac{\partial P}{\partial z}, \quad (3.4)$$

where v_z is seepage velocity, η is the fluid dynamic viscosity, P is the pressure, and z is the direction of the flow. K is a geometrical property of the porous media which has units of area and is called the permeability. This equation is for one-dimensional flow. The three-dimensional generalization (Nield & Bejan, 1992; Bear, 1988) is

$$\mathbf{v} = \eta^{-1} \mathbf{K} \cdot \nabla P, \quad (3.5)$$

where \mathbf{K} is a second rank tensor. In the case of an isotropic media (3.5) reduces to

$$\nabla P = -\frac{\eta}{\mathbf{K}}\mathbf{v}. \quad (3.6)$$

Equation (3.6) has been confirmed both experimentally and theoretically for small \mathbf{v} . Dullien (1979) discusses theoretical results from a geometrical approach, and Whitaker (Whitaker, 1986) and Ene (Ene & Poliřevski, 1987) use statistical methods to derive (3.6).

While Darcy's law has strong experimental and theoretical backing, extensions to include acceleration terms and large \mathbf{v} have not been settled. With the addition of the acceleration term proposed by Nield & Bejan (1992) (3.6) becomes,

$$\rho_f \mathbf{c}_a \cdot \frac{\partial \mathbf{v}}{\partial t} = -\nabla P - \frac{\eta}{\mathbf{K}}\mathbf{v}, \quad (3.7)$$

where ρ_f is the fluid density and \mathbf{c}_a is the acceleration coefficient tensor. This equation is analogous to the momentum equation for pure fluids. However \mathbf{c}_a is thought to be negligible in most situations (Nield & Bejan, 1992). Several terms have been suggested to explain deviations from (3.6) at large \mathbf{v} . These include a \mathbf{v}^2 dependence suggested by Forchheimer (1901). The Ahmed-Sunada equation (Ahmed & Sunada, 1969),

$$\nabla P = -a\eta\mathbf{v} - b\rho_f|\mathbf{v}|\mathbf{v}, \quad (3.8)$$

where a and b are arbitrary constants to be determined experimentally is one possible version of Forchheimer's idea. Macdonald et al. (1979) compared this equation to an equation of the same form due to Ergun (1952). Ergun

determined the one-dimensional empirical relation,

$$\frac{\partial P}{\partial z} = -\frac{150\eta(1-\phi)^2 v_z}{d_p^2 \phi^3} - \frac{1.75\rho_f(1-\phi)v_z^2}{d_p^2 \phi^3}, \quad (3.9)$$

where ϕ is the void fraction, d_p is the average particle diameter, and the constants, 150 and 1.75 depend on the details of the media. This relation was also derived theoretically by Irmay (1958). By comparing (3.9) and (3.4) an equation for K can be determined. This relation,

$$K = \frac{d_p^2 \phi^3}{150(1-\phi)^2}, \quad (3.10)$$

is known as Kozeny's equation and gives reasonable estimates of K . Another equation based on Forchheimer's idea is due to Ward (Ward, 1964) and is given by

$$\nabla P = -\frac{\eta}{K}\mathbf{v} - c_F K^{-1/2} \rho_f |\mathbf{v}|\mathbf{v}, \quad (3.11)$$

where c_F is a dimensionless form-drag constant. While both (3.9) and (3.11) fit experimental data well, no consistent definition of K will reduce them to the same equation. Obviously with the appropriate choice of constants (3.8) can be transformed into either the Ergun equation or to (3.11) and will fit current experimental data as well.

Brinkman (1901) added a second viscous term which is analogous to the Laplacian term in the Navier-Stokes equation, but with a different viscosity. His equation,

$$\nabla P = -\frac{\eta}{K}\mathbf{v} + \eta_B \nabla^2 \mathbf{v}, \quad (3.12)$$

is appropriate for large values of the porosity.

3.3.6 Flow Channelling

Flow channelling is an enhanced velocity flow near the boundary of a porous medium and an impermeable wall. If the matrix is made of packed spheres, then near the wall the porosity necessarily goes to a limiting value of one. In fact, our measurements as well as others (Benenati & Brosilow, 1962, for example) have shown that the porosity is an oscillating function which starts at the wall at one and decays to the mean porosity in about five bead diameters in randomly packed spheres. Therefore from (3.10) the permeability will increase, and as a result the velocity will increase as well. Due to the no slip boundary conditions, at the impermeable wall the velocity will go to zero. From this we see that within the distance of one pore diameter the velocity will increase to a maximum and then decrease to zero at the wall.

3.4 Experimental Setup

The schematic of the test section is given in figure 3.1. It consists of a random packing of mono-disperse spherical acrylic beads of $3.204 \pm .029$ mm diameter. The beads are fully saturated with water in a plastic cylindrical tube with inner diameter of 3.175 cm and held in place by two perforated plugs. The water also contains copper sulfate in order to expedite the acquisition of data. The whole assembly is placed inside the bore of the MRI magnet, which is represented by the outer cylinder in figure 3.1. The water is forced through the plastic tube in the \hat{z} direction by a constant pressure head system. A schematic of this system is shown in figure 3.2.

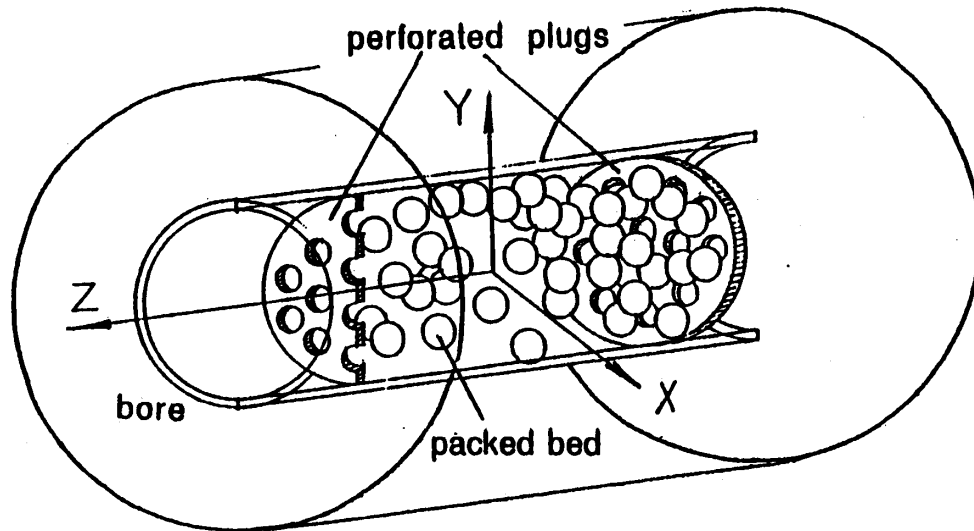


Figure 3.1: Schematic showing the test section used in the MRI pressure-driven flows experiments. The section consists of $3.204 \pm .029$ mm diameter mono-disperse spherical acrylic beads randomly packed in a 3.175 cm inner diameter tube. The beads are held in two perforated plugs.

3.5 Results

The image shown in figure 3.3 was obtained by a standard 3-D imaging sequence in the absence of flow. In this image we measure the relative density of spins at each point on a $(256 \times 256 \times 256)$ grid. The image corresponds to the cylindrical container depicted in figure 3.1 and described above. This image is a volumetric rendering of the density of water in the sample. The intensity of the grey tone corresponds to the density at a given spatial location. The density is known at each $2.5 \times 10^{-3} \text{cm}^3$ voxel. This type of data can be used to obtain the porosity of selected slices and volumes, which in the past has been obtained only by physically slicing and weighing the media (Benenati & Brosilow, 1962).

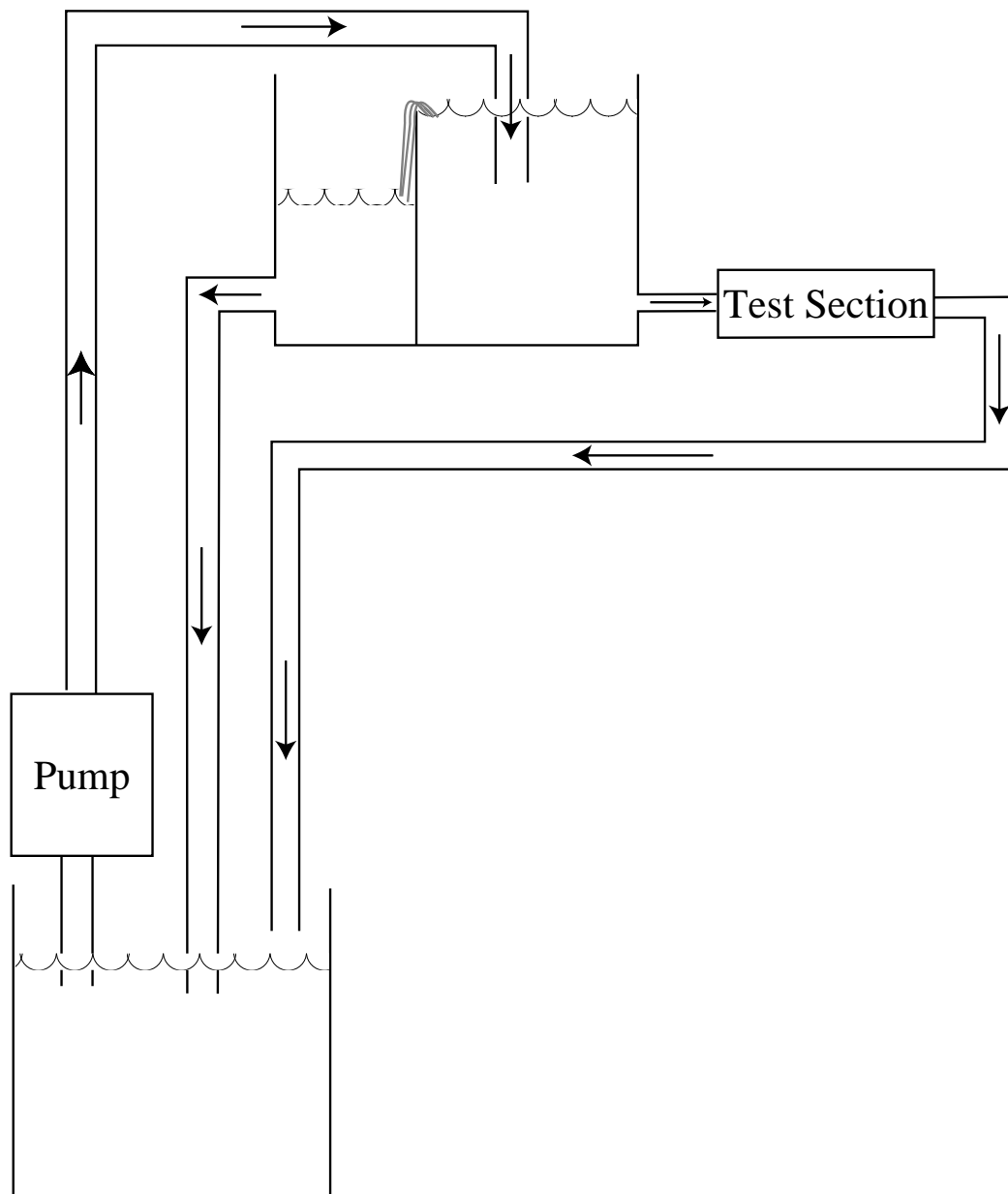


Figure 3.2: Schematic showing constant pressure head system connected to the test section.

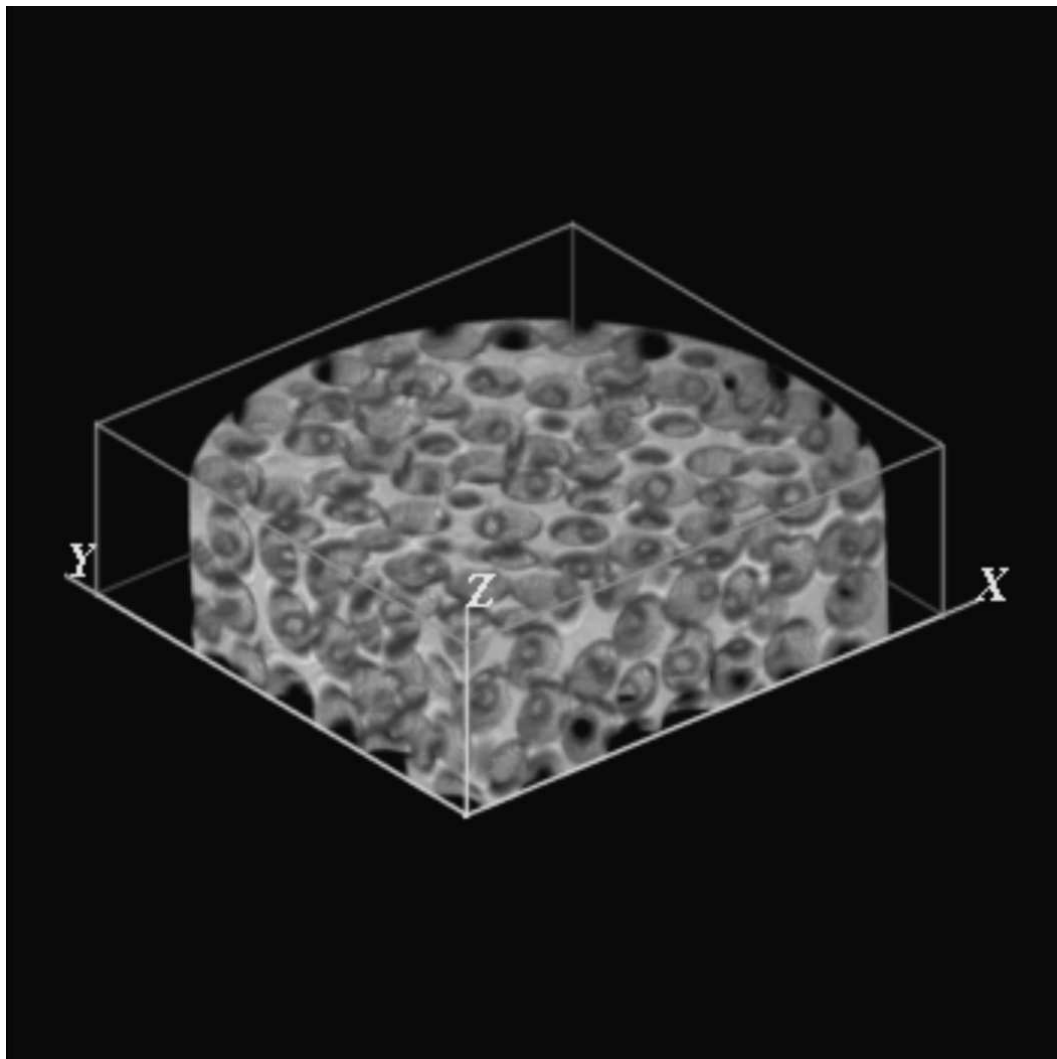


Figure 3.3: Volumetric rendering of the interstitial space (filled with water) in a packed bed using Magnetic Resonance Imaging. The section consists of $3.204 \pm .029$ mm diameter mono-disperse spherical acrylic beads randomly packed in a 3.175 cm inner diameter tube. The intensity of the grey scale corresponds to the density of water at that point. This is a small section from a $256 \times 256 \times 256$ isotropic array. The spacial resolution is 0.14 mm.

3.5.1 Long Range Order

We present four different averages in figure 3.4-3.7. Each of these plots shows the long range order present in this media, which is nominally random. In figure 3.4 we see average porosity seen by a fluid particle approaching the medium. There is a great deal of order. This is more easily seen in figure 3.6 where we also average azimuthally. For comparison, figure 3.5 shows the azimuthal average without the \hat{z} average. This shows that some of the order comes from each average. Finally, figure 3.7 shows the oscillatory nature of the porosity as a function of z . These observations have been previously noted by other authors (Benenati & Brosilow, 1962; Cheng et al., 1991).

3.5.2 Spacial Averaging of Porosity

We determined the porosity as a function of r.e.v. size. We expect that for small volumes, the value will be either zero or one, that is, in a bead or outside a bead. For larger volumes the value should vary widely but slowly approach the value of the bulk. Then as it increases further it will vary again as it begins to include large scale spacial variations. We choose 27 random positions in the central region of the porous medium shown in figure 3.3. All points were more than one quarter of the diameter from a wall or the edge of the data set. At each location we calculate the porosity using a volume, V_{rev} , ranging from one voxel to half the size of the tube diameter. The result is plotted against the log of the cube root of V_{rev} in units of bead diameters in figure 3.8. From this graph we see that an average porosity is reached at all points in about 3 bead diameters.

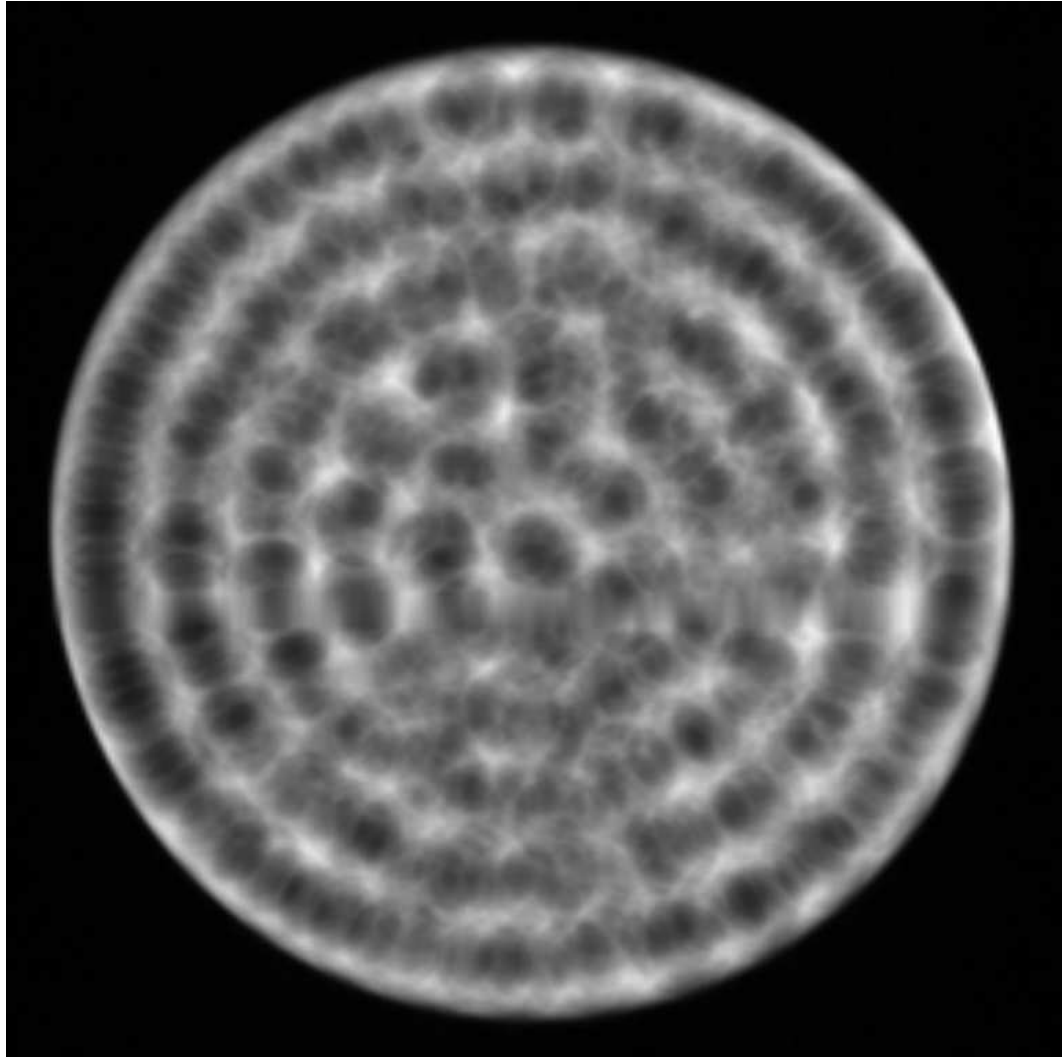


Figure 3.4: Image of porosity averaged over the \hat{z} axis, parallel to the tube. The image is averaged over 35 mm or 11 bead diameters from a $256 \times 256 \times 256$ isotropic array. The pixels are 0.14 mm across. The grey values are scaled to the maximum intensity pixel.

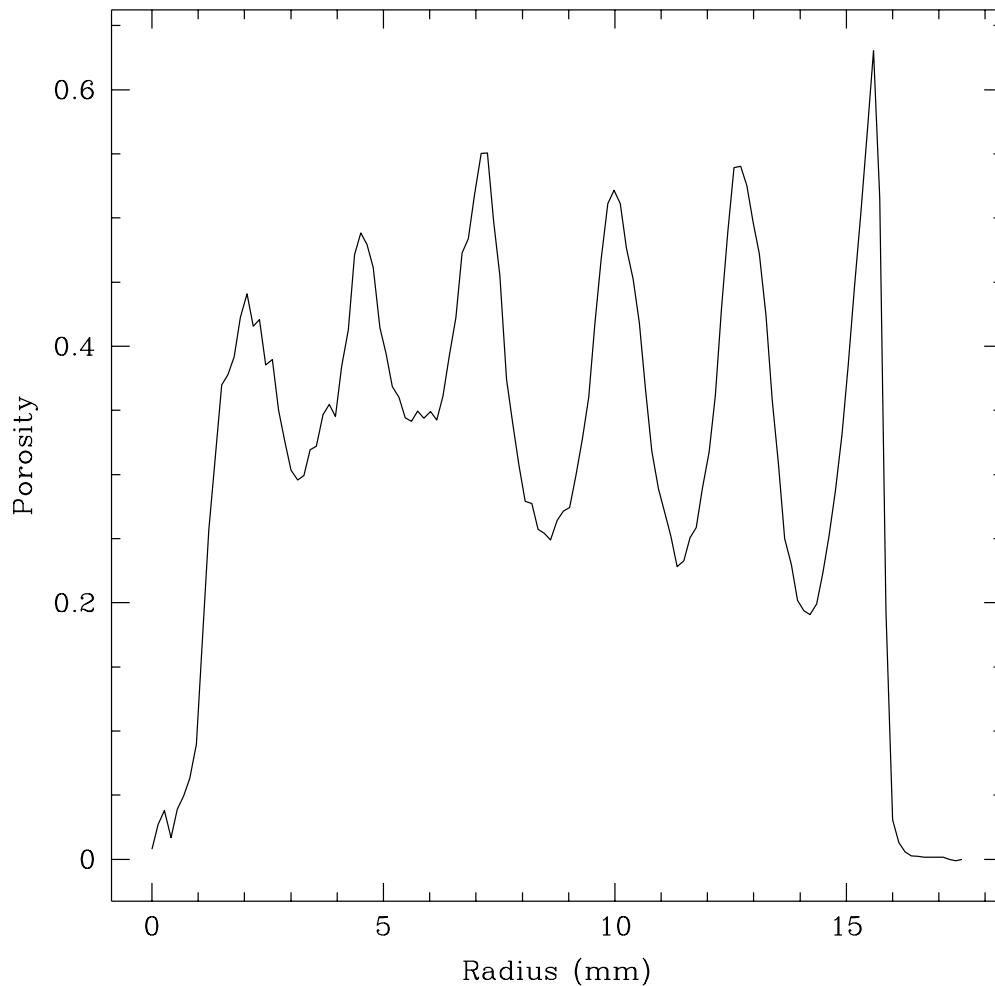


Figure 3.5: Plot of the azimuthally averaged porosity of a thin axial slice as a function of radius. A single slice, which is 0.14 mm thick was taken from a $256 \times 256 \times 256$ isotropic density acquisition of the test section in figure 3.1. This plot is the azimuthal average of that slice. The tube diameter is 3.175 mm.

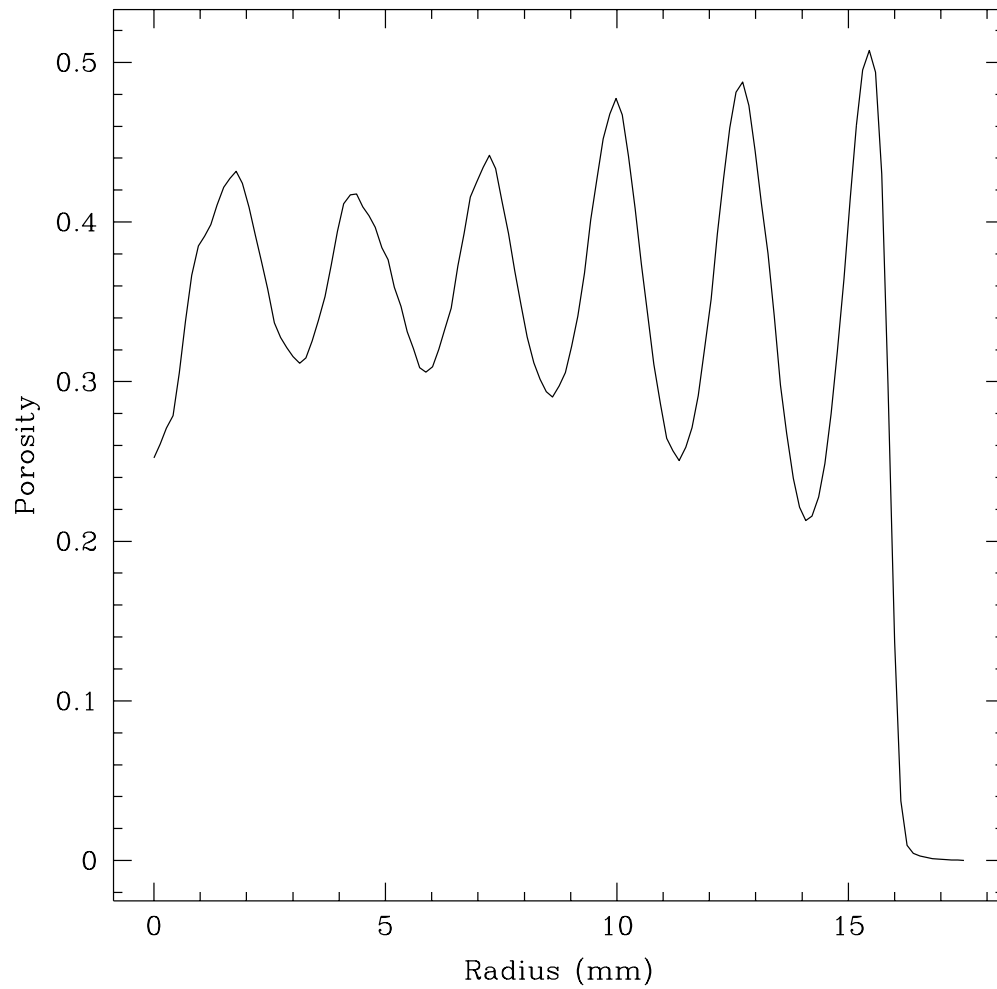


Figure 3.6: Plot of the porosity averaged azimuthally and over the \hat{z} axis as a function of radius. A thick slice, which is 35 mm or 11 bead diameters thick was taken from a $256 \times 256 \times 256$ isotropic density acquisition of the test section in figure 3.1. The slice was averaged azimuthally and over \hat{z} . The tube diameter is 3.175 mm.

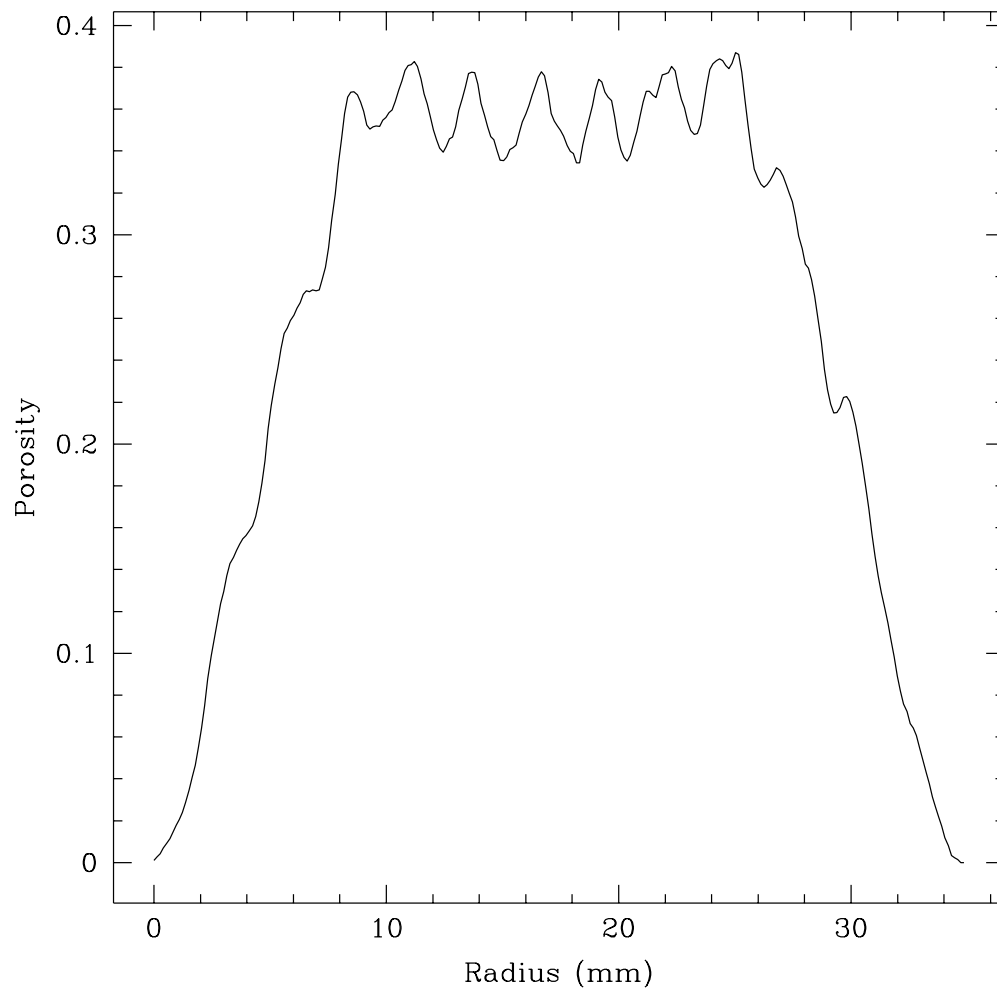


Figure 3.7: Plot of the porosity averaged over the \hat{x} and \hat{y} axes as a function of z from a $256 \times 256 \times 256$ isotropic density acquisition of the test section in figure 3.1. The tube diameter is 3.175 mm.

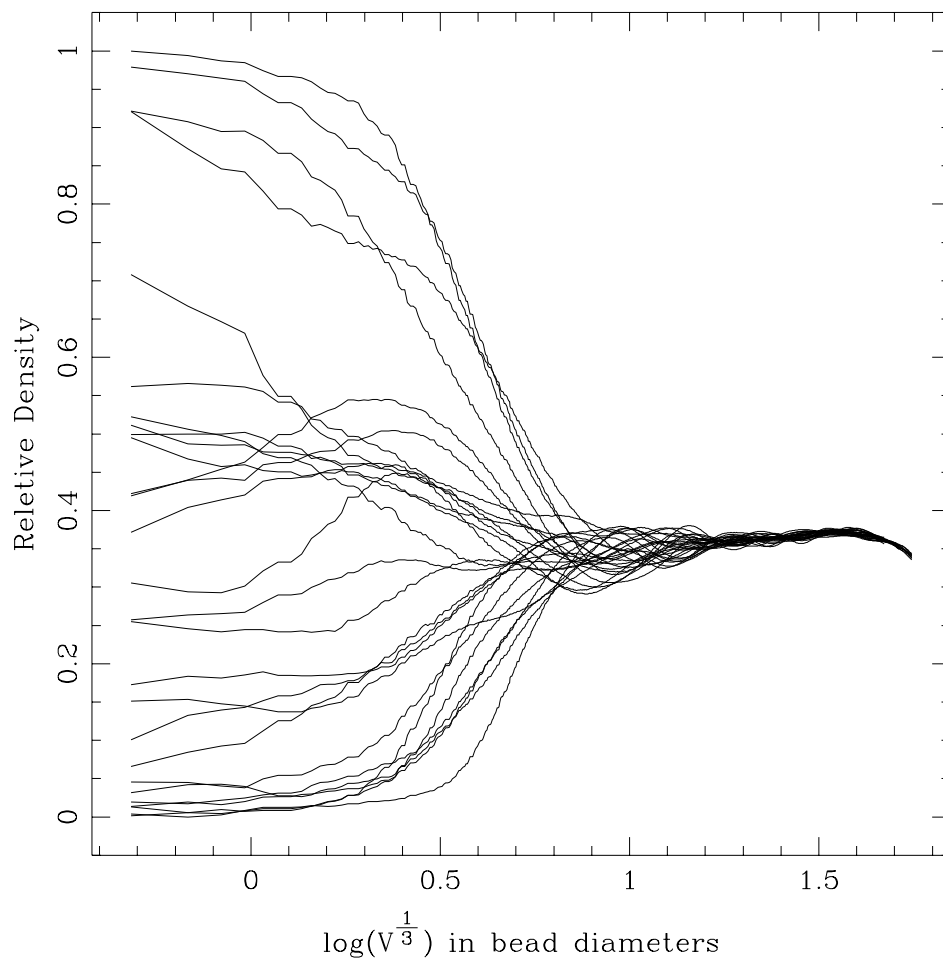


Figure 3.8: Graph of porosity as a function of averaging volume, V_{rev} , for 27 random starting positions within the central region.

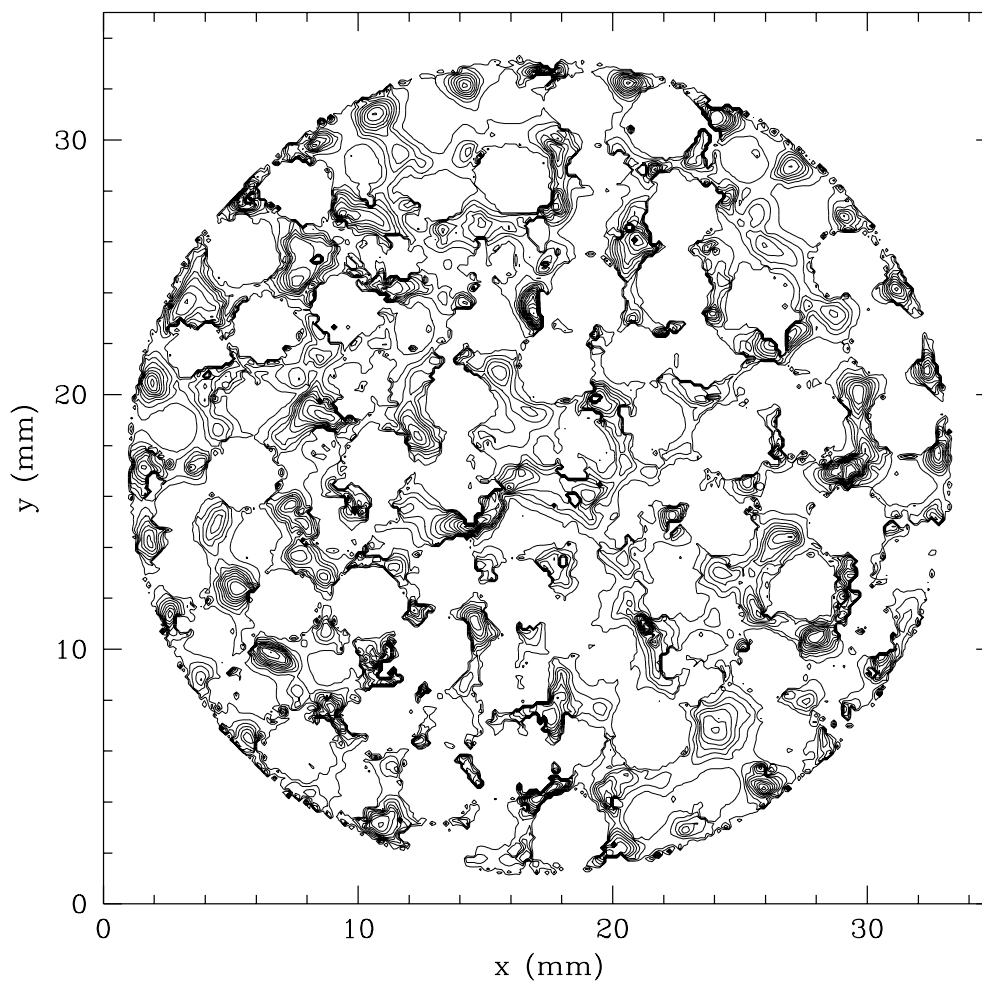


Figure 3.9: Axial velocity contours in a cross-section of a packed bed during pressure driven flow. The velocity is averaged in the flow direction over a 2 mm slice. Each velocity contour represents 0.8 mm s^{-1} .

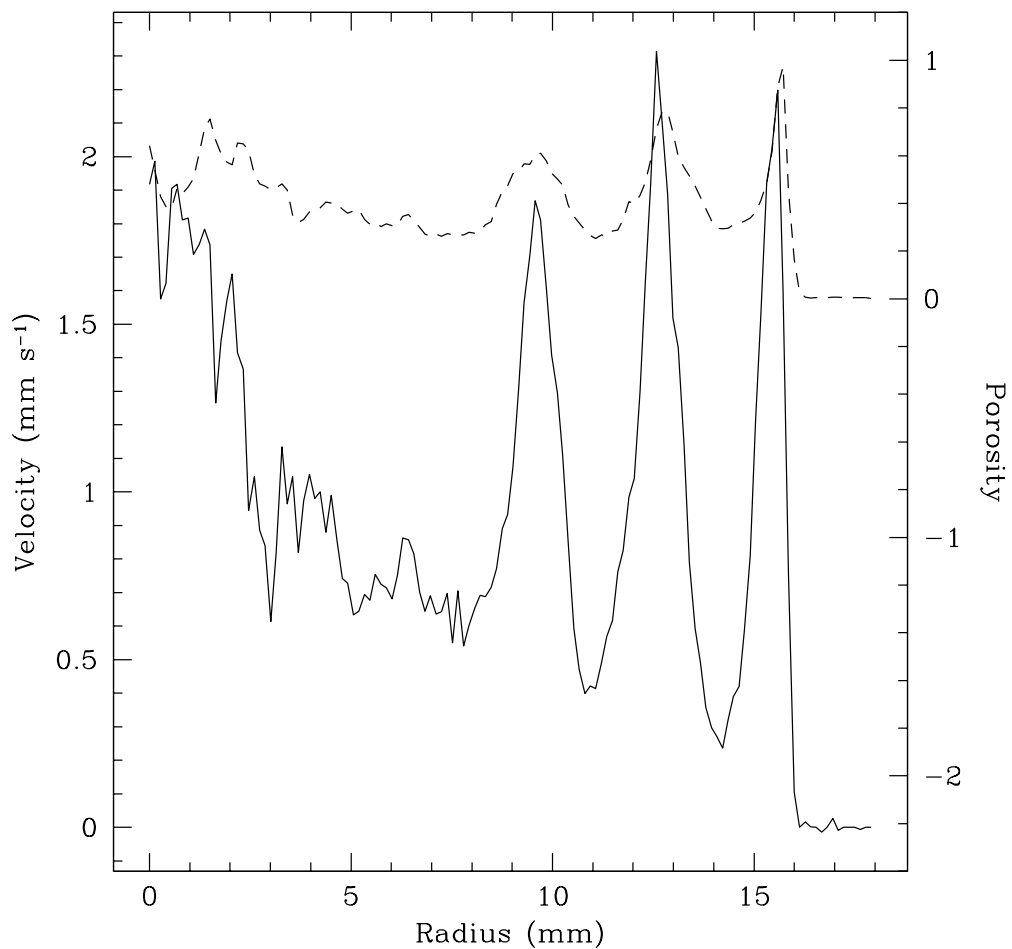


Figure 3.10: Graph showing flow channelling in a 15.9 mm radius pipe packed with 3.2 mm beads. The azimuthally averaged, axial velocity profile in a 2 mm axial slice is shown with the solid line. The azimuthally averaged porosity is shown as a dashed line. The velocity is highest in the regions of largest porosity near the wall.

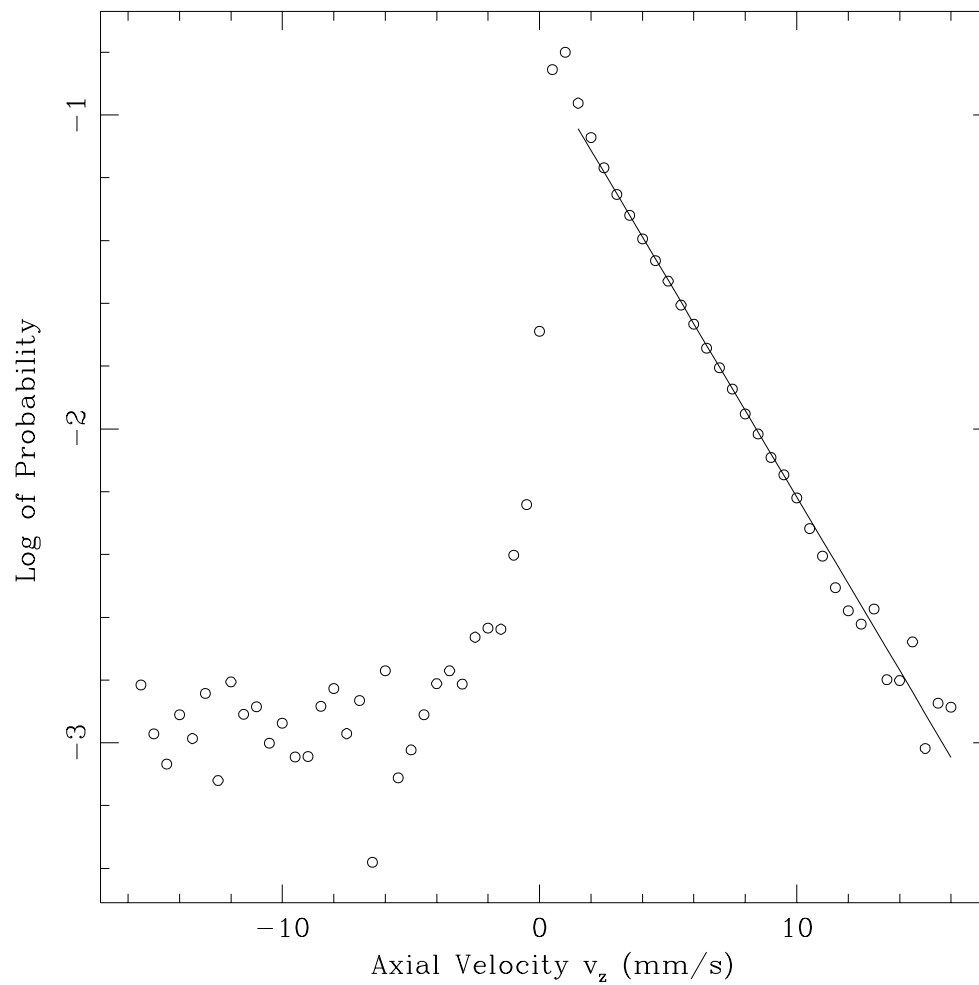


Figure 3.11: A graph showing the distribution of velocities integrated over a 2 mm slice perpendicular to the flow direction in a 3.175 mm pipe filled with 3.2 mm beads. For comparison the distribution of velocities for bulk pipe flow is shown in figure 2.3

3.5.3 Flow Channeling

We measure the distribution of velocities at each point on a (256×256) grid in a 2 mm slice when the fluid is driven by a uniform pressure gradient through the interstitial space of the porous medium of figure 3.3. Figure 3.9 shows velocity contours in an axial slice. Note the regular arrangement of the regions with high velocity near the pipe wall. Figure 3.10 shows the axial velocity profile on the same slice, averaged azimuthally. The porosity distribution like the one in figure 3.5 is also shown in this plot and correlates well with the three peaks near the tube wall.

With few exceptions, all previously reported velocity profiles in columnar packed beds have been obtained outside the bed. Nevertheless, such measurements reveal that the fluid velocity reaches a peak at about 1–2 particle diameters from the solid wall, while the flow is fairly uniform, statistically, in the core. This flow enhancement near the solid walls is referred to as the channeling phenomenon. Schwartz & Smith (1953), using hot-wire anemometry, found that the peak velocity was 30-100% greater than the core velocity when the bed-to-particle diameter ratio was less than 30. Volkov, Reznikov, Khalilov, Zel'vensky & Sakodynsky (1986) used laser velocimetry to study the statistics of local velocity variation in a cross section at the bed outlet. Recently, Northrup et al. (1991) reported interstitial velocity profiles in the interior of packed beds obtained by particle tracing.

3.5.4 Velocity Distributions

Figure 3.11 shows the distribution of velocities integrated over the whole slice. Note that these data are presented on a logarithmic-linear plot. The striking

feature which has never been documented before, to our knowledge, is the exponential distribution of velocities. The distribution of axial velocities obtained by Northrup et al. (1991) shows some qualitative similarities, but as noted previously, they probably do not have enough data to determine the functional dependence. Here, we have included data near the walls, since in the present apparatus the wall effects penetrate a substantial way across the cylinder. The effect of tube-to-particle diameter ratio was investigated numerically by Chu & Ng (1989). Their data also agree qualitatively with our findings.

3.6 Conclusions

We demonstrate the suitability of MRI velocity measurement in porous media. These studies give the first non-invasive quantitative velocity measurement in the interstitial spaces of a three-dimensional porous media. As well as velocity information, MRI provides the relative density on a microscopic spatial scale. In the past, density measurements were tedious and destructive. Using the density measurements we verified the oscillatory nature of the porosity in packed spheres, and the inherent long range order, even in disordered media.

We determined the velocity profile in a packed bed of spheres driven by an external pressure gradient. The profiles verify theoretically predicted flow channelling inside the medium for the first time. We also report the interesting result that the distribution of velocities is exponential. To our knowledge, this result has never been observed or predicted.

3.7 Future Directions

There are several possible follow-up experiments for future investigation. We have not yet looked at the effect of bead diameter on the flow pattern or the distribution of velocities. The use of poly-disperse material would further randomize the system. And we have not yet studied the effect of velocity, except over a small range of $1-10Re$.

Chapter 4

Porous Media Convection

4.1 Introduction

As mentioned previously, porous media convection, PMC, has many technical applications. In addition to these applications PMC is also an interesting nonlinear pattern forming system. Interest in pattern formation in nonlinear systems has recently increased as advances have been made as a result of precisely controlled experiments in conjunction with new analytical and computational advances. Rayleigh-Bénard convection, RBC, the bulk fluid analog to PMC, represents one of the canonical and most studied pattern forming systems (Cross & Hohenberg, 1993). The advances in understanding RBC are due in part to its amenability to theoretical analysis and to the ease of visualization with the shadowgraph technique (Busse & Whitehead, 1971). Theoretically PMC and RBC are similar in a number of ways. For example, PMC has simpler governing equations than RBC but still contains many of the interesting features of RBC, like a finite-wavenumber instability, nonlinear pattern selection, and secondary instabilities. In PMC the momentum equation is linear, and the only nonlinearity comes from the coupling of the velocity and temperature field in the heat equation. Also, in PMC the vertical vorticity de-

cays away quickly, which provides an interesting test of the relation of vertical vorticity to the complex dynamics observed for low to moderate Pr fluids in RBC (Siggia & Zippelius, 1981; Morris, Bodenschatz, Cannell & Ahlers, 1993).

Despite these similarities, our understanding of PMC has lagged behind that of RBC, especially in experiments. This is due in part to the fact that PMC is difficult to visualize, since visible light is dispersed by the solid matrix in porous media. Until recently, there were no effective PMC visualization techniques with the ability to determine the convection pattern non-invasively. The current lack of and need for better visualization and local velocity information has been pointed out in recent reviews by Torrance et al. (1982) and Georgiadis (1991).

4.2 Previous Experiments

Most experimental data in PMC are limited to heat transfer measurements (Schneider, 1963; Katto & Masuoka, 1967; Combarous, 1970; Kaneko, Mohade & Aziz, 1974; Yen, 1974; Buretta & Berman, 1976). Visualization techniques in the past have been invasive, limited to special geometries or to a few points. Further, there was no quantitative velocity information. Elder (1967) visualized Hele-Shaw convection to gain qualitative information about PMC based on the correspondence between Hele-Shaw equations and PMC equations. Prasad, Kulacki & Keyhani (1985) used point measurement techniques, inserting thermocouples into the convection cell to map the temperature. Bories & Thirriot (1969) observed PMC with a free upper surface using aluminum particles sprinkled on a thin layer of fluid above the medium. Beckermann, Viskanta & Ramadhyani (1988) studied a convective system with

vertical layers of porous media and clear fluid. They visualize the temperature patterns in the bulk fluid and use that information to infer the pattern in the porous region. Lister (1990) visualized convection from above through a thin transparent teflon sheet with stainless steel mesh underneath. The mesh helped to maintain isothermal boundary conditions and served as the cathode in electrolysis. He placed thirteen graphite slabs in the medium to serve as anodes, and visualized the fluid pattern with a pH indicator in the fluid. The electrolysis produced local alkaline regions near the anodes and caused the pH indicator to change color. The colored fluid was then carried to the top of the cell by the convection. While this technique allows visualization in a system is closer to the standard theoretical conditions than many of the previous methods, it is still quite invasive. The graphite plates represented a large spacial perturbation and the fluid was not pure. Also, he did not indicate the effectiveness of the mesh in eliminating horizontal temperature gradients. Lein & Tankin (1992) used a technique based on the Christiansen filter concept to visualize temperature profiles in two-dimensional PMC. This technique works well for this geometry, but it cannot be used to determine three-dimensional patterns. Recently, Howle, Behringer & Georgiadis (1993) used a modified shadowgraph technique to visualize PMC with a special matrix that has all surfaces either parallel or perpendicular to the incoming light rays. While this technique is non-invasive, it is limited to special media and does not provide velocity information. Our work represents the first quantitative velocity profiles in PMC and the first visualization for PMC in a packed bed of spheres, one of the most common ways to create a porous medium in the laboratory. By using MRI we can measure the local density, velocity, and temperature of a flowing fluid, such as water.

4.3 Theory

4.3.1 Equations of motion

Natural PMC was first described theoretically by Horton and Rodgers (Horton & Rodgers, 1945) and Lapwood (Lapwood, 1948). They discuss the porous media analogy to RBC, a homogeneous isotropic fully-saturated porous medium heated from below. The system has uniform height, h , in the z direction and infinite horizontal extent. The temperature is specified on the horizontal boundaries, $T(z = -h/2) = T_1$ and $T(z = +h/2) = T_2$. We define a reference temperature $T_0 = (T_1 + T_2)/2$ and the temperature difference, $\Delta T = (T_1 - T_2)/2$. In the case of convection there is a buoyant force on the fluid which must be added to Darcy's law (3.6). We also include an acceleration term (Nield & Bejan, 1992), which gives

$$\rho_0 a \frac{\partial \mathbf{v}}{\partial t} = -\nabla P - \frac{\eta}{K} \mathbf{v} - \rho_f g \hat{z} \quad (4.1)$$

as the momentum equation. Here, g is the acceleration due to gravity, and a is a media-dependent acceleration coefficient, assumed to be of order one (Nield & Bejan, 1992). In (4.1) we have also used the Oberbeck-Boussinesq approximation (Oberbeck, 1879; Boussinesq, 1903). Under this approximation all fluid parameters are assumed independent of T and P , except in the buoyancy term, the fluid density, $\rho_f = \rho_0(1 - \beta(T - T_0))$, where β is the coefficient of thermal expansion. From (3.3) the equation for mass conservation is

$$\nabla \cdot \mathbf{v} = 0 \quad (4.2)$$

for incompressible fluid saturating a uniform porous medium. The temperature varies according to the heat equation,

$$(\rho c)_m \frac{\partial T}{\partial t} + (\rho c_P)_f \mathbf{v} \cdot \nabla T = k_m \nabla^2 T, \quad (4.3)$$

where c is the specific heat, k is the thermal conductivity and the m subscripts refer to properties of the porous medium and fluid combined, and f subscripts refer to the fluid properties only. The boundary conditions for \mathbf{v} are $v_z(z = \pm h/2) = 0$, and the boundary conditions on T are given above. For the theoretical case the lateral boundaries are assumed to be at infinity. For the experimental case, we have chosen insulating lateral boundary conditions. One solution to (4.1), (4.2), and (4.3) is

$$\mathbf{v}_c = 0 \quad (4.4)$$

$$T_c = T_0 - \frac{\Delta T z}{h} \quad (4.5)$$

$$P_c = P_0 + \rho_0 g \left(z + \frac{\beta}{2h} z^2 \right), \quad (4.6)$$

where P_0 is pressure at $z = 0$. This represents pure conduction of heat through the layer, with the fluid stationary.

Using h , $(\sigma h^2)/\alpha_m$, α_m/h , and $\Delta T/Ra$ as the scale for length, time, velocity, and temperature respectively (4.1), (4.3), and (4.2) become

$$\frac{A}{Pr} \frac{\partial \mathbf{u}}{\partial t} = -\nabla P - \mathbf{u} + \theta \hat{z} \quad (4.7)$$

$$\frac{\partial \theta}{\partial t} + \mathbf{u} \cdot (\nabla \theta - Ra \hat{z}) = \nabla^2 \theta \quad (4.8)$$

$$\nabla \cdot \mathbf{u} = 0, \quad (4.9)$$

where

$$Ra = \frac{\beta K h g \Delta T}{\nu \alpha_m} = 4 \Delta T, \quad (4.10)$$

$$Pr = \frac{\nu}{\alpha_m} = 9.09, \quad (4.11)$$

$$Da = \frac{K}{h^2} = 3 \times 10^{-5}, \quad (4.12)$$

$$A = \frac{a Da}{\sigma} = 5 \times 10^{-5} a, \quad (4.13)$$

$$\sigma = \frac{(\rho c)_m}{(\rho c_P)_f} = .597, \quad (4.14)$$

$$(4.15)$$

and

$$\alpha_m = \frac{k_m}{(\rho c_P)_f} = 7.24 \times 10^{-4} \text{ cm}^2 \text{ s}^{-1}, \quad (4.16)$$

where Ra is the Rayleigh number, Pr is the Prandtl number, Da is the Darcy number, A is the non-dimensional acceleration coefficient, σ is the heat capacity ratio, and α_m is the diffusivity of the medium. Here the numerical values are based on the parameters of our system, which are given in table 4.1. The non-dimensional velocity, \mathbf{u} , and temperature, θ , are related to \mathbf{v} and T by

$$\mathbf{u} = \frac{h}{\alpha_m} \mathbf{v} \quad (4.17)$$

and

$$\theta = \frac{Ra}{\Delta T} \left(T - \left[T_0 - \frac{\Delta T z}{h} \right] \right). \quad (4.18)$$

θ measures the deviation of the temperature from the conduction solution (4.4). P has also been modified to absorb any terms which can be written as gradients.

Our choice of temperature scale is different from most in the literature, but, for comparison, leads to non-dimensional equations which are closer to those used in the RBC literature.

The parameters in (4.10-4.14) and the scaling factors provide insight into PMC. Ra is the Rayleigh number and is a non-dimensional measure of ΔT . Ra is the ratio between $\eta\alpha_m K^{-1}$ and $\rho_0 g h \beta \Delta T$. The viscous terms, $\eta\alpha_m$, and the resistance to flow, K^{-1} , both tend to keep the fluid from moving. The buoyancy term, $\rho_0 g h \beta \Delta T$, tends to make the fluid move. Ra is a measure of the state of the competition between these two tendencies. When Ra is below a critical value, Ra_c the fluid is stationary, but when $Ra > Ra_c$ it begins to move. Pr and A determine the relative importance of the acceleration term. Da is the Darcy number and is a non-dimensional measure of the permeability. In our experiment, $Da = 3 \times 10^{-5}$ based on (3.9), which implies that A is small. Da is typically small and the acceleration term is often neglected. σ is the heat capacity ratio, which modifies the thermal time scales. The time scale, $\tau_v = (\sigma h^2)/\alpha_m$ or vertical thermal diffusion time, is a measure of the relevant time for thermal changes to propagate from the bottom of the cell to the top. The horizontal diffusion time is $\tau_h = \Gamma^2 \tau_v$, where Γ is the aspect ratio of the cell. Γ is defined as L/h , where L is a typical lateral dimension of the cell.

4.3.2 Additional terms

As discussed in (§3.3), there are several additional terms which can be added to the momentum equation, (4.1) to account for deviations from Darcy's law at high velocities. To determine whether we should include one of the higher order terms we add the quadratic term from (3.11) to (4.1) and non-dimensionalize

to obtain:

$$\frac{A}{Pr} \frac{\partial \mathbf{u}}{\partial t} = -\nabla P - \mathbf{u} - \frac{c_F \sqrt{Da}}{Pr} |\mathbf{u}| \mathbf{u} + \theta \hat{z}. \quad (4.19)$$

We determine the relative importance of linear and quadratic terms through their ratio:

$$\frac{c_F \sqrt{Da}}{Pr} |\mathbf{u}| = \frac{c_F \sqrt{K}}{\nu} |\mathbf{v}|.$$

This ratio is called the Reynolds number, Re . Ward (1964) determined that when $Re < c_F \simeq 0.55$, the quadratic term is not important. For our case from table 4.1, $Re = 0.6 \text{ s cm}^{-1} |\mathbf{v}|$. Our typical maximum velocity at the highest Ra is less than 2 mm s^{-1} , which gives $Re = 0.12$.

Linear stability analysis has been applied to (4.7-4.9) (Lapwood, 1948). It is found that the uniform conduction state loses linear stability to a finite-wavelength, λ , disturbance at $Ra_c = 4\pi^2$. The value for Ra_c has been verified by several heat transport experiments (Comberous & Bories, 1975; Close, Symmons & White, 1985, for example). We define a reduced Ra ,

$$\epsilon = \frac{Ra - Ra_c}{Ra_c}, \quad (4.20)$$

such that, $\epsilon = 0$ at onset and increases proportionally to Ra . The critical wavenumber, $q_c = 2\pi h/\lambda_c$, is found to be π .

While linear analysis can determine the wavelength of the new state, it cannot predict the three-dimensional pattern. Nonlinear analysis predicts two-dimensional roll states near onset for systems with vertical mid-plane symmetry (Busse, 1985). In most experiments in which the pattern is determined, it is found to be hexagonal or polygonal (Bories & Thirriot, 1969; Lister, 1990). Bories & Thirriot and Nield & Bejan (1992) attribute this to broken

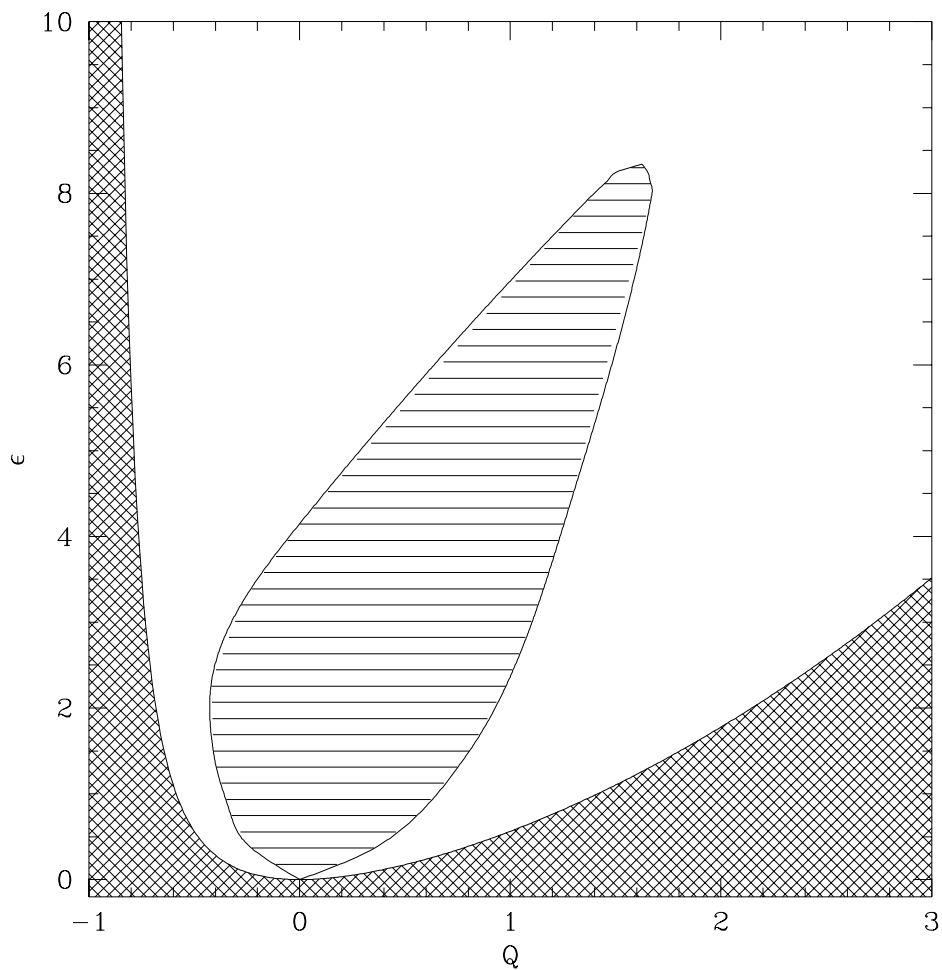


Figure 4.1: Stability diagram determined by Strauss (1974). The hatched region is the conducting state. The stripped region is stable.

symmetry in the boundary conditions. However, Howle et al. (1993) have obtained straight parallel rolls using a special media. Further stability analysis has been done to determine secondary instabilities (Strauss, 1974; Strauss & Schubert, 1978). In these studies the stability of two-dimensional rolls to three-dimensional disturbances is determined. Strauss (1974) shows that two-dimensional rolls lose stability to a cross roll state at $\epsilon = 4$. We show a diagram of the stability of different wavelength disturbances as a function of ϵ in figure 4.1. This graph, known as a stability diagram, was by calculated by Strauss (1974). The lowest curve in that diagram is called the neutral or marginal stability curve. Points below the curve are in the conduction state and points above are in the convective state. Because there is a single minimum point on this curve, when ϵ is slowly raised to 0 only one wavelength becomes unstable.

The neutral stability curve is easily derived from (4.7-4.9). The first step is to linearize the equations about the conduction solution. We let

$$\mathbf{u} = \mathbf{u}_c + \delta\mathbf{u},$$

$$\theta = \theta_c + \delta\theta,$$

and

$$P = P_c + \delta P,$$

where $\delta\theta$, $\delta\mathbf{u}$, and δP are infinitesimal disturbances, and θ_c , \mathbf{u}_c , and P_c are the non-dimensional conduction solutions. From (4.4), (4.18) and (4.17) we see that $\theta_c = 0$, and $\mathbf{u}_c = 0$. Substituting these fields into (4.7-4.9) and eliminating second order terms we obtain,

$$\frac{A}{Pr} \frac{\partial \delta\mathbf{u}}{\partial t} = -\nabla\delta P - \delta\mathbf{u} + \delta\theta\hat{z} \quad (4.21)$$

$$\frac{\partial \delta \theta}{\partial t} + -Ra \delta u_z = \nabla^2 \delta \theta \quad (4.22)$$

$$\nabla \cdot \delta \mathbf{u} = 0. \quad (4.23)$$

We apply the curl operator twice to (4.21) and use (4.23) to obtain:

$$\left(\frac{A}{Pr} \frac{\partial}{\partial t} + 1\right) \nabla^2 \delta u_z = \left(\frac{\partial^2}{\partial x^2} + \frac{\partial^2}{\partial y^2}\right) \delta \theta. \quad (4.24)$$

We now examine the stability of solutions to (4.22) and (4.24) of the form:

$$\delta u_z = U_z(z) \exp(\varsigma t + i q_x x + i q_y y) \quad (4.25)$$

and

$$\delta \theta = \Theta(z) \exp(\varsigma t + i q_x x + i q_y y). \quad (4.26)$$

Combining these with (4.22) and (4.24) we obtain:

$$\left(\frac{\partial^2}{\partial z^2} - q^2 - \varsigma\right) \Theta(z) = -Ra U_z(z) \quad (4.27)$$

$$\left(1 + \frac{A}{Pr} \varsigma\right) \left(\frac{\partial^2}{\partial z^2} - q^2\right) U_z(z) = -q^2 \Theta(z), \quad (4.28)$$

where $q = \sqrt{q_x^2 + q_y^2}$. We eliminate $\Theta(z)$ from (4.27-4.28) and obtain

$$\left[\left(1 + \frac{A}{Pr} \varsigma\right) \left(\frac{\partial^2}{\partial z^2} - q^2 - \varsigma\right) \left(\frac{\partial^2}{\partial z^2} - q^2\right) - q^2 Ra\right] U_z(z) = 0. \quad (4.29)$$

The boundary conditions on the dimensional parameters, as mentioned above, are $T(z = -h/2) = T_1$, $T(z = +h/2) = T_2$, and $v_z(z = \pm h/2) = 0$. Then, $U_z(z = \pm \frac{1}{2}) = 0$, and $\Theta_z(z = \pm \frac{1}{2}) = 0$. Finally, evaluating (4.28) at $z = \pm \frac{1}{2}$ we obtain the four boundary conditions needed to solve (4.29):

$$U_z(z = \pm \frac{1}{2}) = \frac{\partial^2 U_z(z = \pm \frac{1}{2})}{\partial z^2} = 0.$$

The solution to (4.29) with these boundary conditions is

$$U_z(z) = \cos(n\pi z), \quad (4.30)$$

where

$$n = \frac{1}{\pi} \sqrt{\frac{\sqrt{(1 + \frac{A}{Pr}\zeta)(4q^2 Ra + \zeta^2(1 + \frac{A}{Pr}\zeta)) - (2q^2 + \zeta)(1 + \frac{A}{Pr}\zeta)}}{2(1 + \frac{A}{Pr}\zeta)}},$$

and n must be a non-zero integer. From this requirement we determine that

$$Ra = \frac{((n\pi)^2 + q^2)((n\pi)^2 + q^2 + \zeta)(1 + \frac{A}{Pr}\zeta)}{q^2}. \quad (4.31)$$

From (4.25) we see that the criterion for stability of the solution is that $\text{Re}(\zeta) < 0$. Otherwise, δu_z will grow exponentially. To determine the marginal stability we set $\zeta = 0$, and obtain

$$Ra = \frac{((n\pi)^2 + q^2)^2}{q^2}. \quad (4.32)$$

The minimum of this function is $Ra = 4\pi^2$ when $n = 1$ and $q = \pi$. This function with $n = 1$ is the lowest line plotted in figure 4.1 and is called the neutral or marginal stability curve.

4.3.3 Amplitude equations

Above, but near the threshold of a nonlinear instability, it is possible to derive amplitude equations, which describe the large scale envelope of a basic state (Newell & Whitehead, 1969; Segel, 1969). In this regime the bifurcation parameter is small and can be used with multiple scales perturbation methods

to produce a small number of amplitude equations describing the universal behavior of large classes of systems. In PMC the bifurcation parameter is ϵ . PMC and RBC belong to the class I_s (Cross & Hohenberg, 1993) systems as defined by linear stability analysis. Class I_s or stationary periodic, includes any non-linear system which loses stability of a uniform state to a time-independent finite-wavelength pattern. For a base state of straight parallel rolls, the form of the amplitude equation for all isotropic systems with a type I_s instability is the same:

$$\tau_0 \frac{\partial \mathbf{A}}{\partial t} = \epsilon \mathbf{A} + \xi_0^2 \left[\frac{\partial}{\partial x} - \left(\frac{i}{2q_c} \right) \frac{\partial^2}{\partial y^2} \right]^2 \mathbf{A} - g_0 |\mathbf{A}|^2 \mathbf{A}. \quad (4.33)$$

Here, τ_0 , ξ_0 , and g_0 are the scales for time, space, and amplitude, respectively. q_c is the wavenumber at onset, defined above, and $\mathbf{A}(x, y, t)$ is a complex amplitude which depends on space and time. All of the variation near onset among different members of this class comes through the parameters τ_0 , ξ_0 , q_c , and g_0 . In the case of PMC and RBC the amplitude and the basic state defined by the wavenumber determine the velocity and the temperature field as follows:

$$U(x, y, z, t) = U_o(z) [\mathbf{A}(x, y, t) \exp(i q_c x) + \mathbf{A}^*(x, y, t) \exp(-i q_c x)] + \mathcal{O}(\epsilon), \quad (4.34)$$

where U can be the velocity in any direction or the temperature, and U_o is determined from linear analysis. For concreteness we have assumed that the base state is parallel rolls in the \hat{x} direction.

Two of the three scales, τ_0 and ξ_0 , can be derived from the linear stability analysis above. Specifically, we solve (4.31) for ς and use (4.20) and $Ra_c = 4\pi^2$

to eliminate Ra in favor of ϵ .

$$\varsigma(q, \epsilon) = \frac{-QB + \sqrt{Q^2B^2 - 4\frac{A}{Pr}Q(Q^2 - 4\pi^2q^2(1 + \epsilon))}}{2\frac{A}{Pr}Q}, \quad (4.35)$$

where $Q = q^2 + (n\pi)^2$ and $B = 1 + \frac{A}{Pr}Q$. The time and space scales are related to $\varsigma(q, \epsilon)$ by

$$\tau_0 = \left(\left. \frac{\partial \varsigma(q, \epsilon)}{\partial \epsilon} \right|_{q=\pi, \epsilon=0, n=1} \right)^{-1} = \frac{1 + 2\pi^2 \frac{A}{Pr}}{2\pi^2} = \frac{1 + 19.739 \frac{A}{Pr}}{19.739} \quad (4.36)$$

and

$$\xi_0 = \sqrt{\left. -\frac{\tau_0}{2} \frac{\partial^2 \varsigma(q, \epsilon)}{\partial q^2} \right|_{q=\pi, \epsilon=0, n=1}} = \frac{1}{\pi} = .3183. \quad (4.37)$$

Typically, $\frac{A}{Pr}$ is small and can be ignored, in which case, $\tau_0 = (2\pi^2)^{-1}$. The scale for the amplitude, g_0 is difficult to calculate and will not be attempted here.

4.3.4 Symmetry

Equations (4.7-4.9) remain the same under the following transformation:

$$\begin{aligned} z &\rightarrow -z \\ \mathbf{u}_z &\rightarrow -\mathbf{u}_z \\ \theta &\rightarrow -\theta. \end{aligned}$$

This symmetry and (4.34) show that the amplitude, A , in the amplitude equation for PMC has the symmetry $A \rightarrow -A$. This symmetry is important in determining the pattern near onset. In (§4.3.3), we described the amplitude

equations for the base state of straight parallel rolls. Amplitude equations can also be derived for a base state consisting of the superposition of multiple straight rolls (Newell & Whitehead, 1969). Of particular interest is the case where three roll directions co-exist at 60 degree angles to each other. In this state, the base pattern is hexagonal. When the symmetry $A \rightarrow -A$ is present the roll state is stable. However, if the symmetry is broken then a quadratic term appears in the amplitude equations for the hexagonal state and then the hexagon state is stable.

The symmetry in (4.7-4.9) depends on several assumptions. First, the boundary conditions must be symmetric in the \hat{z} direction. Second, Ra must be symmetric about the \hat{z} axis. This implies that none of the parameters in Ra can depend on temperature or pressure, since they both have a linear dependence on z in the conduction state. Although this criterion is never met exactly in real experiments, the range of Ra in which hexagons are stable depends on the size of the asymmetry. If parameter variations are small, then the range Ra for stable hexagons may be too small to obtain. The exact dependence of parameter variation on the stability of hexagons versus rolls has been determined for RBC (Busse, 1967) when the variation is small. However, the equivalent calculation has not been carried out for PMC.

4.3.5 Comparison of PMC and RBC

The equations of motion for RBC are:

$$\rho_0 \left(\frac{\partial}{\partial t} + \mathbf{v} \cdot \nabla \right) \mathbf{v} = -\nabla P - \eta \nabla^2 \mathbf{v} - \rho_f g \hat{z} \quad (4.38)$$

$$\rho c_P \left(\frac{\partial}{\partial t} + \mathbf{v} \cdot \nabla \right) T = k \nabla^2 T, \quad (4.39)$$

$$\nabla \cdot \mathbf{v} = 0 \quad (4.40)$$

We can use the same scales for length, time, velocity, and temperature as in the porous case to put these equations in non-dimensional form. It should be noted that the scale for time is h^2/α_m since $\sigma = 1$.

$$\frac{1}{Pr} \left(\frac{\partial \mathbf{u}}{\partial t} + \mathbf{u} \cdot \nabla \mathbf{u} \right) = -\nabla P - \nabla^2 \mathbf{u} + \theta \hat{z} \quad (4.41)$$

$$\frac{\partial \theta}{\partial t} + \mathbf{u} \cdot (\nabla \theta - Ra^{\text{rbc}} \hat{z}) = \nabla^2 \delta \theta \quad (4.42)$$

$$\nabla \cdot \delta \mathbf{u} = 0. \quad (4.43)$$

Here $Ra^{\text{rbc}} = RaDa^{-1}$. The heat and mass conservation equations are the same as in the porous case, but the momentum equation is more complicated in the case of RBC. It contains both a nonlinear term and higher-order spacial derivatives. The critical wave number for RBC is 3.117 and $Ra_c^{\text{rbc}} = 1707.76$ at the onset of convection. The time scale and length scale in the amplitude equations are:

$$\tau_0 = \frac{1 + 0.5117Pr^{-1}}{19.65} \quad (4.44)$$

and

$$\xi_0 = 0.3847. \quad (4.45)$$

They have the same Pr dependence as the PMC case. However, since A is almost always very small PMC is more like RBC when Pr is large. In fact, if $Pr \rightarrow \infty$ then the only difference in the form of the equations is the order of the velocity derivative in the momentum equation.

If we take the vertical component of the curl of (4.7) we obtain,

$$\frac{\partial \xi_z}{\partial t} = -\frac{Pr}{A} \xi_z, \quad (4.46)$$

where the vertical vorticity, $\xi_z = \nabla \times \mathbf{u} \cdot \hat{z}$. The solution to (4.46) for an arbitrary initial condition, ξ_0 , is

$$\xi_z = \xi_0 \exp\left(-\frac{Pr}{A}t\right). \quad (4.47)$$

Thus, the vertical vorticity decays with a non-dimensional time constant,

$$\frac{A}{Pr}.$$

Using the time scale defined above we see that the dimensional time constant is

$$\frac{A\sigma h^2}{\alpha_m Pr} = \frac{aK}{\nu} = 4.5 \times 10^{-3} a \text{ s}.$$

Therefore assuming that a is of order one, the vertical vorticity decays on millisecond time scales. From (4.41) it is clear that the equation for the vertical vorticity is a complicated nonlinear equation. While some researcher (Siggia & Zippelius, 1981; Morris, Bodenschatz, Cannell & Ahlers, 1993) have suggested that vertical vorticity is responsible for complicated behavior such as spiral chaos in moderate Prandtl number RBC, the role of vertical vorticity in these systems has not been settled (Greenside, Cross & W. M. Coughran, 1988; Greenside, 1995). If vertical vorticity is responsible for spiral chaos or other complicated behavior, we expect that we will not see that type of behavior. Instead we expect that PMC will be stable within the linear stability region.

4.3.6 Heat transport

The Nusselt number Nu is a non-dimensional measure of the heat transport across the medium. This quantity is easily measured and provides several important checks on theory. When the sample starts to convect the fluid

motion causes greater heat transport. The larger heat transport can be thought of as an increase in thermal conductivity. Nu is the ratio of the effective thermal conductivity caused by convection of the medium, k_{eff} , to the thermal conductivity of the medium below onset, k_0 . By combining Fourier's law of heat conduction,

$$q = -k \frac{\Delta T}{\Delta z}, \quad (4.48)$$

where q is the heat flux, with the definition of Nu we obtain

$$Nu = \frac{k_{\text{eff}}}{k_0} = \left(\frac{q}{\Delta T} \right) \left(\frac{q}{\Delta T} \right)_0^{-1}. \quad (4.49)$$

Here, the subscript 0 refers to values below the onset of convection. Both q and ΔT are easily measured. Nu is 1 below the onset of convection, but when convection begins the effective conductivity increases and Nu increases. This provides an easy way to determine the critical temperature difference, ΔT_c for the onset of convection, by plotting Nu versus ϵ . Also, $Nu(\epsilon)$ provides an important link with theory. Busse & Joseph (1972) and Gupta & Joseph (1973) determined upper bounds for $Nu(\epsilon)$. Palm, Weber & Kvernfold (1972) have found that for small ϵ , $Nu = 1 + 2\epsilon$.

4.3.7 Size of apparatus

For Darcy's law to apply, the coarseness, δ/h , must be much less than one, that is $\delta/h \ll 1$, where δ is the typical pore size. Experimentally, it is difficult to make δ small without requiring very large temperature gradients, since the permeability, K , decreases like δ^2 according to (3.9). Smaller K means that a larger ΔT is needed to produce convection. For water and 3.204 mm plastic beads at 40 °C with $h = 1$ cm, then $\Delta T_c = 10$ °C. If the beads are decreased

to 1 mm then $\Delta T_c > 100$ °C. However, h cannot simply be increased as Lister (Lister, 1990) has suggested. Since $\tau_v \propto h^2$, h cannot be too large or only transients will be observed. For the example above, $\tau_v = 16$ min and the horizontal diffusion time, τ_h , for $\Gamma = 10$ is 26 hrs. Lister used $h = 30$ cm and $\Gamma = 10$, giving a $\tau_v = 8.6$ days and a $\tau_h = 2.3$ years. For experiments which have time to relax, only $\delta/h < 1$ can be realized.

The extent to which large coarseness affects the predictions based on Darcy's law has been partially explored by Close, Symmons & White (1985). They compared Ra at the onset of convection in experiments to the theoretical value of $4\pi^2$ derived from Darcy's law. They determined that the continuum approach might be valid down to $h/\delta \sim 2$. Since the prediction that $Ra_c = 4\pi^2$ holds for $h/\delta \sim 2$ it is interesting to see what other predictions hold. They also looked at the slope of the Nu versus Ra curve and found that the coarseness had a greater effect there, noting differences from theory and other experiments up to at least $h/\delta = 5$.

In this work, in addition to the slope of the Nu versus Ra curve, we examine four other predictions: the pattern at onset, the wavenumber at onset, the stability of patterns in the stability region, and the type of patterns produced after secondary instabilities occur. These observations can only be made in a system like ours which has visualization capabilities.

4.4 Experimental Setup

4.4.1 The Convection Cell

We have constructed a convection cell that closely approximates the ideals of the theoretical description. Horizontal parallel isothermal planes separated by

Parameter	Water at 40 °C	Beads(plastic)	Medium
Thermal Expansion β (K^{-1})	3.8530×10^{-4}	6.8×10^{-5}	na
Conductivity k ($\text{W cm}^{-1} \text{K}^{-1}$)	6.27×10^{-3}	1.9×10^{-3}	3.0×10^{-3}
Density ρ (g cm^{-3})	0.9922158	1.19	1.14
Specific Heat c ($\text{J g}^{-1} \text{K}^{-1}$)	4.1786	1.470	2.173
Kinematic viscosity ν ($\text{cm}^2 \text{s}^{-1}$)	6.580×10^{-3}	na	na
Permeability K (cm^2)			
random, $\phi = .31$	na	na	4×10^{-5}
close-pack, $\phi = .26$	na	na	2×10^{-5}
close-pack, based on ΔT_c	na	na	5.5×10^{-5}

Table 4.1: Material parameters

(Unless otherwise noted, medium properties are for the close-packed cell and are calculated based on an average of the separate properties weight by the porosity.)

a distance h were constructed from 1 mm Aluminum Nitride (AlN) plates and separated by a machined Delrin spacer. Normally, at least one of the plates would be copper, but due to the r.f. fields and the rapidly changing magnetic fields produced during MRI, no metal could be used in the construction of the convection cell. AlN, a ceramic, with high electrical resistivity and high thermal conductivity, $1.33 \text{ W cm}^{-1} \text{K}^{-1}$, was used in place of copper. AlN has 1/3 the conductivity of copper, 222 times the conductivity of water, and 3.3 times the conductivity of sapphire, which is often used in high precision convection experiments with shadowgraph visualization. The high conductivity ensures that the plates are isothermal and horizontal temperature gradients will be minimized. The Delrin spacer provides insulating lateral boundary conditions, with a conductivity 1/3 that of water.

4.4.2 Temperature Control

The two AlN plates were held at a constant temperature by two temperature controlled water reservoirs. The water from these reservoirs is circulated over the plates (see figure 4.2). The baths were controlled by a laboratory computer using proportional and integral feedback to a stability of 5 mK. Temperatures were determined to 0.3 mK with thermistors at the inlets and outlets to the cell using a scanning digital multimeter connected by an IEEE interface to the laboratory computer. There was no detectable difference in the inlet and outlet temperatures. This ensures that the temperature measured outside of the cell is a good representation of the actual temperature of the top and bottom plates.

4.4.3 Planform and Packing

Several Delrin spacers were constructed with different planforms (see table 4.2). In each case, the thickness, h , varied by less than $25 \mu\text{m}$ around the spacer. The careful machining, along with a leveling bubble, ensure that the top and bottom plates are horizontal and parallel. We use $3.204 \pm .029 \text{ mm}$ mono-disperse acrylic spheres to pack the cell, and distilled, deionized water to fill the cell. For disordered packing, the spheres were simply poured into the circular cell and closed. Figure 4.3(a), a density image, reveals that the disordered packing is far from random and contains several ordered regions meeting at grain boundaries as well as other defects. Figure 4.3(b) shows that the cell is packed 3 bead-layers high.

For the ordered packing in the rectangular and hexagonal cells the beads were carefully packed into a 4-layer triangular lattice (ABCA). As explained

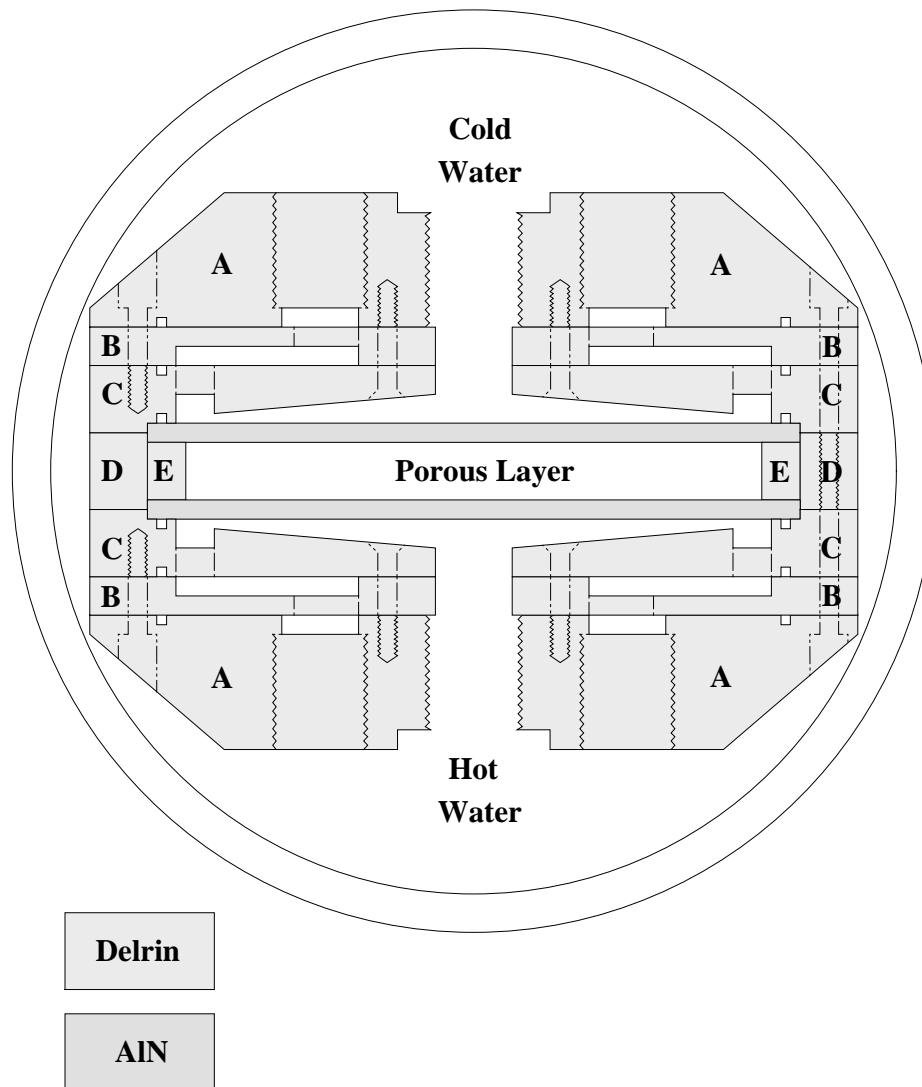


Figure 4.2: Schematic of convection cell. Hot water flows in from the bottom and cold flows in from the top. The outer circle represents the bore of the magnet, which is 15.24 cm.

Planform	Height (mm)	Width (mm)	Length (mm)	Γ
Circular	9.52	radius=47.60	na	5.00
Rectangular	10.95	51.70	87.20	7.97
Hexagonal	10.69	96.80 (corner to corner)	na	9.05

Table 4.2: Physical dimensions of various spacers.

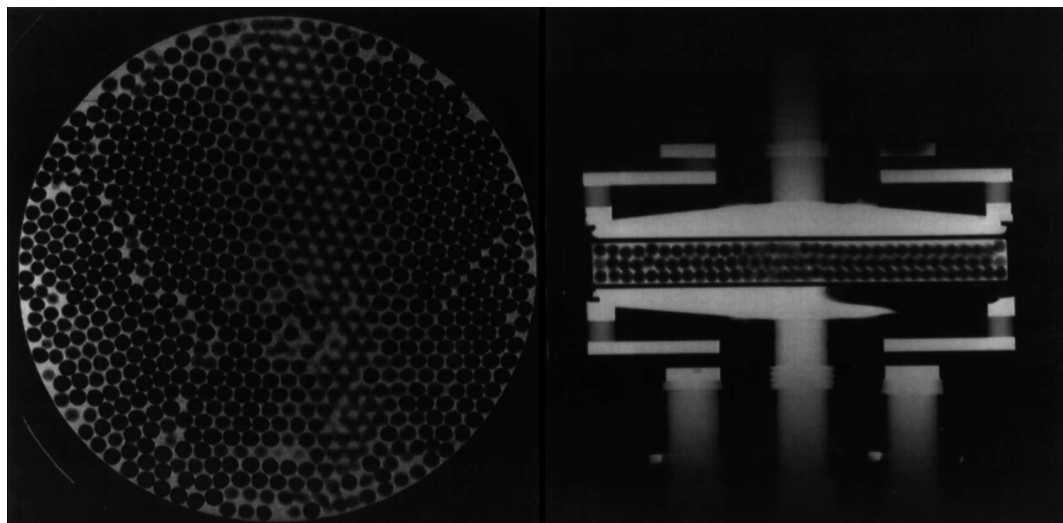


Figure 4.3: (a) Density MRI of a 1 mm horizontal slice of the disordered media. The slice is taken at approximately mid-plane. (b) Density MRI of a 8 mm vertical slice of the disordered media.

in (§4.3.7) the requirement that the pore scale $\delta \ll h$ is the only idealization which is not met to a high degree of experimental accuracy.

4.4.4 Heat Flux Measurement

It is also useful to measure the heat transport across the convective layer. This is typically an easy measurement to make. Usually, a resistive heater is used on the bottom plate. By applying a known voltage, the power input can be calculated using the known resistance of the heater. Thus, a direct measure of q is available. A measurement of the top and bottom plate temperatures completes the information needed to determine Nu from (4.49). However, we found that the presence of the heater, a conductor, interfered with the r.f. field needed for MRI. Thus, we used a different technique, adding two extra layers to the bottom AlN plate. First a thin layer of lexan is added below the AlN and then another layer of AlN is added below the lexan forming a sandwich as in figure 4.4. Since there are only vertical boundaries between the isothermal plates, the heat flux is constant in each region. The total heat flow rate through the sandwich is $Q_s = A_s q_s$, where A_s is the area of the sandwich perpendicular to the direction of heat flow. Likewise, the total heat flow rate through the Delrin spacer, is $Q_D = A_D q_D$, where A_D is the area of the spacer and the total heat flow rate through the medium is $Q_m = A_m q_m$, where A_m is the area of the medium. By conservation of energy, $Q_s = Q_D + Q_m$. Combining this with (4.48) and solving for k_m ,

$$k_m = \frac{C_s \left(\frac{T_1 - T_2}{T_1 - T_3} \right) - A_D k_D}{A_m}, \quad (4.50)$$

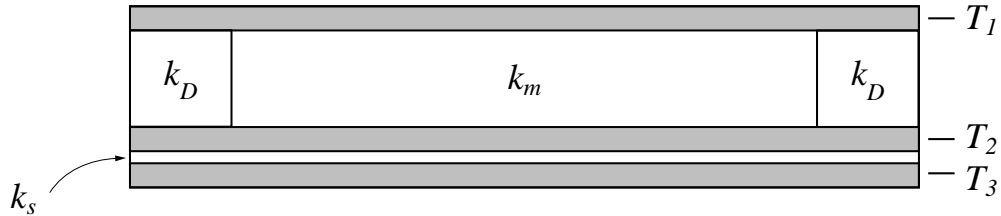


Figure 4.4: Cross section of experimental cell, Delrin spacer, and Nu measurement sandwich. T_1 , T_2 , and T_3 are measured temperatures. k_D , k_s , and k_m are the conductivity of the Delrin spacer, the sandwich, and the medium, respectively.

where $C_s = A_s k_s h / H$ and H is the height of the sandwich. Below the convective onset, using the known conductivity of the medium (table 4.1), C_s can be measured using the following rearrangement of (4.50):

$$C_s = (A_m k_m + A_D k_D) \left(\frac{T_1 - T_3}{T_1 - T_2} \right)_0, \quad (4.51)$$

where the 0 subscript refers to measurements below onset. Combining (4.50) and (4.51) with (4.49) Nu can be determined using

$$Nu = (1 + \Lambda) \left(\frac{T_1 - T_2}{T_1 - T_3} \right) \left(\frac{T_1 - T_3}{T_1 - T_2} \right)_0 - \Lambda, \quad (4.52)$$

where $\Lambda = (A_D k_D) / (A_m k_m)$. For the hexagonal cell using the relation $k_m = \phi k_w + (1 - \phi) k_p$, where k_w is the conductivity of water, k_p is the conductivity of the plastic beads, and ϕ is the porosity of the medium, $\Lambda = 1.0$. In general, the conductivity of the medium must be known from a relation like the one above or measured in order to use (4.52) to calculate the Nu .

For the disordered experiments the Nu measurement apparatus was not in place, and our determination of ΔT_c has a 20 percent error. For the rectangular measurements, ΔT_c was determined from images at 0.5 °C increments, which gives a relative accuracy of 5 percent. For the hexagonal planform, we used

both images and Nu to determine ΔT_c . The determination of Ra_c in all cases is complicated by the fact that permeability is difficult to measure and (3.9) does not give high accuracy. We have made two determinations of K . First we used (3.9). Second, K can be calculated from $Ra_c = 4\pi^2$ and the medium and fluid material properties. These results, which differ by a factor of two, are in table 4.1. Thus, determination of Ra_c is difficult. However ϵ only depends on ΔT and ΔT_c , since all other parameters in Ra are constant. We will use ϵ exclusively.

4.5 Results

4.5.1 Disordered media

The pattern selection in the disordered media is dominated by the defects in the packing. In figure 4.5, velocity images for the disordered medium in figure 4.3 are shown at several values of ϵ , which is defined by Ra_c of the ordered regions. Figure 4.5(a) shows the circular cell well below convective onset. In figure 4.5(b), $\epsilon = -0.5$, and convection has begun near the wall and at the grain boundaries, which are evident in figure 4.3. This is expected since the porosity, ϕ and hence from (3.9) the permeability, K is largest in these regions. There is no distinct wavenumber. Instead, roll pairs are separated by many different lengths. There are wave numbers from 0.8π – 5π , but most are larger than the predicted value of π . As ϵ is increased above onset to 1, as shown in figure 4.5(c), convection is evident in the ordered region. The convection along the grain boundaries is stronger than in the bulk regions and tends to pin the pattern, as can be seen as ϵ is increased up to 4 in figure 4.5(d-e). The pattern has not changed significantly, especially near the defects. Compare this to the

differences seen in the ordered media, as in figure 4.6-4.7, when ϵ is increased to 4. Figure 4.5(f) shows the pattern after dropping ΔT to 0 and returning to $\epsilon = 3$. The pattern is again very similar to the others, which shows that the defects tend to pin the pattern. Compare the differences here to the ordered media in figure 4.8. The wavenumber in the bulk is not well defined, although it is definitely smaller than π . A q of π would correspond to 5 roll pairs across the diameter. Although not as pronounced as in ordered media, the ratio of the size of up-flowing regions to down-flowing regions decreases as ϵ is increased.

The striking effect of the defects on the pattern formation is probably exacerbated by the small number of layers. Point defects would not effect the overall porosity as much if there were many layers. In our case, one missing bead from an area of close-packing can change ϕ by a third. Unfortunately, we cannot increase the number of layers significantly, as discussed in (§ 4.3.7). However, a poly-disperse set of beads would eliminate ordered regions and grain boundaries. The large variation in material properties that results, in the case of disordered media with small δ to h ratio, makes connection with current theory difficult. Moving to ordered media eliminates the large scale variations in favor of smaller periodic variations.

4.5.2 Ordered media

Because of the dominant role played by defects in the disordered medium, we decided to try ordered media. Although these systems have periodic spacial variations and large variations at the walls, we think that this is a good way to realize the ideal of uniform homogeneous properties, given the restriction on coarseness described in (§ 4.3.7).

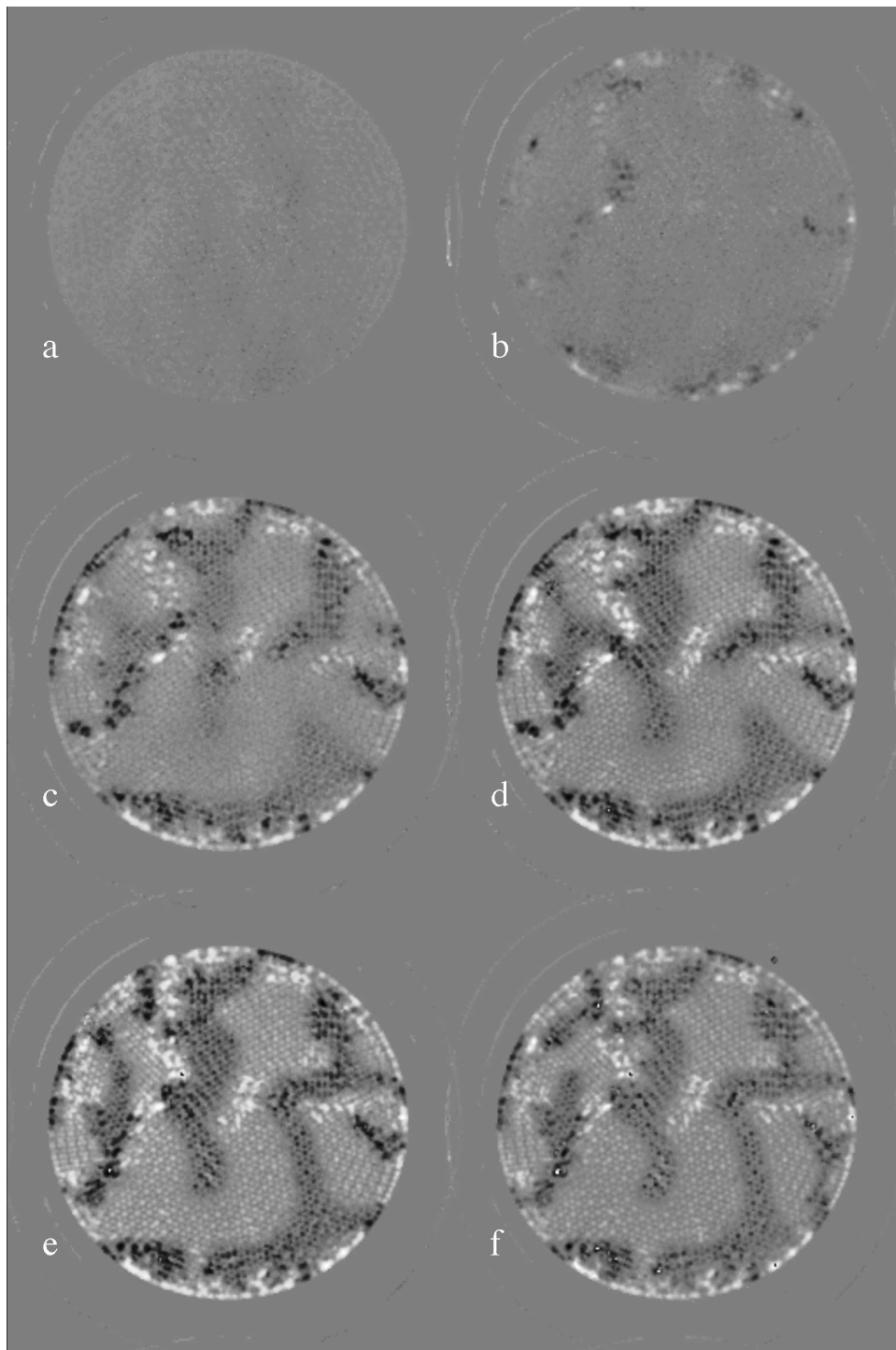


Figure 4.5: Vertically averaged, vertical velocity for circular cell with disordered packing. a) $\Delta T = 0$. b) $\epsilon = -0.5$. c) $\epsilon = 1$. d) $\epsilon = 3$. e) $\epsilon = 5$. f) $\epsilon = 3$, but after dropping ΔT to 0.

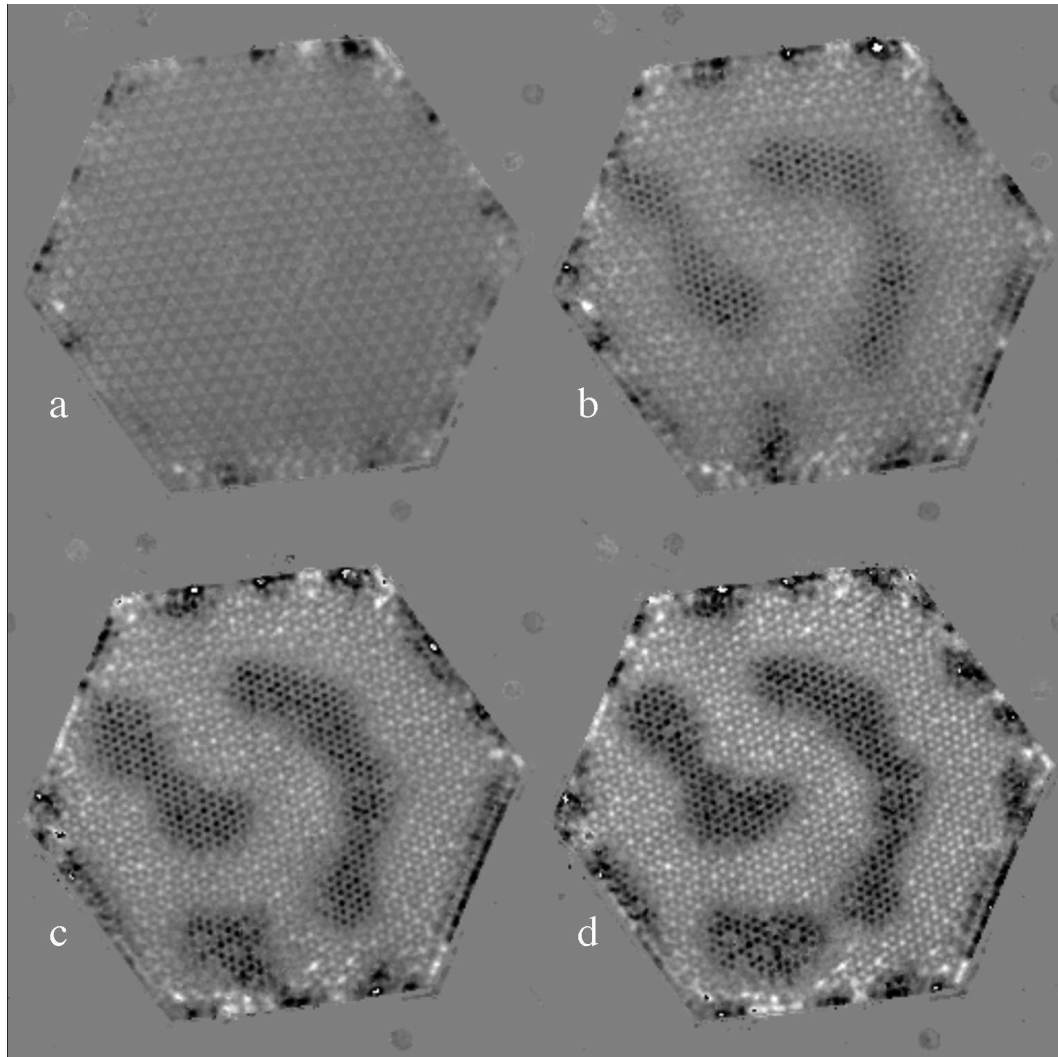


Figure 4.6: Vertically averaged, vertical velocity for hexagonal cell with ordered packing. a) $\epsilon = -0.2$. b) $\epsilon = 1$. c) $\epsilon = 2$. d) $\epsilon = 3$.

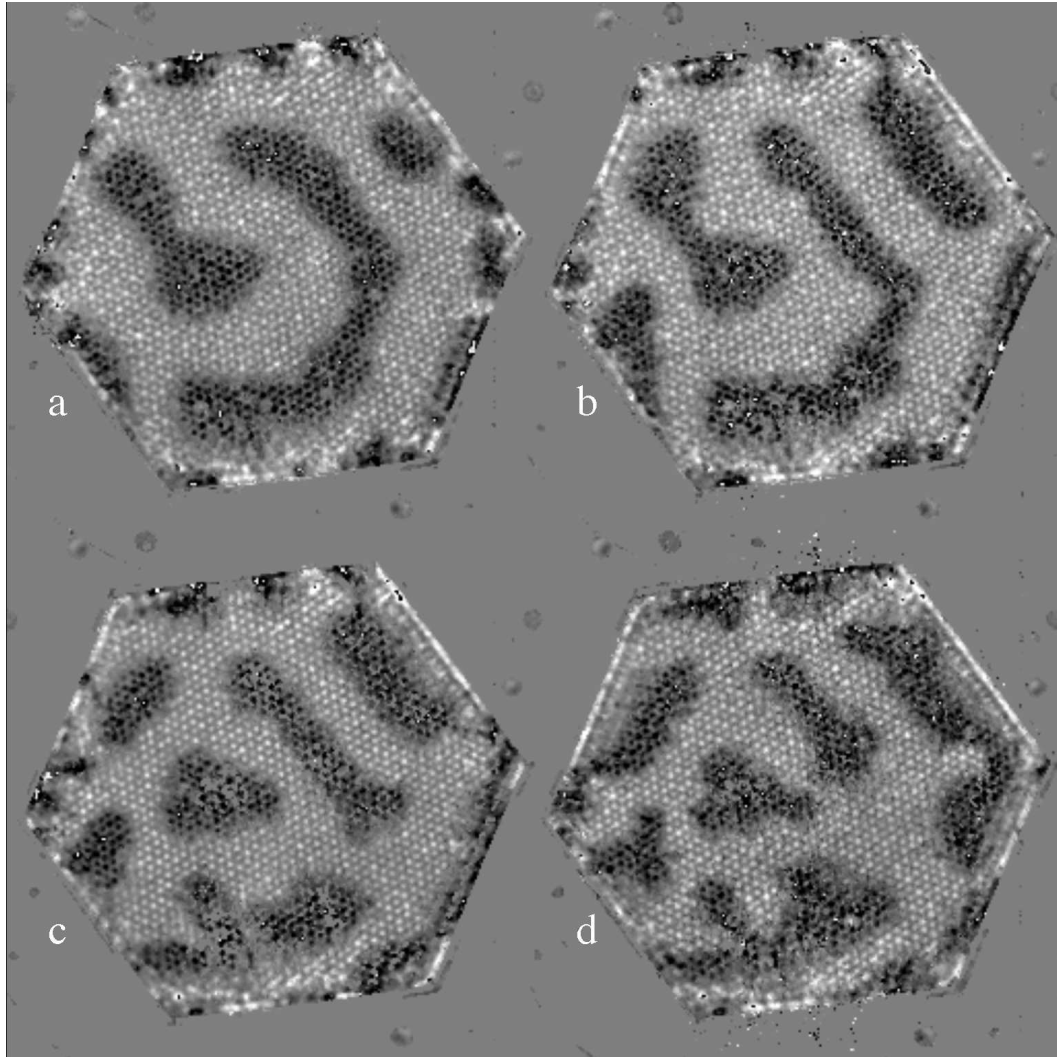


Figure 4.7: Vertically averaged, vertical velocity for hexagonal cell with ordered packing. a) $\epsilon = 4$. b) $\epsilon = 5$. c) $\epsilon = 6$. d) $\epsilon = 7$.

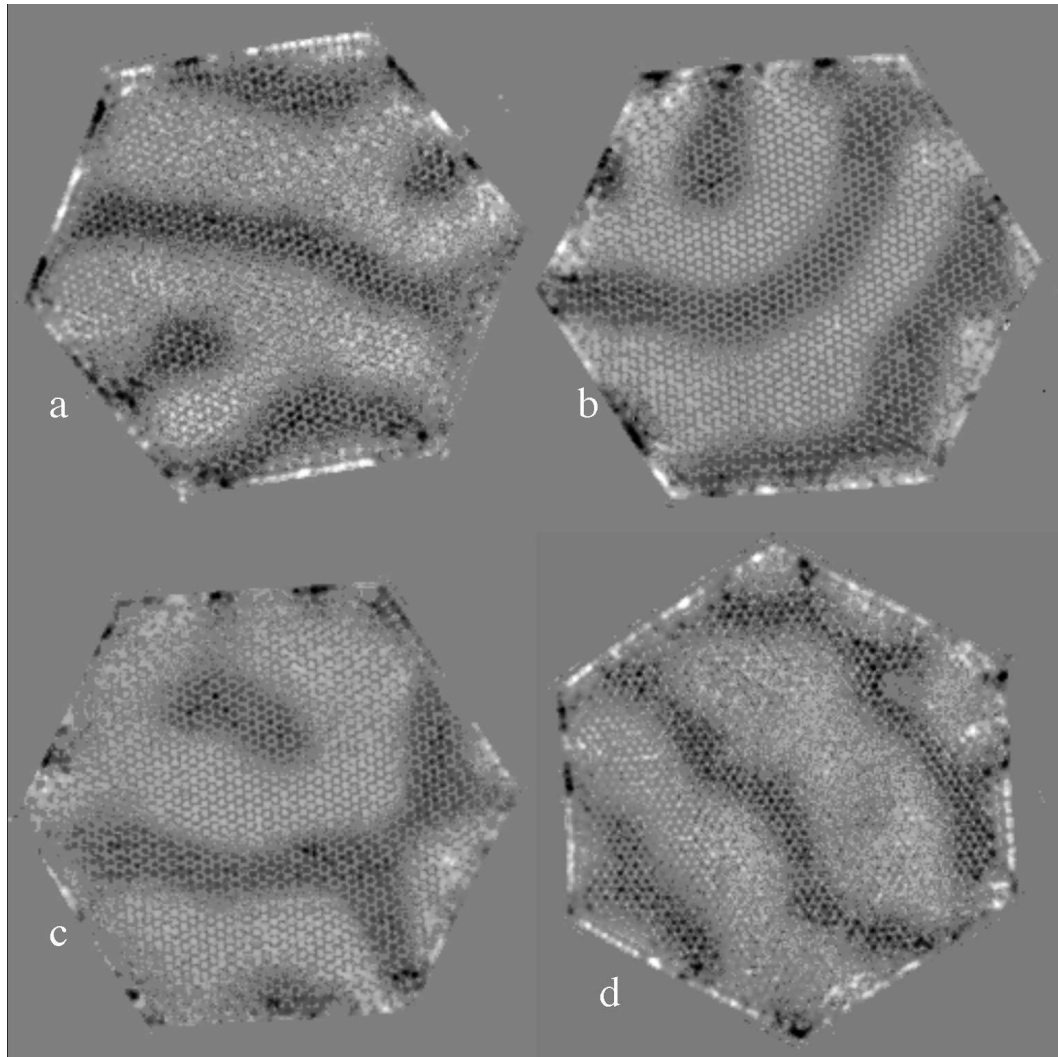


Figure 4.8: Vertically averaged, vertical velocity for hexagonal cell with ordered packing at $\epsilon = 1$, but ΔT was dropped to 0 between each image.

For the ordered media, we began our investigation with a rectangular planform as described in table 4.2. Because our packing has hexagonal symmetry, the defects along the short wall and the long wall are different. In our packing $\phi_L > \phi_S > \phi_{\text{bulk}}$, where ϕ_L , ϕ_S , and ϕ_{bulk} are the porosities of the long wall, the short wall, and the bulk, respectively. By (3.9) and (4.10) this leads to three regions with different Ra_c . We see three separate onsets of convection in the rectangular cell. Figure 4.9 shows the progression of the pattern as ϵ is increased. As in the disordered case, we define ϵ using Ra_c for the bulk. We see roll-like states in basic agreement with theory, although specific predictions for the wavenumber are not met. The convection begins first along the long wall in figure 4.9(a) at $\epsilon = -0.5$. The wavenumber, q_L , in this region is 2.05π , which is typical of the defect regions and is larger than the theoretical value of π . The convection begins on the short wall at $\epsilon = -0.2$ and the bulk at $\epsilon = 0$, by definition. The wavenumbers in these regions are $q_S = 1.35\pi$ and $q_{\text{bulk}} = 0.77\pi$, for the short wall and the bulk, respectively, as can be seen in figure 4.9(b,c). The wavenumber for the short wall is larger than the predicted value, but q_{bulk} is smaller than expected. It is interesting that $q_L > q_S > q_{\text{bulk}}$, just as for the porosity. We did not carry out enough experiments to determine if the asymmetry between up and down-flowing rolls seen in the other configurations was present. Instead, we moved to a hexagonal planform in order to limit further the effect of the walls.

In moving to a planform with the same symmetry as the packing, that is, hexagonal, the defects at the walls are all the same. In this arrangement, we studied states from $\epsilon = 0$ to $\epsilon = 7$. Up to $\epsilon = 4$, a steady state roll-like pattern is observed. Above $\epsilon = 4$ a more cellular time-dependent pattern is observed. The transition from roll-like to cellular is relatively smooth.

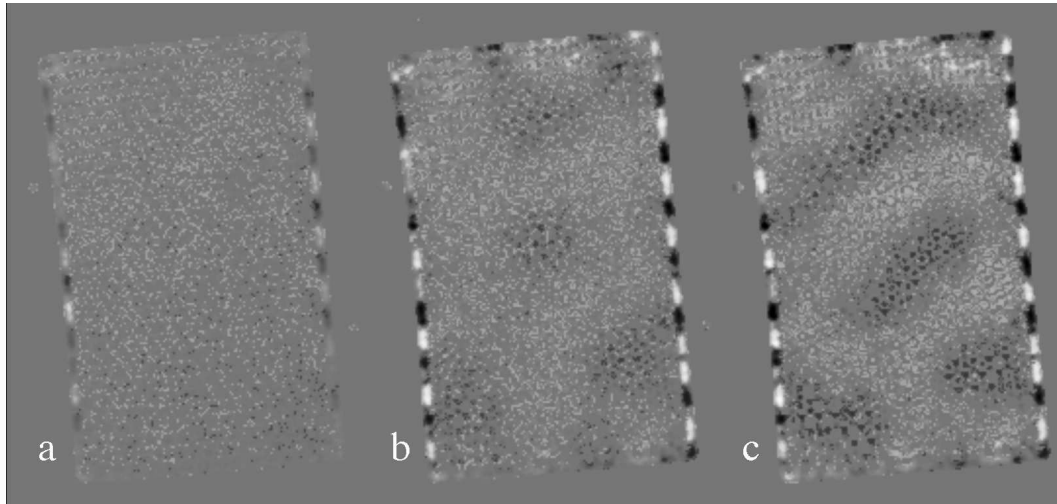


Figure 4.9: Vertically averaged, vertical velocity for rectangular cell with ordered packing for various values of ϵ . a) $\epsilon = -0.5$ b) $\epsilon = 0.2$ c) $\epsilon = 0.4$

In the steady regime, we are confident that the wall plays only a minor roll in pattern formation. This can be seen in figure 4.8, which shows 4 different patterns formed at $\epsilon = 1$ after cycling ΔT below ΔT_c . Although convection begins at $\epsilon = -0.2$ along the walls, different patterns are able to form in the bulk. This figure also shows the variability of the patterns formed. Unlike in RBC the slip boundary conditions in PMC do not force the rolls to be perpendicular at the boundaries. In these images we see rolls both perpendicular and parallel to the wall. Some patterns have horizontal symmetry, for example, figure 4.8(a), and some do not. The rolls also branch as in figure 4.8(c).

As discussed in (§4.3.5), we expect that within the stability region, the flow should rapidly decay to a steady state, due to the fact that the vertical vorticity decays so rapidly. To test this, we brought the system to $\epsilon = 7$, which is a rapidly changing, time-dependent state. From this state the system was quickly quenched to an ϵ within the stability region; $\epsilon \leq 4$. This technique has been previously used to test stability (Heutmaker, Fraenkel & Gollub, 1985;

Ahlers & Cannell, 1985). Figure 4.10 shows this process. Each image, except for the last, is separated by $2\tau_v$. In figure 4.10(a) the system is in the time-dependent state at $\epsilon = 7$. Between figure 4.10(a) and figure 4.10(b), in $0.3\tau_v$ the temperature is changed to $\epsilon = 2$. Figure 4.10(b-e) show the decay to steady state, and figure 4.10(f) shows the pattern $100\tau_v = 1.2\tau_h$ after figure 4.10(b). From these images and other experiments, in which we quench from $\epsilon = 7$ to $\epsilon = 0.2, 1, 3,$ and 4 , we see that steady state is approached in $2-5\tau_v$ and is stable for up to τ_h , except for minor adjustments in the wall regions. Presumably, the pattern will remain stable beyond τ_h , but we have not experimentally verified this.

Figure 4.6-4.7 show the pattern evolution as the temperature is increased in steps of 1ϵ from $\epsilon = 0$ to $\epsilon = 7$. From these images and figure 4.8 we can determine the wavenumber. A plot of ϵ versus reduced wavenumber, $Q = (q - q_c)/q_c$ for various runs along with the theoretical stability boundaries (Strauss & Schubert, 1978) is shown in figure 4.12. This plot was produced using Q since $q_c = 0.7\pi$ does not match the predicted value of π . It is also clear from figure 4.6-4.7 that there is an asymmetry between the horizontal size of the up-flowing rolls and the down-flowing rolls. A plot of their ratio is shown in figure 4.11 for various runs. The size ratio of up flowing rolls to down-flowing rolls steadily decreases as ϵ is increased. The length of the up-flowing rolls also decreases as ϵ is increased. By $\epsilon = 5$, figure 4.7(b), the pattern has become cellular, with small regions of fast up-flow in large regions of slower down-flow, and the up-flowing regions move about the cell. In all runs the up-flow has always covered a smaller region than the down-flow. The time-dependent motion at $\epsilon = 7$ is seen in figure 4.13. The images are $2\tau_v$ apart. The motion is not obviously periodic, although we do not have enough

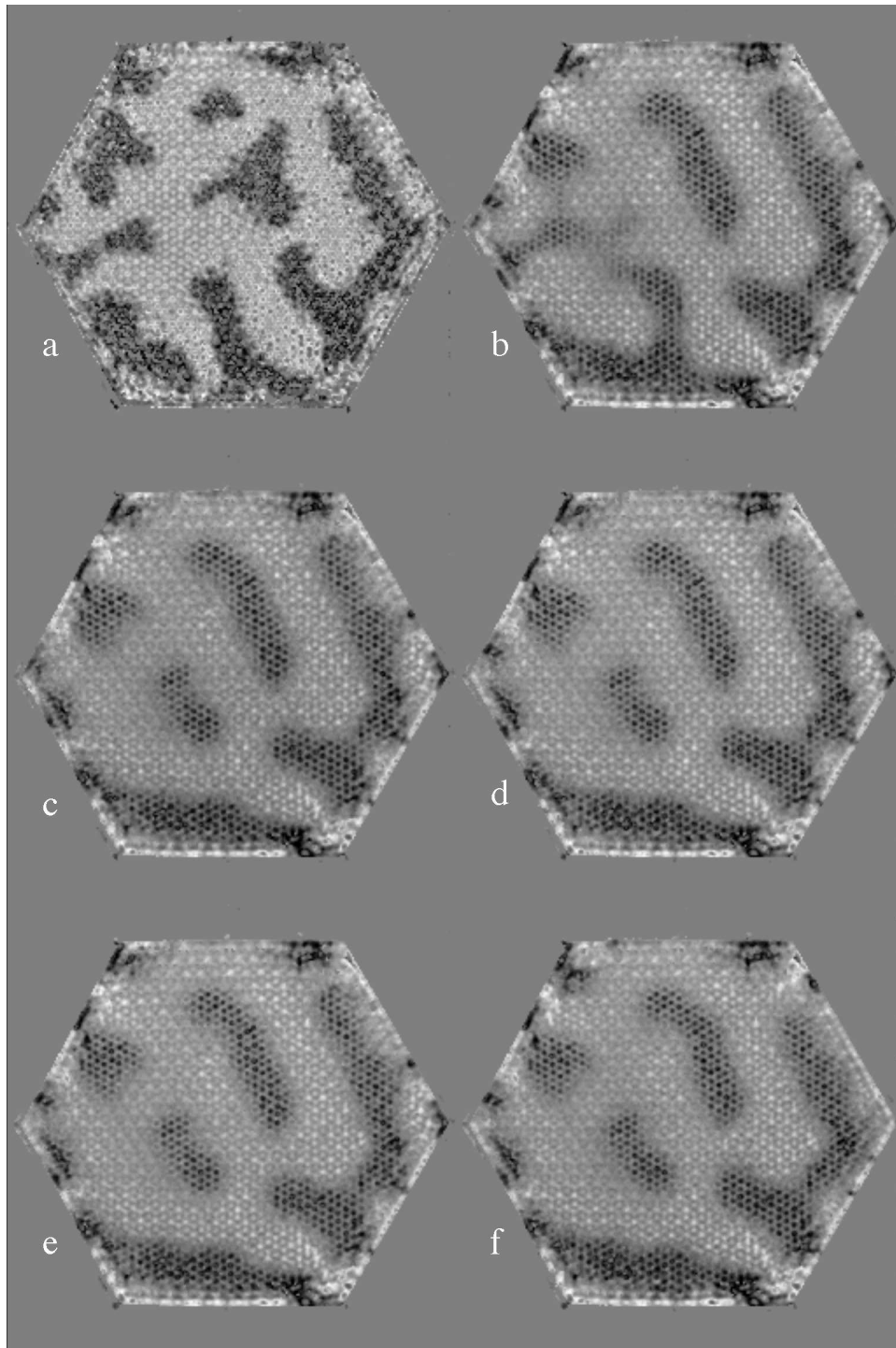


Figure 4.10: Vertically averaged, vertical velocity for hexagonal cell with ordered packing. All images, except for the last, are $2\tau_v$ apart. a) The time-dependent state before quenching ΔT . $\epsilon = 7$ b-e) Decay to steady state at $\epsilon = 2$. f) State $100\tau_v$ after quench.

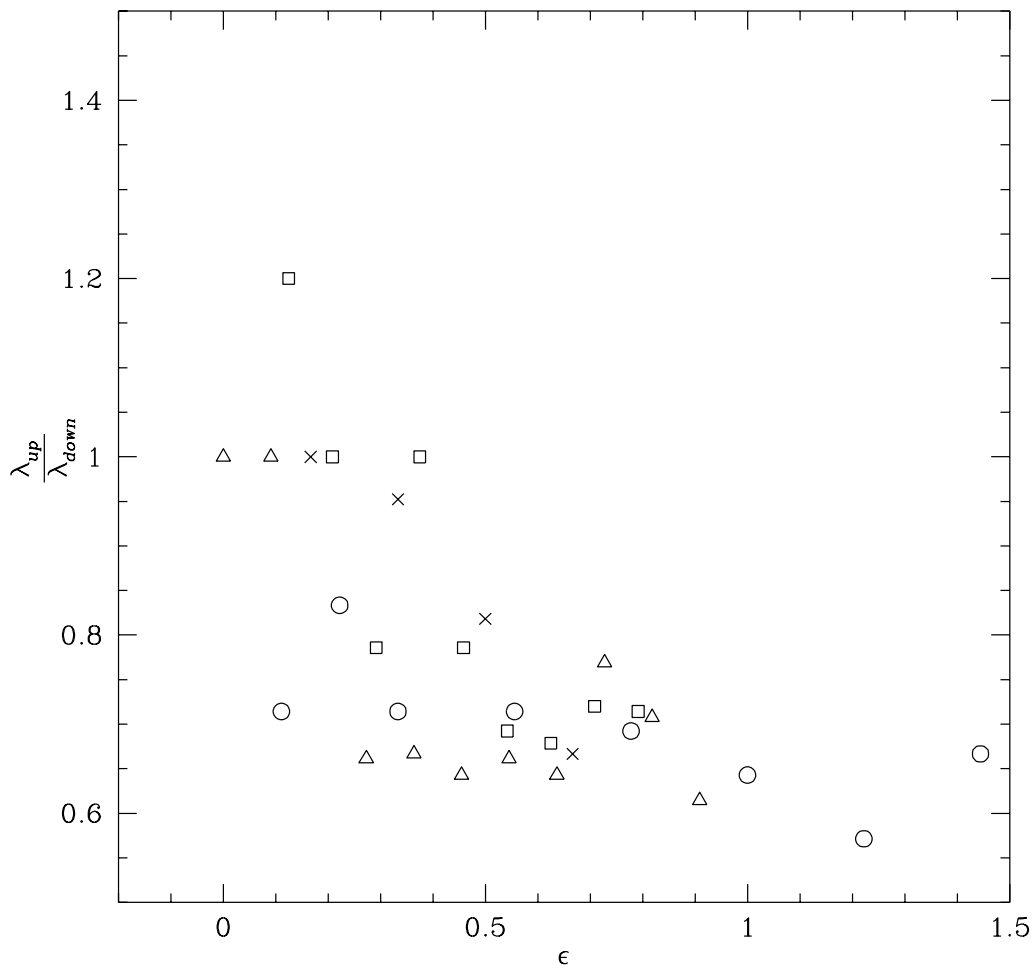


Figure 4.11: Plot of the ratio of up-flowing roll width to down-flowing roll width versus ϵ for several runs.

data to rule that out at this time.

In several runs we included our Nu measurement device. We did not use this routinely, because there are some qualitative differences in the pattern which is formed while using it. In figure 4.8(d) we have an example of the pattern with the device in place. The other images in that figure do not have the Nu measurement device in place. With the device in place, the roll boundaries are

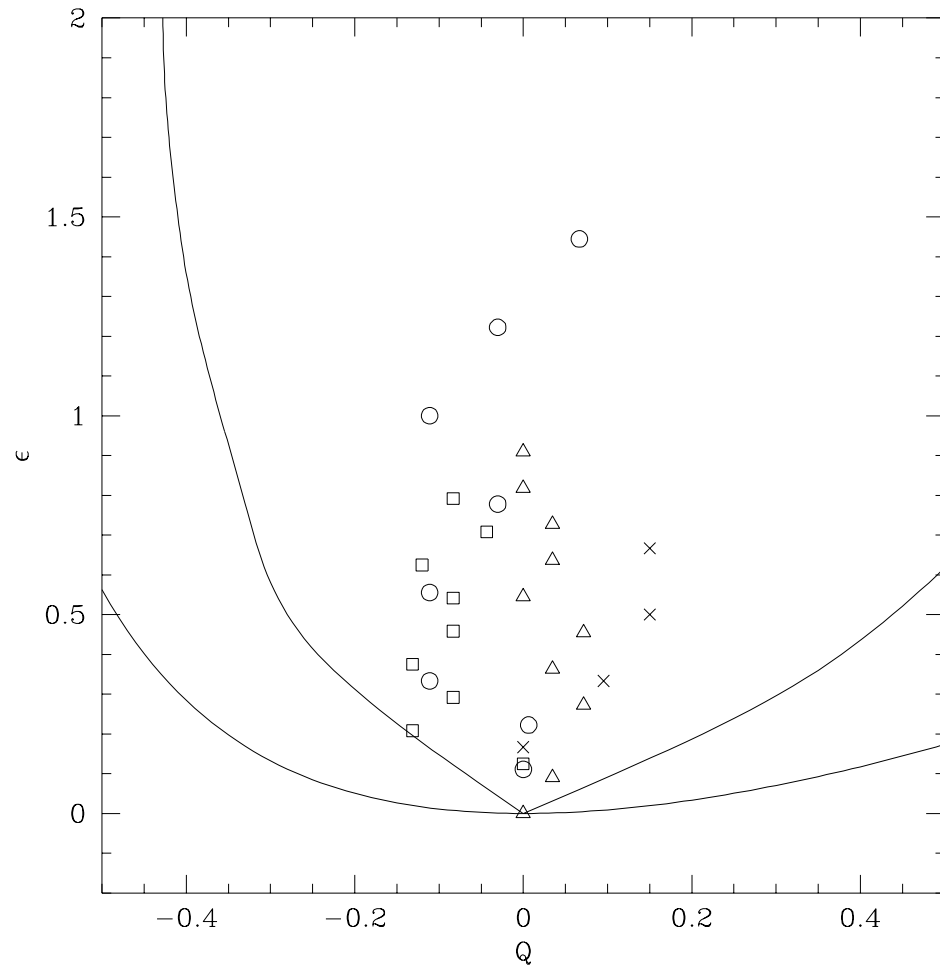


Figure 4.12: Plot of ϵ versus reduced wavenumber, Q for several runs.

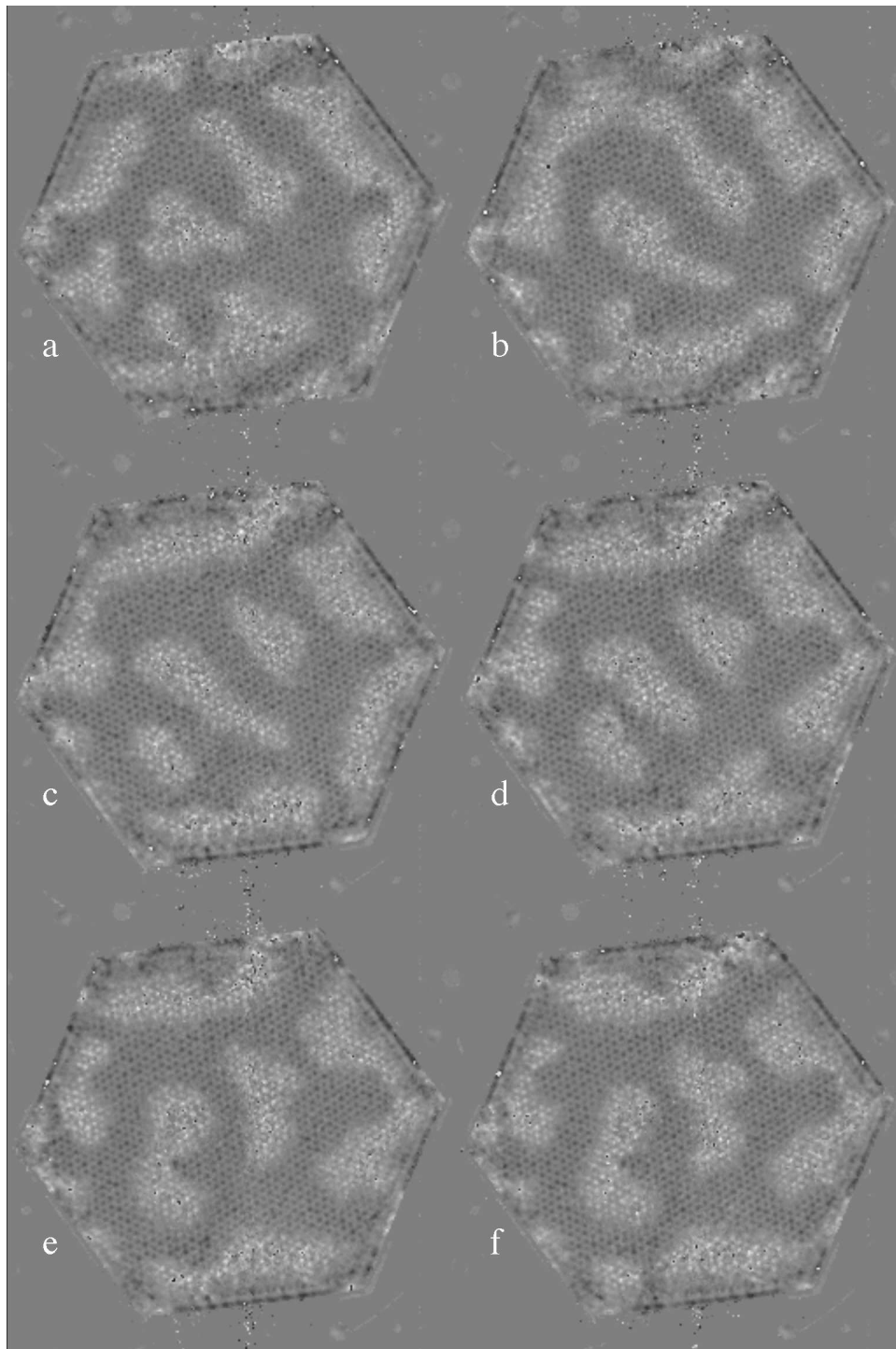


Figure 4.13: Vertically averaged, vertical velocity for hexagonal cell with ordered packing showing time-dependent behavior above 4ϵ . The images are separated by $2\tau_v$ and $\epsilon = 7$.

not as smooth, there is more branching, and the up-flow region is thinner at the same ϵ . It is not yet understood what is causing these differences. So, we have only used the device to help determine ΔT_c in two runs. The function $Nu(\epsilon)$ is plotted for those two runs in figure 4.14. The critical temperature for the two runs differs by 6% percent, which is significant. The values are $\Delta T_c = 8.5$ K and $\Delta T_c = 8.0$ K. The average slope of both curves is 0.725, which differs from the theoretical value of 2. The difference between the slopes of the two curves is not significant at our accuracy. Elder (1967) found that the Nu curve fit the equation

$$Nu = \frac{Ra}{4\pi^2} = 1 + \epsilon,$$

which is a slope of 1. Howle, Behringer & Georgiadis (1993) finds a slope of 0.33. Close, Symmons & White (1985) find that the slope is dependent on the coarseness, with coarser systems having lower slopes.

4.6 Conclusions

We have obtained the first velocity profiles in a convecting packed bed of spheres. This work represents a major step forward in understanding PMC, as previous experiments which attempted visualization have been invasive and ineffective in capturing the unperturbed flow field. We have studied both ordered and non-ordered systems. The disordered systems are characterized by large spacial variation in the critical parameters, combined with large regions of order. These systems exhibit defect pinning at the grain boundaries between the ordered regions. In the ordered media we see different patterns when we cycle below onset, which indicates that any remaining defects, at the wall for

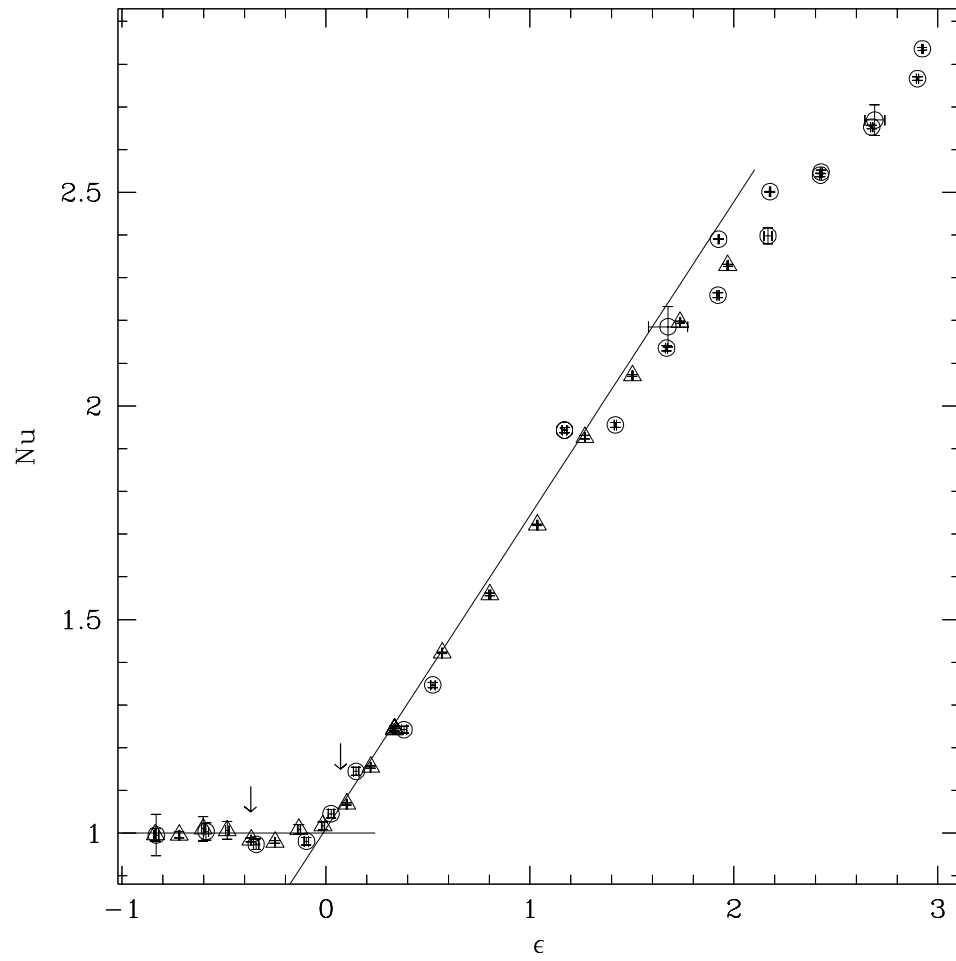


Figure 4.14: Plot of Nu versus reduced Ra , ϵ , for two different runs.

example, are not having a significant effect on the pattern.

One of the most important points to come out of this work is that there are experimental limitations on realizing the Darcy continuum limit in porous convection. This point is not well appreciated in the literature, and the Darcy model is routinely applied for modeling. The absence of the right kind of experiments has made tests of the Darcy model very difficult. In this work we juxtapose the standard models and experiment to emphasize that the former are inadequate. In the present study we examined five predictions. Four of these: the pattern at onset, the wavenumber at onset, the stability of patterns in the stability region, and the type of patterns produced after secondary instabilities occur, can only be examined in a system which has visualization capabilities. The fifth prediction, the slope of the Nu versus Ra curve, has been examined before, but we included it for completeness. Of these five predictions based on the continuum theory, we find that two, the pattern at onset and the stability of patterns in the stability region, match experiment. We found stable roll-like states near onset which remain stable up to $\epsilon = 5$. The states also relax rapidly, within $2-5\tau_v$, after quenching from a time-dependent state at $\epsilon = 7$. This is consistent with the rapid decay of vertical vorticity. The wavenumber at onset, the secondary instabilities, and the Nu versus Ra curve do not agree with theory. We measure the wavenumber at onset to be 0.7π instead of π . The stable time-independent states are predicted to lose stability to time-independent cross roll like states. Instead we find that they loss stability to a time-dependent state. The slope of the Nu versus Ra curve is found from weakly nonlinear theory to be 2. We have measured it to be $0.7 \pm .05$. We have also observed an interesting asymmetry in the size of the up-flowing and down flowing roll widths. The ratio of the width of the up-flowing roll to

the width of the down-flowing roll tends to decrease as ϵ is increased. As ϵ is increased further the up-flowing rolls break up and enter a time-dependent state at $\epsilon \simeq 6$.

4.7 Future Directions

These experiments have just begun to uncover the important aspects of PMC. In the future, we would like to examine the effect of coarseness in a systematic way. This could be accomplished in the ordered media by obtaining beads with radii that are integer multiples of each other. Then the same cell could be close packed with different radii beads. The packing arrangement clearly has a large effect on the pattern formed. It would be interesting to try to determine the effect of packing in a quantitative way.

The asymmetry between up and down-flow points to a breaking of the inversion symmetry which determines whether rolls or hexagons will be favored at onset. It would be interesting to look closely for hexagons near onset.

It is clear from the change in pattern with the Nu measurement device in place that a less perturbative method must be found. It is possible that a carbon based heater would allow r.f. field penetration.

We would also like to perform studies using binary mixtures. Binary mixtures have many interesting properties that are not present in single fluid convection. In particular, the study of oscillatory and traveling wave states has been very fruitful in RBC.

Conclusion

We developed a technique to noninvasively measure fluid flows in porous media using MRI and applied it to two important problems. First, we have measured the local velocity and density in pressure driven flows through packed beds. We verified long range order and oscillation in the porosity in poured spheres in a tube. We have measured for the first time flow channeling inside a porous medium, and found that the distribution of velocities is exponential.

We also applied the technique to porous media convection. Convective flows for disordered packings are strongly influenced by packing defects. Localization occurs because of pinning in regions where the permeability is locally large. Convective flows for ordered packings are consistent in several ways with predictions. In particular, there exists a range of Rayleigh numbers over which stable steady roll-like states are seen. Several observations differ from predictions for isotropic porous media. These include the relatively low value of the critical wavevector $q = 0.7\pi$ and the asymmetry between up-flows and down-flows. Finally the slope of the heat transport curve is found to be 0.7, whereas theory predicts that it should be two.

The discrepancies with theory are likely caused by two factors: large coarseness and temperature dependent parameters. In the future, we will address these situations both experimentally and theoretically. Experimentally, it may be possible to produce porous media with small coarseness, but large porosity. This combination would eliminate both problems. The large porosity would lead to a high permeability, which would lower ΔT_c . Temperature dependent parameter variation is less of a problem when the temperature difference is small. This could eliminate the largest discrepancies between the standard idealized system and our implementation. However, it is also desirable to be able to understand the coarser system, as it is of significant technical impor-

tance. To this end, the theory could possibly be adapted to match the coarse mono-disperse sphere media that we have studied in this work. One approach would be to introduce parameters, like the permeability, which would be averaged over a scale which is the same order as the pore scale. Ideally, this approach would average out the overwhelming details of the full fluid equations, but retain enough of the spacial variations to account for some of the discrepancies the we see when treating the medium as a single homogeneous average. Finally, temperature dependent parameter variation has been extensively studied in RBC. Now, that PMC visualization is available, there is more incentive to adapted to the case of PMC.

Bibliography

- Ahlers, G. & Cannell, D. S. (1985). Time dependence of flow patterns near the convective threshold in a cylindrical container. *Phys. Rev. Lett.*, *54*(13), 1373–1376.
- Ahmed, N. & Sunada, D. K. (1969). *J. Hydraul. Div., Proc ASCE*, *95*, 1847.
- Axel, L. & Dougherty, L. (1989). *Radiology*, *172*, 349.
- Bailes, D. R. & Bryant, D. J. (1984). *Contemp. Phys.*, *17*, 553.
- Bear, J. (1988). *Dynamics of Fluids in Porous Media*. Dover.
- Beckermann, C., Viskanta, R., & Ramadhyani, S. (1988). Natural convection in vertical enclosures containing simultaneously fluid and porous layers. *Journal of Fluid Mechanics*, *186*, 257–284.
- Benenati, R. F. & Brosilow, C. B. (1962). Void fraction distribution in beds of spheres. *AIChE J.*, *8*, 359.
- Bloch, F. (1946). Nuclear induction. *Phys. Rev.*, *70*, 460.
- Bloch, F., Hansen, W. W., & Packard, M. (1946). Nuclear induction. *Phys. Rev.*, *69*, 127.
- Bories, S. & Thirriot, C. (1969). Echanges thermiques et tourbillons dans une couche poreuse horizontale. *La Houille Blanche*, *24*, 237–245.
- Boussinesq, J. (1903). Théorie analytique de la chaleur. *Gauthier-Villars*, *2*.
- Brinkman, H. C. (1901). A calculation of the viscous force exerted by a flowing fluid on a dense swarm of particles. *Appl. Sci. Res. A*, *1*, 27–34.
- Burette, R. J. & Berman, A. S. (1976). Convective heat transfer in a liquid saturated porous layer. *ASME J. Appl. Mech.*, *43*, 249–253.
- Busse, F. H. (1967). The stability of finite amplitude cellular convection and its relation to an extremum principle. *Journal Fluid Mechanics*, *30*, 625.

- Busse, F. H. (1985). Transition to turbulence in Rayleigh-Bénard convection. In H. L. Swinney & J. Gollub (Eds.), *Hydrodynamic Instabilities and the transition to Turbulence* (2 ed.). (pp. 97–137). Berlin: Springer.
- Busse, F. H. & Joseph, D. D. (1972). Bounds for heat transport in a porous layer. *Journal of Fluid Mechanics*, *54*, 521–543.
- Busse, F. H. & Whitehead, J. A. (1971). Instabilities of convection rolls in a high Prandtl number fluid. *Journal Fluid Mechanics*, *47*, 305–245.
- Callaghan, P. T. (1991). *Principles of Nuclear Magnetic Resonance Microscopy*. London: Clarendon Press, Oxford.
- Cheng, P., Chowdhury, A., & Hsu, C. T. (1991). Forced convection in packed tubes and channels with variable porosity and thermal dispersion effects. In S. Kakaç, B. Kiliç, F. A. Kulacki, & F. Arinç (Eds.), *Convective Heat and Mass Transfer in Porous Media* (pp. 625–653). Dordrecht: Kluwer Academic.
- Chu, C. F. & Ng, K. M. (1989). Flow in packed tubes with a small tube to particle diameter ratio. *AIChE J.*, *35*(1), 148–158.
- Close, D. J., Symmons, J. G., & White, R. F. (1985). Convective heat transfer in shallow gas-filled porous media. *Int. J. Heat Mass Transfer*, *28*, 2371–2378.
- Combarous, M. (1970). Convection naturelle et convection mixte dans une couche poreuse horizontale. *Rev. Gén. Therm.*, *9*, 1355–1375.
- Combernous, M. A. & Bories, S. A. (1975). Hydrothermal convection in saturated porous media. *Hydroscience*, *10*, 231–307.
- Cross, M. C. & Hohenberg, P. C. (1993). Pattern formation outside of equilibrium. *Rev. Mod. Phys.*, *65*(3), 851–1112.
- Darcy, H. (1856). *Les Fontaines Publiques de la Ville de Dijon*. Dalmont.
- Doering, E. (1955). *Allg. Wärmetechnik*, *4*, 82.
- Dudgeon, C. R. (1966). *Houille Blanche*, *21*, 785.
- Dullien, F. A. L. (1979). *Porous Media: Fluid Transport and Pore Structure*. New York: Academic.
- Dumoulin, C. L. (1986). Magnetic resonance angiography. *Radiology*, *161*(3), 717–720.

- Elder, J. W. (1967). Steady free convection in a porous medium heated from below. *J. Fluid Mech*, *27*, 29–48.
- Ene, H. I. & Poliřevski, D. (1987). *Thermal Flow in Porous Media*. Dordrecht: Reidel.
- Ergun, S. (1952). Fluid flow through packed columns. *Chem. Eng. Prog.*, *48*, 89–94.
- Ernst, R. R., Bodenhausen, G., & Wokaun, A. (1987). *Principles of Nuclear Magnetic Resonance in One and Two Dimensions*. London: Clarendon Press, Oxford.
- Fancher, G. H. & Lewis, J. A. (1933). *Ind. Eng. Chem.*, *25*, 1140.
- Forchheimer, P. H. (1901). *Z. Ver. Deutsch. Ing.*, *45*, 1781.
- Georgiadis, J. G. (1991). Future research needs in convective heat and mass transport in porous media. In Kakac, S., Kilkis, B., Kulacki, F. A., & Arinc, F. (Eds.), *Convective Heat and Mass Transfer*, (pp. 1073–1088). NATO Advanced Study Institute, Kluwer Academic Publishers.
- Goldstein, H. (1980). *Classical Mechanics* (2 ed.). Reading, Massachusetts: Addison-Wesley Publishing Company.
- Greenside, H. S. (1995). Personal communication.
- Greenside, H. S., Cross, M. C., & W. M. Coughran, J. (1988). Mean flows and the onset of chaos in large-cell convection. *Phys. Rev. Lett.*, *60*, 2269.
- Gupta, V. P. & Joseph, D. D. (1973). Bounds for heat transport in a porous layer. *Journal of Fluid Mechanics*, *57*, 491–514.
- Hahn, E. L. (1950). Spin echoes. *Phys. Rev.*, *74*, 580.
- Haughey, D. P. & Beveridge, G. S. G. (1953). Local voidage variation in a randomly packed bed of equal-sized spheres. *Industrial and Engineering Chemistry*, *45*(6), 1209–18.
- Heutmaker, M. S., Fraenkel, P. N., & Gollub, J. P. (1985). Convection patterns: Time evolution of the wave-vector field. *Phys. Rev. Lett.*, *54*(13), 1369–1372.
- Hindman, J. C., Svirnickas, A., & Wood, M. (1971). Relaxation processes in water. The spin-lattice relaxation of deuterium in D₂O and oxygen ¹⁷O in H₂¹⁷O. *J. Chem Phys.*, *54*, 621–634.

- Hinshaw, W. S. & Lent, A. H. (1983). *Proc. IEEE*, 71(3), 338.
- Horton, C. W. & Rodgers, F. T. (1945). Convection currents in a porous media. *J. Appl. Phys.*, 16, 367–370.
- Hoult, D. I. (1979). *J. Magn. Reson.*, 35, 66.
- Howle, L. E., Behringer, R. P., & Georgiadis, J. G. (1993). Visualization of convective fluid flow in a porous medium. *Nature*, 362, 230–232.
- Irmay, S. (1958). On the theoretical derivation of Darcy and Forchheimer formulas. *Eos, Trans. AGU*, 39, 702–707.
- Jackson, J. D. (1975). *Classical Electrodynamics* (2 ed.). New York: John Wiley & Sons.
- Kaneko, T., Mohtade, M., & Aziz, K. (1974). An experimental study of natural convection in inclined porous media. *Int. J. Heat Mass Transfer*, 17, 485–496.
- Katto, Y. & Masuoka, T. (1967). Criterion for the onset of convective flow in a fluid in a porous medium. *Int. J. Heat Mass Transfer*, 10, 297–309.
- Kyan, C. P., Wasan, D. T., & Kintner, R. C. (1970). *Ind. Eng. Chem.*, 9, 596.
- Landau, L. D. & Lifshitz, E. M. (1987). *Fluid Mechanics* (2 ed.). New York: Pergamon Press.
- Lapwood, E. R. (1948). Convection of a fluid in a porous medium. *Proc. Camb. Phil. Soc.*, 44, 508–521.
- Lauterbur, P. C. (1973). Imaging formation by induced local interactions: Examples employing nuclear magnetic resonance. *Nature*, 242, 190.
- Lein, H. & Tankin, R. S. (1992). Natural convection in porous media—i. nonfreezing. *Int. J. Heat Mass Transfer*, 35(1), 175–186.
- Lister, C. R. B. (1990). An explanation for the multivalued heat transport found experimentally for convection in a porous medium. *J. Fluid Mech.*, 214, 287–320.
- Luther, H., Abel, O., Rittner, K., Giesler, M., & Schultz, H. J. (1971). *Chem. Ing. Tech.*, 6, 376.
- Macdonald, I. F., El-Sayed, M. S., Mow, K., & Dullien, F. A. L. (1979). Flow through porous media—the ergun equation revisited. *Ind. Eng. Chem. Fundam.*, 18(3), 199–208.

- Mansfield, P. & Grannell, P. K. (1973). Diffraction in solids? *J. Phys. C*, *6*, 190.
- Matthies, H. J. (1955). *VDI-Forschungsh.*, *454*.
- Morales, M., Spinn, C. W., & Smith, J. M. (1951). Velocity and effective thermal conductivities in packed beds. *Industrial and Engineering Chemistry*, *43*(1), 225–232.
- Moran, P. (1982). A flow velocity zeugmatographic interlace for nmr imaging in humans. *Magnetic Resonance Imaging*, *1*, 197–203.
- Morris, S. W., Bodenschatz, E., Cannell, D. S., & Ahlers, G. (1993). *Phys. Rev. Lett.*, *71*, 2026.
- Newell, A. C. & Whitehead, J. A. (1969). Finite bandwidth, finite amplitude convection. *J. Fluid Mech.*, *38*, 279.
- Nield, D. A. & Bejan, A. (1992). *Convection in Porous Media*. New York: Springer-Verlag.
- Northrup, M. A., Kulp, T. J., & Angel, S. M. (1991). Imaging of interstitial velocity fields and tracer distributions in a refractive index-matched porous medium. In *International Conference on Heat and Mass Transfer in Porous Media—Dubrovnik, Yugoslavia*.
- Oberbeck, A. (1879). Ueber die Wärmeleitung der Flüssigkeiten bei Berücksichtigung der Strömungen infolge von Temperaturdifferenzen. *Ann. Phys. Chem.*, *7*, 271–292.
- O'Donnell, M. (1985). Nmr blood flow imaging using multiecho, phase contrast sequences. *Med. Phys.*, *12*(1), 59–64.
- Pahl, M. H. (1975). PhD thesis, Karlsruhe.
- Palm, E., Weber, J. E., & Kvernfold, O. (1972). On steady convection in a porous medium. *Journal of Fluid Mechanics*, *54*, 153–161.
- Pauly, J., Nishimura, D., & Macovski, A. (1989). A k-space analysis of small-tip-angle excitation. *Journal of Magnetic Resonance*, *81*, 43–56.
- Prasad, V., Kulacki, F. A., & Keyhani, M. (1985). Natural convection in porous media. *J. Fluid Mech.*, *150*, 89–119.
- Purcell, E. M., Torrey, H. C., & Pound, R. V. (1946). Resonance absorption by nuclear magnetic moments in a solid. *Phys. Rev.*, *69*, 37.

- Redpath, T., Norris, D., Jones, R., & Hutchison, J. (1984). A new method of nmr flow imaging. *Phys. Med. Biol.*, *29*(7), 891–898.
- Rumpf, H. & Gupte, A. R. (1971). *chem. Ing. Tech*, *43*, 367.
- Schneider, K. J. (1963). Investigation on the influence of free thermal convection on the heat transfer through granular material. In *Proc. 11th int. Cong. of Refrigeration*, (pp. 247–253)., Oxford. Pergamon Press.
- Schwartz, C. E. & Smith, M. M. (1953). Flow distribution in packed beds. *Industrial and Engineering Chemistry*, *45*(6), 1209–1218.
- Segel, L. A. (1969). Distant side-walls cause slow amplitude modulation of cellular convection. *J. Fluid Mech.*, *38*, 203.
- Siggia, E. D. & Zippelius, A. (1981). Pattern selection in Rayleigh-Bénard convection near threshold. *Phys. Rev. Lett.*, *47*, 835.
- Singer, J. R. (1980). Blood flow measurements by nmr of the intact body. *IEEE Trans. Nuclear Science*, *27*(3), 1245–49.
- Stephenson, J. L. & Stewart, W. E. (1986). Optical measurement of porosity and fluid motion in packed beds. *Chemical Engineering Science*, *41*(8), 2161–2170.
- Strauss, J. M. (1974). Large amplitude convection in porous media. *J. Fluid Mech*, *64*, 51–63.
- Strauss, J. M. & Schubert, G. (1978). *J. Fluid Mech*, *87*, 385.
- Szekely, J. & Poveromo, J. J. (1975). Flow maldistribution in packed beds: A comparison of measurements with predictions. *AlChE Journal*, *21*(4), 769–772.
- Torrance, K. E., Schoenhals, R. J., Tien, C. L., & Viskanta, R. (1982). Natural convection in porous media. In Yang, K. T. & Lloyd, J. R. (Eds.), *Proceedings of a Workshop on Natural Convection*, (pp. 36–45).
- Volkov, S. A., Reznikov, V. I., Khalilov, K. F., Zel'vensky, V. Y., & Sakydinsky, K. I. (1986). Nonuniformity of packed beds and its influence on longitudinal dispersion. *Chemical Engineering Science*, *41*(2), 389–397.
- Ward, J. C. (1964). Turbulent flow in porous media. *ASCE J. Hydraul. Div.*, *90*, 1–12.

- Whitaker, S. (1986). Flow in porous media: A theoretical derivation of Darcy's law. *Transport in Porous Media*, 1, 3–25.
- Yen, Y. C. (1974). Effects of density inversion on free convective heat transfer in porous layer heated from below. *Int. J. Heat. Mass Transfer*, 17, 1349–1356.

Biography

MARK SHATTUCK

Born: Fort Wauchuca, AZ

Education: Wake Forest University
Winston-Salem, North Carolina
B.A., Physics, *magna cum laude*, 1987
M.S., Physics, 1989

Duke University
Durham, North Carolina
M.A., Physics, 1991
Ph.D., Physics, 1995

Master's Thesis: *The Kinetics and Diffusion of Radicals in X-irradiated L- α -Amino-n-butyric Acid Hydrochloride with L-cysteine Hydrochloride as Impurity*
Professor Howard Shields, advisor (May 1989)

Dissertation: *Flows in Porous Media Convection: Visualization by Magnetic Resonance Imaging*
Professor Robert Behringer, advisor (May 1995)

Position: Graduate Teaching Assistant, Wake Forest University, 1985–1988
Graduate Teaching Assistant, Duke University, 1988–1990
Graduate Research Assistant, Duke University, 1990–1994
Associate in Research, Duke University, 1994–1995
Research Associate, Duke University, 1995–present

Professional Societies: *American Physical Society*
Sigma Xi

Honors: Fritz London Fellowship 1993-1994
Conference Travel Fellowship, 1991,1992,1993,1994

Publications

1. M. D. Shattuck, Y. Ma, M. Itoh, and H. Shields, *An ESR Study of Radical Kinetics in L- α -Amino-n-butyric Acid Hydrochloride Containing L-Cysteine Hydrochloride*, Radiat. Res. **120**, 430-441 (1989).
2. J. Georgiadis, R. P. Behringer, M. Shattuck, and G. A. Johnson, *Interstitial Velocity and Temperature Fields in Fully-saturated Porous Media*, Proceedings of the Ninth Symposium on Energy Engineering Sciences (1990).
3. M. Shattuck, R. P. Behringer, J. Georgiadis, and G. A. Johnson, *Experimental Techniques in Multiphase Flows*, volume FED125, chapter: Magnetic Resonance Imaging of interstitial velocity distributions in porous media, American Society of Mechanical Engineers, 39–46 (1991).
4. K. E. Anderson, M. D. Shattuck and R. P. Behringer, *Novel Cross Roll State in Cylindrical Convection Cell with Thermally Conducting Side-walls*, Phys. Rev. A **46**,(10) 6143–6146 (1992).
5. M. Shattuck, R. P. Behringer, J. Georgiadis, and G. A. Johnson, *Magnetic Resonance Imaging of Convection in Porous Media*, Proceedings of the twelfth Symposium on Energy Engineering Sciences (1994).
6. M. D. Shattuck, R. P. Behringer, J. Georgiadis, and G. A. Johnson, *Onset and Stability of Convection in Porous Media: Visualization by MRI*, Phys. Rev. Let. submitted (July 1994).

Contributed Presentations

1. M. Shattuck, Y. Haven, and H. Shields, *The Identity and Structure of the Sulfur Radicals in X-Irradiated Amino Acids Containing Cysteine as an Impurity*, Bull. Am. Phys. Soc. **32**(3) 799 (1987).
2. Ma Yi, M. Shattuck, B. Kopelman, Y. Haven, and H. Shields, *The Activation Energy and Mechanism for Transfer of Radiation Damage in Irradiated Amino-Butyric Acid*, Bull. Am. Phys. Soc. **33**(3) 565 (1988).
3. M. Shattuck, R. P. Behringer, J. Georgiadis, and G. A. Johnson, Duke University, *Local Velocity in Porous Media Flow Using Magnetic Resonance Imaging*, Bull. Am. Phys. Soc. **36**(9) (1991).
4. M. Shattuck, R. P. Behringer, J. Georgiadis, and G. A. Johnson, Duke University, *Local Velocity Measurements in Porous Media Convection Using Magnetic Resonance Imaging*, Bull. Am. Phys. Soc. **37**(9) (1992).
5. M. Shattuck, R. P. Behringer, J. Georgiadis, and G. A. Johnson, Duke University, *Convection Patterns in Random and Ordered Porous Media*, Bull. Am. Phys. Soc. **38**(9) (1993).
6. M. Shattuck, R. P. Behringer, J. Georgiadis, and G. A. Johnson, Duke University, *Relaxation and Stability of Porous Media Convection with Visualization by Magnetic Resonance Imaging*, Bull. Am. Phys. Soc. **39**(9) (1994).
7. M. Shattuck, S. L. Gewalt, G. H. Glover, L. W. Hedlund, G. A. Johnson, Duke University, *Three-Dimensional Measurements of Lung Properties*

during the Breathing Cycle, Third International Conference on Magnetic Resonance Microscopy. (1995)